UNIVERSIDADE DE LISBOA
INSTITUTO SUPERIOR TÉCNICO

THE GALACTIC CENTER: A TESTING GROUND FOR DARK MATTER AND GRAVITY THEORIES

ARIANNA FOSCHI

SUPERVISOR : Doctor Vitor Manuel dos Santos Cardoso

CO-SUPERVISOR : Doctor Paulo Jorge Valente Garcia

THESIS APPROVED IN PUBLIC SESSION TO OBTAIN THE PHD DEGREE IN
PHYSICS

JURY FINAL CLASSIFICATION: PASS WITH DISTINCTION

2024

UNIVERSIDADE DE LISBOA
INSTITUTO SUPERIOR TÉCNICO

THE GALACTIC CENTER: A TESTING GROUND FOR DARK MATTER AND GRAVITY THEORIES

ARIANNA FOSCHI

SUPERVISOR : Doctor Vitor Manuel dos Santos Cardoso
CO-SUPERVISOR : Doctor Paulo Jorge Valente Garcia

THESIS APPROVED IN PUBLIC SESSION TO OBTAIN THE PHD DEGREE IN
PHYSICS
JURY FINAL CLASSIFICATION: PASS WITH DISTINCTION

JURY

CHAIRPERSON:
Doctor Ilídio Pereira Lopes, Instituto Superior Técnico, Universidade de Lisboa

MEMBERS OF THE COMMITTEE :
Doctor Vitor Manuel dos Santos Cardoso, Instituto Superior Técnico, Universidade de Lisboa
Doctor Andrea Maselli, School of Advanced Studies, Gran Sasso Science Institute, Italy
Doctor Stefan Gillessen, Max Planck Insitute for extraterrestrial Physics, Garching, Germany
Doctor David Matthew Hilditch, Instituto Superior Técnico, Universidade de Lisboa

FUNDING INSTITUTIONS:
European Research Council
Faculdade de Engenharia da Universidade do Porto
FCT: Fundação para a Ciência e a Tecnologia

2024

THE GALACTIC CENTER: A TESTING GROUND FOR DARK MATTER AND GRAVITY THEORIES

ARIANNA FOSCHI

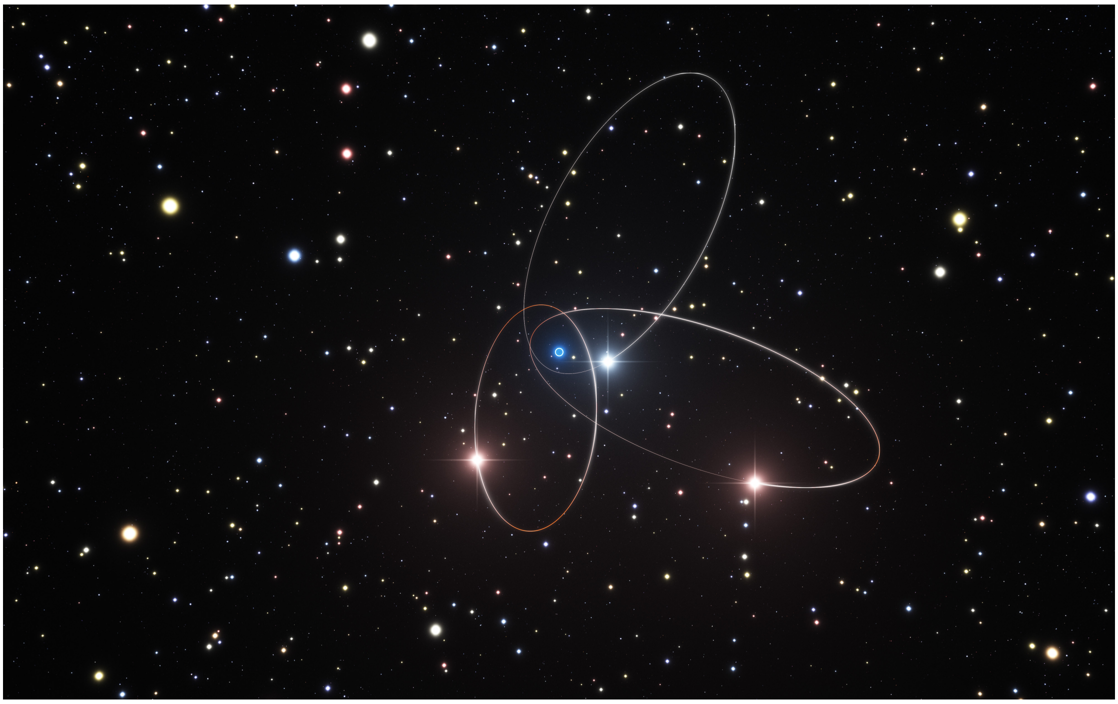

Credits for image: ESO/M. Parsa/L. Calçada

2024

A Domenico e Livia.
Passato, presente e futuro della mia vita.

A Giulio Regeni,
che non ha mai consegnato la sua tesi,
perchè abbia giustizia.

RESUMO

A descoberta de estrelas que orbitam muito próximas de Sagittarius A*, o buraco negro supermassivo no centro galáctico da Via Láctea, abriu uma nova via para testar o seu campo gravitacional e estudar o ambiente que o rodeia.

Além disso, os dados recolhidos sobre as estrelas podem ser combinados com as imagens obtidas pelo Event Horizon Telescope da região próxima do horizonte de eventos, produzindo o laboratório perfeito para testar a teoria da gravidade e restringir modelos de matéria escura. Esta última representa um dos maiores desafios (actuais) da física, uma vez que existem várias observações experimentais que suportam a sua existência no Universo, mas nenhum dos modelos propostos pode ser considerado conclusivo.

Nesta tese de doutoramento investigamos o movimento geodésico, i.e., a trajetória de uma partícula de teste num campo gravitacional específico, com o objetivo de compreender possíveis assinaturas de um tal fundo. Ao considerar o regime de campo forte, a equação da geodésica é resolvida para restringir as assinaturas devidas a um companheiro oculto ou estudar a luminosidade da matéria acretada por um buraco negro de Schwarzschild.

No contexto das estrelas no Centro Galáctico, investigamos a possibilidade da matéria escura, sob a forma de um campo ultraleve, se aglomerar em torno de Sagittarius A* criando uma nuvem, e usamos os dados disponíveis para a estrela S2, uma das mais próximas do Centro Galáctico, para determinar a massa dessa nuvem.

Exploramos também a possibilidade de existir uma quinta força no Universo e desta aparecer como uma modificação do potencial newtoniano do tipo Yukawa no limite do campo fraco. Através de dados de S2, a intensidade dessa quinta força no centro galáctico é limitada.

PALAVRAS-CHAVE: relatividade geral; buracos negros; centro galáctico; matéria escura; mecânica celeste.

ABSTRACT

The discovery of stars orbiting very close to the supermassive black hole at the Galactic Center of the Milky Way, Sagittarius A*, opened a new way to test its gravitational field and constrain the environment around it. Moreover, data collected on stars can also be combined with the near horizon images taken by the Event Horizon Telescope, producing the perfect laboratory to test the theory of gravity and constrain dark matter models. The latter represents one of the major challenges in physics, since there are several experimental observations proving its existence in the Universe, but none of the proposed models can be seen as conclusive.

In this doctoral thesis we investigate the geodesic motion, i.e., the trajectory of a test particle in a specific gravitational field, with the aim of understanding possible signatures of such a background. When considering the strong field regime, the geodesic equation is solved to either constrain the signatures due to an hidden companion or study the luminosity of matter accreted by a Schwarzschild black hole.

In the context of stars at the Galactic Center, we investigate the possibility that dark matter in the form of an ultralight field clusters around Sagittarius A* creating a cloud, and we use the available data for star S2, one of the closest to the Galactic Center, to constrain the mass of such a cloud.

We also explore the possibility that a fifth force exists in the Universe and appears as a Yukawa-like modification to the Newtonian potential in the weak field limit. By means of S2 data, the intensity of such a fifth force is constrained at the Galactic Center.

KEY-WORDS: general relativity; black holes; galactic center; dark matter; celestial mechanics.

PUBLICATIONS

This doctoral thesis is based on the following publications:

V. Cardoso & A. Foschi, *Geodesic structure and quasinormal modes of a tidally perturbed spacetime*, Phys. Rev. D, 104 (2021) 2, 024004; arXiv:2106.06551 [gr-qc]

V. Cardoso, F. Duque, A. Foschi, *Light ring and the appearance of matter accreted by black holes*, Phys. Rev. D103 (2021) 10, 104044; arXiv:2102.07784 [gr-qc].

A. Foschi & the GRAVITY Collaboration, *Using the motion of S2 to constrain scalar clouds around SgrA**, Mon. Not. Roy. Astron. Soc. 524 (2023) 1, 1075 − 1086; arXiv:2306.17215 [gr-qc].

A. Foschi & the GRAVITY Collaboration, *Using the motion of S2 to constrain vector clouds around SgrA**, Mon. Not. Roy. Astron. Soc. (2023); arXiv:2001.01729 [gr-qc].

A. Foschi & the GRAVITY Collaboration, *Testing the Yukawa potential at the Galactic Center*, in preparation.

During the years of my doctoral program, I also coauthored the following works (not - or only partially - discussed in this thesis):

V. Cardoso, A. Foschi & M. Zilhão, *Collective scalarization or tachyonization: when averaging fails*, Phys. Rev. Lett. 124 (2020) 22, 221104; arXiv:2005.12284 [gr-qc]

The GRAVITY Collaboration, *Mass distribution in the Galactic Center based on interferometric astrometry of multiple stellar orbits*, Astron. Astrophys. 657 (2022) L12; arXiv:2112.07478 [gr-qc]

The GRAVITY Collaboration, *Where intermediate-mass black holes could hide in the Galactic Center - A full parameter study with the S2 orbit*, Astron. Astrophys. 677 (2023) C2; arXiv:2303.04067 [gr-qc]

The GRAVITY Collaboration, *Polarimetry and astrometry of NIR flares as event horizon scale, dynamical probes for the mass of SgrA**, Astron. Astrophys. 677 (2023) L10; arXiv:2307.11821[gr-qc]

ACKNOWLEDGMENTS

I would like to acknowledge the financial support from Fundação para a Ciência e Tecnologia through the scholarship PRT/BD/153347/2021 and the Faculty of Engeneering of Universidade do Porto through the grant PTDC/FIS-AST/7002/2020. I would also like to thank the support of the European Union's 2020 ERC Consolidator Grant "Matter and strong-field gravity: New frontiers in Einstein's theory" (grant agreement n. MaGRaTh-646597), the European Union's H2020 ERC Advanced Grant “Black holes: gravitational engines of discovery” (grant agreement n. Gravitas–101052587), and the financial help provided by the GWverse COST Action CA16104, “Black holes, gravitational waves and fundamental physics”, together with the Marie Sklodowska-Curie scholarship N. 101007855.

I would like to thank my supervisor, Vitor Cardoso, and my co-supervisor, Paulo Garcia, for their support and their willingness to help me at any time.

Many thanks go to the members of the GRAVITY collaboration who helped me during this journey: Stefan Gillessen, Gernot Heißel, Frédéric Vincent, Thibaut Paumard, Diogo Ribeiro, Matteo Sadun Bordoni and Antonia Drescher. I would also like to thank Jarle Brichmann for fruitful discussions on Monte Carlo methods.

A huge thanks goes to CENTRA and its incredible members, with a particular mention to GRIT and all those people who made my PhD way more easier. You have all been great. Thanks to our secretaries, Rita and Dulce, without whom CENTRA would not work as it should.

A special mention goes to my fellow PhDs: Lorenzo, Thanasis, Isabel, Antoine, Francisco, David, Rodrigo. Without your guidance, your support and the laughs we had together, everything would have been much more difficult to deal with. My best memories here are with you, guys. Thanks to my office mates Christian, Krinio, Tiago and Jorge for the chatting and the chilled environment you helped to create in our office.

Thank you to my Lisbon friends: Saby, Joan, Matteo, Giorgio, Martina, Gemma, Santiago, Mariana and all those people with whom I have had the pleasure of spending time with. I am going to miss our dinners and parties together so much.

Chiara, grazie per essermi stata vicina fisicamente e metaforicamente, per tutti i consigli, il divertimento e l'aiuto che mi hai dato. Grazie anche a Marco, che da "il ragazzo di Chiara" è presto diventato un amico con cui chiacchierare, guardare l'AS Roma e addormentarsi durante i film.

Grazie a Sara, per essere una persona speciale con cui è un onore condividere la vita e i suoi drammi, e per aver fondato *Piena*, un luogo che sa di casa e che porterò sempre nel cuore.

Grazie a Saro, che col suo senso dell'umorismo ("da quattro soldi", *cit.*) mi ha rallegrato tante giornate cupe e si è dimostrato un compagno di serate degne di questo nome.

Grazie al Bucci Roma Club: Sebastiano, Beppe, Leonardo e Stefano. Siete state le prime persone che ho incontrato qui e so che imprecare la magica senza di voi non sarebbe stato lo stesso.

Agradeço à minha academia de BJJ, Brazilian Fight Lisboa, ao meu professor Rafael e a todos os meus parceiros de treino. Oss!

Grazie a Laura, per essere sempre e comunque al mio fianco, e a Sebastiano, perchè insieme mi hanno donato Livia, che illumina le mie giornate anche a distanza e mi restituisce speranza nel mondo.

Grazie a la *Familia* di Albano, membri vecchi e nuovi. Mi ricordate che alcune cose non cambiano mai e forse è proprio questo che le rende speciali. Grazie a Gabriele, che è venuto a trovarmi quando meno me l'aspettavo e ha condiviso con me questa splendida città e un pezzettino della mia vita. Grazie a Lorenzo e Simone, poco noti con il loro vero nome, perchè è impossibile per me muovermi nel mondo e portare avanti la mia vita senza il loro costante, incondizionato supporto.

Grazie a Stefano detto il Fresco, presenza costante nella mia vita da ormai quasi vent'anni, fratello acquisito, che più di tutti mi ha tenuto compagnia mentre ero lontana e ha contribuito a creare i miei migliori ricordi lisbonesi.

Grazie a Sara, la mia amica del cuore che sento sempre vicina, anche quando è a centinaia di chilometri di distanza o quando la vita fa brutti scherzi. Se c'è qualcuno che mi ha insegnato a non mollare mai, sei certamente tu.

Grazie, ovviamente, al gruppo *cacca*, senza il quale non ci sarebbe stata neanche una laurea, figuriamoci un dottorato. A Simone, per essersi accollato i miei problemi scientifici (che non sono stati pochi), a Matteo, che mi ha ascoltato sbroccare mille e più volte, e a tutti gli altri che sono sempre lì per ascoltare, confrontarsi, ridere. Alle mie amiche scienziate, Alessia, Ilenia e Rita, per avermi sempre fatto trovare un posto sicuro in cui essere me stessa e per aver portato alta la bandiera delle donne nella scienza.

Grazie a Francesca, che mi ha letteralmente salvato dal baratro e ha sempre creduto in me, non lasciandomi mai sola.

Grazie a mamma e a papà, per il loro supporto incondizionato. Ma anche a nonna, a zia Lia, a Francesca e Andrea, e a tutta la mia famiglia *di nascita*, che nel bene e nel male mi ha resa la persona che sono ora.

Grazie a Daniele, e a Paz. Non esistono parole adeguate per esprimere quanto sia grata di aver condiviso un pezzo (enorme) di strada insieme a voi. Se ho costruito un percorso di vita è perchè c'eravate voi a passarmi le mattonelle.

Grazie alla famiglia Zoppi, quella allargata che comprende tutti. Mi avete sempre fatta sentire accolta e benvoluta e per questo vi ringrazio, perchè l'affetto non è mai scontato.

Trovo quasi incredibile dover ringraziare una città, ma Lisbona ha il miracoloso potere di aggiustare le giornate storte semplicemente risplendendo nei suoi vivaci colori. E allora grazie Lisboa, per essere sempre meravigliosa, per avermi insegnato a vivere lentamente, per essere diventata immediatamente *casa mia*, per avermela fatta *pia a bene* anche quando sembrava impossibile. Grazie a *OBazzar*, *Amor Perfeito*, *Piena*, *Ideal* e il bar in fondo alla strada, luoghi del cuore che hanno reso questo soggiorno memorabile e sono diventati parte della mia vita.

CONTENTS

The galactic center: a testing ground for dark matter and gravity theories

I Geodesic motion in the strong-gravity regime

II Testing the Galactic Center with S2 motion

III Appendix

LIST OF FIGURES

LIST OF TABLES

CONVENTIONS, NOTATION AND UNITS

In this thesis I follow the conventions of Refs. [1, 2]. Unless stated otherwise, I use geometrized units ($c = G = \hbar = 1$) and work with the *mostly positive* metric signature $(- + + +)$.

$\alpha, \beta, \gamma, \ldots$	spacetime indices (from 0 to 3)
$i, j, k, \ldots$	3-spatial indices (from 1 to 3)
$V_\alpha W^\alpha \equiv \sum_{\alpha=0}^{3} V_\alpha W^\alpha$	Einstein's notation
$g_{\alpha\beta}\,,\eta_{\alpha\beta}$	curved, flat spacetime metric
$(\,\cdot\,)_{,\alpha} = \partial_\alpha(\cdot) = \frac{\partial}{\partial x^\alpha}(\cdot)$	partial derivative
$(\,\cdot\,)_{;\alpha} = \nabla_\alpha(\cdot)$	Levi-Civita derivative
$\Box(\cdot) \equiv \nabla_\alpha \nabla^\alpha(\cdot)$	Levi-Civita d'Alembertian
$M_\bullet$	mass of Sagittarius A*
R_0	Galactic center distance from Earth

ACRONYMS

BH	black hole
CDM	cold dark matter
CM	center of mass
DEC	declination
DM	dark matter
EHT	Event Horizon Telescope
ETG	extended theory of gravity
GC	Galactic Center
GR	General Relativity
GW	gravitational wave
ISCO	innermost stable circular orbit
LIGO	Laser Interferometer Gravitational-Wave Observatory
LR	light ring
MCMC	Markov Chain Monte Carlo
MLE	maximum likelihood estimator
MW	Milky Way
NIR	near infrared
NS	neutron star
NSC	Nuclear Star Cluster
PDF	probability density function
PN	post Newtonian
PPN	parametrized post Newtonian
QNM	quasinormal mode
RA	right ascension
RV	radial velocity
SgrA*	Sagittarius A^*
SMBH	supermassive black hole
SP	Schwarzschild precession
VLBI	very-long-baseline interferometry
VLT	Very Large Telescope

THE GALACTIC CENTER: A TESTING GROUND FOR DARK MATTER AND GRAVITY THEORIES

1

INTRODUCTION

1.1 GRAVITATIONAL PHYSICS AS A DATA-DRIVEN FIELD

In the last two decades the gravitational physics field has seen an enormous increase in the number of available instruments and observations, turning it from a pure theoretical field to a data-driven one. As a matter of fact, the first experimental proof that black holes (BHs) exist in the Universe can be attributed to Giacconi et al. [3], who observed periodic pulsations in the X-ray that they associated with collapsed rotating stars. However, in the context of BHs physics, the most considerable achievement is surely represented by the detection of the first gravitational wave (GW) signal in 2015 by the Laser Interferometer Gravitational Waves Observatory (LIGO) and Virgo collaborations, produced by the merger of two black holes (BHs) with masses $36^{+5}_{-4}\,M_{\odot}$ and $29^{+4}_{-4}\,M_{\odot}$ [4].

This astonishing result was the first (of many) test showing that the current theory of gravity, General Relativity (GR), correctly predicts the dynamics of very compact objects in the strong field regime. Indeed, GR predicts that massive stars at the end of their life collapse under the gravitational pull and form a BH, a singularity of the spacetime where the laws of physics as we know them completely fail. Chandrasekhar once said:

"The only elements in the construction of black holes are our basic concepts of space and time. They are, thus, almost by definition, the most perfect macroscopic objects there are in the Universe."

Indeed, astrophysical BHs can be seen as very simple objects, whose properties are entirely encoded in only two parameters: mass M and spin j, the latter representing how fast it rotates [1, 5, 6]. This is stated in the so-called "no hair theorem" [7], which is a consequence of more general uniqueness theorems [6, 8, 9]. These latter establish that the only stationary and asymptotically flat solution of Einstein's field equations in vacuum are BHs described by the Kerr metric:

$$\begin{aligned} ds^2 = &-\left(1-\frac{2Mr}{\Sigma}\right)dt^2+\frac{\Sigma}{\Delta}dr^2+\Sigma d\theta^2 \\ &+\left(r^2+j^2+\frac{2Mrj^2}{\Sigma}\sin^2\theta\right)\sin^2\theta d\varphi^2-\frac{4Mrj\sin^2\theta}{\Sigma}dtd\varphi\,, \end{aligned} \tag{1.1}$$

where $\Sigma = r^2 + j^2 \cos^2\theta$, $\Delta = r^2 - 2Mr + j^2$ and j is the dimensionless spin parameter of the BH, defined as $j = J/M$, with J being the angular momentum of the BH (in international units system: $\tilde{J} = Jc^3/G$).

Being stationary and axisymmetric, the Kerr metric admits two Killing vectors: $\mathbf{k} = \partial/\partial t$ and $\mathbf{m} = \partial/\partial\varphi$. The former is associated with the conserved mass M, while the latter is associated with rotations around the axis of symmetry of the BH and leads to have a conserved charge $J = jM$. In order to avoid the formation of naked singularities, i.e., singularities of the spacetime which are not embedded in an event horizon, $0 \leq j/M < 1$. The metric in Eq. (1.1) reduces to the Schwarzschild solution for non rotating BHs in the limit $j = 0$.

When two BHs merge to form a more massive BH, in events that are among the most energetic in the Universe, they emit gravitational radiation in the form of GWs, i.e., ripples of the spacetime that propagate at (almost) the speed of light, already predicted in Einstein's original theory.

The gravitational waveform observed by the LIGO-Virgo collaboration was in agreement at 5σ confidence level with the predicted one from GR, leaving almost no space for misinterpretation. This extraordinary result was a huge breakthrough to understand the strong field regime of gravity, since previous experiments were only carried out in the weak field limit, leaving the way open for alternative theories and speculations.

From that first impressive detection, the number of GW events has dramatically increased, bringing the total number of candidates to more than 90 [10]. Looking at the full catalogue, one can see that these signals can be generated by very different sources: stellar BHs mergers, neutron stars (NSs) mergers, BH-NS mergers and also, quite surprisingly, from the merger of a BH with a compact object which is too light to be a BH and too heavy to be a NS [11]. As always happens when new regimes are explored, the discovery of this mysterious object questioned current models for stellar BHs and NSs formation.

The discovery that BHs indeed exist in the Universe and are not simply mathematical artefacts, opened the way to a new experimental field of research, with several instruments developed in the last decade and many in construction, especially in the context of GWs astronomy [12].

1.1.1 *Beyond GWs*

Despite their incredible power to probe the strong field regime of gravity, GWs are not the only available tools to "look" at very compact objects and unveil the theory that governs their existence. Among others, the Event Horizon Telescope (EHT) played a significant role in the development of the field, producing the first "image" of a supermassive black hole (SMBH). The EHT is a combination of several radio telescopes around the globe aim to create an array such that the angular resolution is sufficiently small to look at the event horizon of SMBHs. Thanks to the very-long-baseline interferometry (VLBI) technique, the EHT works as a telescope whose effective aperture is equal to Earth's diameter. This advanced technology allowed to look directly at the environment in the near proximity of SMBHs, where matter orbits at almost the speed of light, and enabled a new way to test GR [13, 14].

On September 2019, the EHT collaboration announced the first ever image of a SMBH at the center of the elliptical galaxy Messier 87, known as M87* [15–20]. From the analysis of the image, M87* results in having a mass of $(6.5 \pm 0.2_{\rm stat} \pm 0.7_{\rm sys}) \cdot 10^9\,M_\odot$ with a gravitational radius of $3.8 \pm 0.4\,\mu$as, located at a distance of $16.8^{+0.8}_{-0.7}$ Mpc from Earth.

Three years later, the first image of the SMBH at the center of our very own galaxy, Sagittarius A* (SgrA*), was also released [21–26].

In both cases the observed images are in good agreement with the theoretical expectation of a Kerr BH shadow and the authors found no statistical evidence of deviations from GR, confirming the hegemony of the current theory of gravity.

Together with those incredible data sources, the Galactic Center (GC), i.e., the central region of the Milky Way (MW), has also become a very prominent target for astrophysical and astronomical observations in the last decades [27]. The discovery of faint stars, the so-called S-stars cluster, orbiting around SgrA*, allowed to test the weak field limit of gravity in a completely different environment from the Solar System, where previous tests were performed [28]. The motion of stars in the GC will be the main subject of this thesis and it will be explored in depth throughout this work.

Overall, the outstanding number of observational results collected in the last twenty years by means of different experiments have made gravity a research field in which data can no longer be disregarded. On the contrary, experimental evidences should now drive it, wiping out any alternative proposal that is not in agreement with.

Nonetheless, as we will see in the next section, there are still fundamental questions about the theory of gravity and its interactions with other forces in the Universe that can not be answered by means of GR only and need a deeper understanding. Specifically, GR fails, in the sense that it stops being a reliable predictive theory, at both high energy scales, i.e., when one approaches scale lengths comparable with the Planck length ($\ell_P = \sqrt{\hbar G/c} \sim 10^{-35}$m, where we have reintroduced fundamental constants for clarity) and low energy, or cosmological, scales. Since standard quantum field theory approaches have so far failed to provide a theory of gravitation that is valid whatever is the length scale considered, this makes GR somehow an *incomplete* theory. Moreover, the majority of the matter content in the

Universe still remains unknown, elusive to any experiment tried so far to detect it.

1.2 A (VERY) BRIEF HISTORY OF DARK MATTER

"Many of our supposed thousand millions stars, perhaps a great majority of them, may be dark bodies" [29].

The Scottish scientist Lord Kelvin wrote these words in 1884, while trying to estimate the number of dark objects in our galaxy. The idea that the Universe is mostly composed of non-luminous matter was therefore already in the air, and it was firstly postulated by Zwicky [30] while he was studying the galaxies in the Coma cluster and found that the "mass from starlight" was roughly 400 times smaller than the "mass from gravitation". His idea was firstly rejected by most of the scientific community until, forty years later, a series of observations showed that bodies in the inner part of a galaxy were moving with almost the same velocity as outer objects [31, 32]. Those observations explicitly violated the Newtonian theory of gravity, which instead predicts that the velocity of objects in a gravitational field should go as $v \propto r^{-1/2}$.

In order to explain such phenomena, two main solutions were proposed: either Newtonian gravity is not the correct theory of gravity at large scales [33] or a huge amount of matter constitutes most of the galactic content in the form of an halo which does not interact with electromagnetic radiation, i.e., it is *dark* [34, 35].

Fifty years later these proposals still represent our best guesses to explain the inconsistencies between observed data and theory. At the same time, the number of observations confirming that DM somehow exists in the Universe increased consistently since the late 1970s.

As illustrative examples, there are observations with gravitational lensing [36, 37], which showed that the gravitational mass of galaxies is always larger than the luminous mass by a factor $2-4$, and the curious case of the Bullet Cluster [38], consisting of two colliding clusters of galaxies, where the center of mass of the system is surprisingly far from the center of baryonic mass, becoming the strongest evidence in favour of DM existence and discouraging modified theories [39].

Regarding the MW, the luminous and visible disk is thought to be embedded in a much larger halo of DM. This halo is supposed to have a mass in the range $(0.5-3)\cdot 10^{12}\,M_\odot$, roughly 10 times larger than the visible matter content ($M_{\text{vis}} \sim (6-8)\cdot 10^{10}\,M_\odot$), with a local density in the Solar System of $\rho_\odot^{\text{DM}} = 0.39 \pm 0.09\,\text{GeV}/\text{cm}^3$ [40–43]. The latter value depends on the specific model considered to describe the DM halo, and it has been obtained as an average of the results reported in the literature with several different methods [44].

Very recent results based on GAIA satellite third data release have shown that the dynamical mass of the MW may be significantly smaller than previous estimates, reaching the value of $\sim 2 \cdot 10^{11}\, M_\odot$ and finding an absolute upper limit of $5.4 \cdot 10^{11}\, M_\odot$ [45]. Moreover, the MW shows a rotation curve which is not flat anymore, reproducing the so-called Keplerian decline. This would imply also a much smaller DM component in the MW, which would constitute only one third of the total matter content, as opposed to previous estimates.

1.2.1 *The standard cosmological model*

During this 50 years journey looking for DM, a plethora of possible models were proposed. From primordial BHs born due to curvature fluctuations in the early Universe [46, 47] to ultralight particles with mass as low as 10^{-22} eV [48, 49], DM models can span up to 90 order of magnitude in mass, underlying our complete ignorance about it.

However, in order to combine DM observations with the accelerated expansion of the Universe, a standard cosmological model, known as Lambda Cold Dark Matter (ΛCDM) model, was proposed and commonly accepted. It predicts that DM consists of cold, collisionless, dissipationless, non-baryonic matter, which contributes up to 26% of the critical density in the Universe and accounts for 84% of its total matter content [50].

Λ instead represents the cosmological constant, a parameter introduced *ad hoc* in Einstein's field equations to account for the accelerated expansion of the Universe and often known as dark energy [51]. The latter is supposed to represent 68% of the current total energy of the Universe [50]. However, even in the largely accepted ΛCDM model there are some issues that need to be addressed.

Among others, one of the most well-known problems is the so-called cuspy halo problem: while numerical N-body simulations of galaxy clusters showed that CDM halos are characterized by a central core described by a power law density $\rho \propto r^{-\alpha}$, with $\alpha = -1$ in the inner region and $\alpha = -3$ in the outer region [34, 52], the experimental observations seem to favour a constant density core ($\alpha \simeq 0 - 0.4$) [50]. This also implies that numerical simulations predict a central DM density that is much larger than the one observed in galaxies.

This discrepancy questioned the paradigm of CDM, opening the possibility for a different DM modelization, e.g. fuzzy [53], self-interacting [54] or self-annihilating [55] DM, that may suppress the core cusp at small scales [53, 56].

Specifically, ultralight boson fields have gained a lot of attention due to their connection with particle physics, as they emerge naturally in high energy theories, like string theory [49, 57, 58], or as an hidden U(1) gauge boson which is a generic feature of extensions of the Standard Model [59, 60]. Their existence has been investigated in the context of BH imaging, using EHT observations of M87* [61], using rotation curves of low-surface-brightness galaxies (and disfavouring models with $m_\psi \lesssim 10^{-21}$ eV) [62, 63] and using the matter power spectrum revealed by Ly-α forest analysis (again disfavouring masses $m_\psi \lesssim 10^{-21}$ eV) [64–68].

A weaker bound comes from the results of pulsar timing array measurements [69], where the presence of an ultralight boson can emerge as a gravitational potential oscillating at nanohertz frequencies that can affect periodically the times of arrival of pulses from pulsars [70]. Very recently, the detection of the Gravitational Wave Background by the Pulsar Timing Arrays groups has confirmed the presence of low frequency GWs permeating the Universe. Those waves can be explained in the context of pure GR assuming the coalescence of SMBHs in the early Universe. However, the observed signal may also be compatible with the oscillating gravitational potential generated by an ultralight particle [71–73].

Overall, a complete description of DM is still missing, both in terms of its density distribution in galaxies and its nature. In this sense, looking at the inner parsec of our own GC via the motion of stars is a tantalizing possibility of finding out more about DM distribution. This argument will be the main topic of the next chapters.

1.3 STRUCTURE OF THE THESIS

From the famous apple that probably never fell on Newton's head, to matter orbiting at the speed of light near SMBHs, studying how light objects, or *test-particles*, move in proximity of a much more massive body has always been the main tool to understand gravity.

This doctoral thesis is indeed devoted to study the geodesic motion in particular setups, in order to constrain possible signatures induced by specific gravitational backgrounds.

This work is divided in two main parts: the first one is purely theoretical, with possible applications to experiments, and devoted to understand geodesic motion in the strong field regime of gravity, when specific frameworks are considered. Projects presented in this part were all done in collaboration with my supervisor, Vitor Cardoso.

The second part is instead focused on fitting the data of star S2 at the GC, collected using the GRAVITY instrument and other instrumentation at the Very Large Telescope (VLT) in the Atacama desert, Chile. All works involving S2 data have been done in collaboration with the GRAVITY consortium members.

Due to the importance of the latter topic, Chapter 2 will be devoted to describe the GC and its properties, with a specific focus on stars orbiting around SgrA*, since their motion will be used to test its environmental features. In Section 2.6 we will briefly present the experimental apparatus at VLT that allowed to perform the observations used in this work.

In Chapter 3, we will analyse how geodesics in the Schwarzschild spacetime are perturbed if a companion generating a tidal field is added to the background metric.

In Chapter 4, we will present a work in collaboration with Dr. Francisco Duque, where we showed that the appearance of emitting matter accreted by Schwarzschild BHs is entirely dominated by the light ring (LR) and not sensitive to the presence of an event horizon.

The second part of this thesis starts in Chapter 5, where the numerical framework and the methodology used to fit S2 data are presented.

In Chapter 6 the concept of superradiance and the growth of boson clouds around BHs is introduced. In Sections 6.2-6.3 both massive scalar and vector clouds around SgrA* will be considered, with the aim of constraining their mass by making use of S2 orbit.

Finally, in Chapter 7 we considered the specific case of a Yukawa-like modification of the Newtonian potential that emerges as the weak field limit of many different Extended Theories of Gravity (ETG) and represents a deviation due to the presence of a "fifth force" in the Universe. Again, the data collected for S2 will be used to constrain the intensity of such a fifth force at the GC. The latter project is still work in progress and only preliminary results will be presented.

2

THE GALACTIC CENTER AS NEW LABORATORY FOR GRAVITY

2.1 THE GALACTIC CENTRE

The GC of the MW has been a major astrophysical target in the past years and most of its importance resides in the fact that it is relatively close to Earth ($R_0 \sim 8\,\mathrm{kpc}$). This allowed us to study it in depth and perform astronomical observations that are basically impossible in any other galaxy.

The few inner parsecs of the MW are a very populated environment, where one can find young and massive stars [74], hot ionized gas, an HII region, i.e., composed of ionized atomic hydrogen [75] and also an X-rays emitting region which correspond to what is supposed to be a SMBH, SgrA* [76–78]. Due to the presence of interstellar dust, the GC is not observable in the visible spectrum, hence observations are performed at different wavelengths, from microwaves to X-rays and γ-rays.

At a distance of $\sim 1\,\mathrm{pc}$ from SgrA* resides the Nuclear Star Cluster (NSC) that counts up to 6000 stars [79]. The stars in the NSC are mostly old stars, i.e., red giants or supergiants [80], which are expected in this kind of systems.

However, starting with the pioneering observations performed at the end of the 1980s [81, 82], the number of early-type hot stars has consistently increased in the inner parsec of the GC [83–90]. The presence of young stars in a inhospitable environment such as the one around a SMBH is surprising and inexplicable with current theories of stellar formation process [91]. In a nutshell, according to standard scenarios of star formation, the strong tidal shear of the SMBH would prevent the formation of stars, while their young age seems to disfavour the hypothesis that they have migrated there from farther regions. The latter is a very broad research topic and far from the main subject of this thesis and for this reason it will not be explored further (for a comprehensive review we direct the reader to Refs. [91, 92] and references therein).

However, in the context of this work, it is interesting to note that the so-called "Paradox of Youth" [93] might be explained by the presence of DM particles placed inside or in the surrounding environment of stars, as they can significantly alter their evolution [94–99]. Once again, DM might play a significant role in explaining the physics happening at the GC.

2.2 THE RADIO SOURCE: SAGITTARIUS A*

The idea that extremely compact objects could lie at the center of galaxies dates back to 1970, with two pioneering works of Lynden-Bell and Rees [100, 101]. They hypothesized that the release of gravitational energy in the form of radiation due to matter accreting the BH would result in a high energy emission in the core of a galaxy.

In 1974 the first radio emission at the GC was detected [102], in coincidence with the galactic nucleus. This radio emission was lately confirmed by other observations [103] and in 1982 the radio source took the name as we know it today, Sagittarius A* [104, 105]. Constrains from gas dynamics [106–110] and stellar dynamics (particularly with S-stars, see Sec. 2.3 and references there) enhanced the hypothesis of a very compact source with mass $M_\bullet \sim 4 \cdot 10^6 M_\odot$ confined within a very small region of space.

However, the final proof that SgrA* is indeed a BH must come from the observation of a unique feature of BHs, which is the presence of an event horizon. In asymptotically-flat spacetimes, a BH is defined as the set of events from which no future-pointing null geodesic can reach future null infinity. The event horizon is the boundary of this region and for non rotating BHs it has a characteristic size given by the Schwarzschild radius,

$$r_S = \frac{2GM}{c^2}, \tag{2.1}$$

where we have reintroduced fundamental constants for clarity.

In 2022, the EHT Collaboration used the VLBI technology to release the first image of SgrA* at event horizon scale [21–26]. Specifically, they observed the BH *shadow*, namely the dark region below the event horizon surrounded by bright material accreting into the BH and emitting radiation. The intrinsic size of the shadow is mostly determined by the mass-to-distance ratio of the BH and it only depends weakly on the BH's spin [111], while its shape depends on both the spacetime and the modeling of the accretion process.

The subsequent analysis of SgrA* shadow showed that the image is characterized by a bright, thick ring of emission with diameter of $51.8 \pm 2.3\,\mu$as, surrounding a deep brightness depression, in agreement with the predicted shadow of a Kerr BH with mass $M_\bullet = 4.0^{+1.1}_{-0.6} \cdot 10^6\, M_\odot$ at a distance of $\sim 8\,$kpc.

In addiction to this, SgrA* shows flares, i.e., sudden emission of radiation that last for a short time, in both the NIR and X-ray band, orbiting at around $\sim 5\, r_S$ [112–116]. These events are likely due to orbiting parcels of hot plasma, or hot spots. It is still unclear what the cause of these "hot spots" is. Magnetic reconnection in the close vicinity of the BH is a convincing candidate [117] but other possibilities are explored as well [118, 119]. GRAVITY is able to measure the astrometry of these flares with precision of few tens of μas, recently updating its catalogue with 5 new flares observed from 2019 to 2022 [120]. The analysis of both astrometry and polarimetry of all flares combined showed that the compact object at the GC resides almost completely within $R = 4.45^{+0.75}_{-0.65}\, r_S$ ($\sim 0.38\,\mathrm{AU}$) with an enclosed mass of $M_\bullet = 4.2^{+1.2}_{-0.9} \cdot 10^6\, M_\odot$ and inclination of $i_\bullet = 154.9 \pm 4.6^\circ$, ruling out possible extended models, such as the fermionic DM core with typical radius of $\approx 10^{-3}\,\mathrm{pc} \approx 200\mathrm{AU}$ proposed by Ruffini, Argüelles and Rueda [121–123].

These observations allowed for the first time to connect dynamical observations of stars at large scales ($10^3 - 10^5\, r_S$) with measurements at event horizon scales performed by different instruments, resulting in an almost perfect agreement and emphasising the importance of the GC as the perfect testing ground for gravitational physics.

Observations in the millimeter, X-ray, infrared and radio band allowed to put upper limits on SgrA* luminosity ($L/L_{\mathrm{Edd}} \sim 10^{-9}$, being L_{Edd} the Eddington luminosity[1]) and accretion rate ($\dot{M}_\bullet \sim 10^{-9} - 10^{-7}\, M_\odot \mathrm{yr}^{-1}$) [91], showing that the SMBH has low luminosity and it is mostly dormant.

2.2.1 *Testing possible alternatives to the black hole model*

Up to now, observations performed with different instruments seem to favour the hypothesis that SgrA* is indeed a SMBH as predicted by GR [26]. Nevertheless, putting a final word on this topic is a great challenge due to the existence of the so-called BH-mimickers, i.e., compact objects that look exactly like BHs but do not have an event horizon [124].

One of the most common alternatives to the BH paradigm is the wormhole, namely a solution of the Einstein's equations that predicts no singularity at the center but rather a throat connecting either two distant regions of the Universe or two different universes [125, 126]. It has been shown that the presence of a wormhole at the GC would be potentially detectable using star S2 motion, as long as one is able to measure its acceleration with a precision of order $10^{-6}\,\mathrm{m/s^2}$ [127, 128]. However, the diameter of the wormhole's expected shadow would be significantly smaller than the one observed by the EHT and hence it was basically ruled out by the collaboration [26].

---

[1] The Eddington luminosity corresponds to the maximum luminosity that a body in hydrostatic equilibrium can achieve and it is defined as $L_{\mathrm{Edd}} = \frac{4\pi G M m_p c}{\sigma_T}$, where σ_T is the Thompson scattering cross-section of the electron and m_p is the mass of the proton.

A more general model is given by the so called Black Bounce [129], whose metric can be mapped into different models depending on the value of the parameter α, which appears in the radial coordinate as $\tilde{r}^2 = r^2 + \alpha^2$, and reduces to the Schwarzschild metric if $\alpha = 0$. Della Monica and De Martino [130] showed that the current precision in the astrometric measurements of star S2 is not sufficient to detect any deviation from the Schwarzschild metric, making it impossible to distinguish between different models.

More recently, a study by Cadoni et al. [131] tested a non singular BH with super-Planckian hair, where a new length scale ℓ is introduced as a new parameter describing the BH, responsible for the smearing of the central singularity. They found an upper bound of $\ell \sim 0.47 M_\bullet$, while models with $0.2 \lesssim \ell / M_\bullet \lesssim 0.3$ seem to be favoured by observations.

Quite interestingly, also the idea that SgrA* is a boson star has been investigated during the years, both using the motion of S-stars and imaging techniques [132, 133]. Boson stars were firstly introduced in Refs. [134–137] as solutions of the system described by the action:

$$S = \int d^4x \sqrt{-g} \left(\frac{R}{16\pi} - g^{\mu\nu} \bar{\Psi}_{,\mu} \Psi_{,\nu} - \frac{\mu_S^2 \bar{\Psi} \Psi}{2} \right) \tag{2.2}$$

where R is the Ricci scalar, $g^{\mu\nu}$ is the metric describing the spacetime, Ψ is a (complex) scalar field and μ_S is related to the mass parameter of the field m_s via $m_s = \hbar \mu_S / c$ [124]. Those objects are given by new fundamental fields either minimally or non-minimally coupled to gravity, which result in self-gravitating compact objects that may be dark if interactions of the new field with Standard Model particles are weak. Grould et al. [138] investigated possible distinctive features of geodesic motion around boson stars compared to Kerr BHs. They found that orbits become potentially distinguishable for pericenter's distances $\lesssim 30 M_\bullet$, a region of space that is currently unreachable by observations. In Ref. [132], S2 orbit was used to constrain both the mass and the self-interacting coupling constant of the boson field.

In the context of BH imaging, several works have shown how the boson star shadow can be significantly different from that of a BH [133, 139, 140], resulting in a total absence of the central brightness depression. For this reason the mini-boson star model has been ruled out by the EHT collaboration [26]. However, the argument can not be taken as conclusive, since spin, compactness and astrophysical setup can significantly alter the boson star shadow and make it still compatible with EHT results [141].

Throughout this work, we will assume that the compact dark object at the GC is indeed a SMBH described by the Schwarzschild metric, hence non-rotating, and we will not explore further possible alternative models to it.

This assumption is not driven by observations, which are able to place only very broad (and apparently in contradiction) constraints on SgrA*'s spin [142–145], but is rather based on the fact that spin's effect in the motion of S-stars is currently undetectable and hence can be safely neglected. However, this does not imply that SgrA* is actually non rotating, or was not rotating in the past. In fact, as we will see, rotation will play a fundamental role in the development of superradiant clouds at the GC that we will analyse with S2 data.

2.3 THE S-STARS

At a distance of $\sim 0.04 - 0.4\,\mathrm{pc}$ from SgrA* there is another component of the NSC, the so-called S-stars cluster [146–150]. This surprisingly dense group is mainly composed of dwarf B-type stars aged between 6 and $400\,\mathrm{Myrs}$, characterized by randomly distributed orbits with very high eccentricity ($e > 0.5$).

Despite their position may suggest that they are just an extension of the young stellar disk previously mentioned, there are proofs that S-stars must be seen as a completely different component of the GC with respect to other population of stars [146, 147]. Despite several mechanisms have been proposed to explain the formation process of the S-cluster [151–154], none of them is able to provide a complete and satisfying description at the moment.

A possible explanation for the age and location of S-stars was firstly proposed by Hansen and Milosavljevic [155], who hypothesised that an intermediate-mass BH at the GC may be responsible for dragging S-stars to their current location from a more suitable location for stars formation. This idea has been investigated by the GRAVITY collaboration in Ref. [156] with a full parameter study with S2 orbit. For the hierarchical case, i.e., S2 orbiting around the binary SgrA*-BH, intermediate-mass BH with masses $> 2000\,M_\odot$ are largely excluded. When considering the non hierarchical case, meaning that S2 can intersect the intermediate-mass BH orbit, the system becomes chaotic. Despite there are combinations of parameters that still allow the presence of a BH companion to SgrA*, the majority of solutions would disrupt the S-cluster and do not withstand the reality check. A further study on the presence of a possible companion to SgrA* with S2 orbit has been performed by Will et al. [157], who derived bounds on semi-major axis and mass of the BH companion using both numerical and analytical methods.

The monitoring of S-stars around SgrA* has started at the beginning of the 1990s with the New Technology Telescope at VLT [158–160] and it still continues today with the use of more advanced instruments. The observations are performed by two independent groups at the University of California, Los Angeles and at the Max Planck Institute for Extraterrestrial Physics, whose leading scientists, Reinhard Genzel and Andrea Ghez, have been awarded the Nobel Prize in physics in

2020 "for the discovery of a supermassive compact object at the center of our galaxy".

The study of those stars not only improves the current knowledge on the cluster formation, but, most importantly in the context of this thesis, allows to probe the gravitational field of the SMBH with unprecedented accuracy. S-stars are the main tools to look at the inner parsec of the GC and can be exploited to test the nature of the central object, to constrain extended mass distributions around it and to look for possible companions in its vicinity.

Among the S-stars, a particular attention has been devoted to S2 during the last two decades, a $10-15\,M_\odot$ star with apparent magnitude of $K \sim 14$ [161–165].

S2 has a roughly 16 years period and very high eccentricity ($e \sim 0.88$). On May 19, 2018 it passed its pericenter ($r_{\rm peri} \sim 120\,\mathrm{AU} \sim 1.8 \cdot 10^{13}\,\mathrm{m}$) with an orbital speed of $\sim 7700\,\mathrm{km/s}$. This unique event allowed the GRAVITY Collaboration team to detect the Schwarzschild precession (SP) in its orbit for the first time in history, measuring a precession angle which is perfectly compatible with the expectation value from GR [166].

S2 orbit, together with other S-stars, also allowed to improve significantly the estimates for the properties of SgrA*, showing that their motion is completely dominated by a potential generated by a dark object whose mass and distance from Earth are [167]

$$M_\bullet = (4.297 \pm 0.012) \times 10^6 M_\odot \qquad R_0 = 8.277 \pm 0.009\,\mathrm{kpc}\,. \tag{2.3}$$

2.4 TESTING THE ENVIRONMENT AROUND SGRA* WITH S-STARS

Due to their close proximity to SgrA*, S-stars are an incredible tool to look for DM or, more generally, for extended mass distributions at the GC. Indeed the presence of an extended mass around the central BH will induce a retrograde precession in an elliptical orbit, due to the additional acceleration felt by the star, already at Newtonian level [168, 169].

The extended mass considered may be dark, in the sense that it can not be directly observed, and it could be composed of stars, stellar remnants or DM itself. In Ref. [170] the authors made clear that the precession induced by an extended mass can be separated from the SP, not only because they act in opposite directions, but mostly because the former affects the apoastron passage, while the latter becomes detectable (assuming the current instruments' precision) only at periastron. Hence, only a dataset describing a full orbit can successfully characterize the motion, but once the full orbit is known the separation of the two effects becomes duable.

In the context of DM research at the GC, several works have tried to use S-stars to constrain DM models. In the following, we will discuss some illustrative examples.

Lacroix [171] tested the DM spike model using S2 orbit, following the work of Gondolo and Silk [172], where they showed that if a DM halo exists in the galaxy, then it will be accreted by the central BH, forming a dense spike at the GC. The density profile of this distribution is given by

$$\rho(r) = \begin{cases} 0 & r < r_S\,, \\ \rho_{\text{halo}}(R_{\text{sp}}) \left(\frac{r}{R_{\text{sp}}}\right)^{-\gamma_{\text{sp}}} & r_S \leq r \leq R_{\text{sp}}\,, \\ \rho_{\text{halo}}(r) & r \geq R_{\text{sp}}\,, \end{cases} \tag{2.4}$$

where ρ_{halo} is given by a generalized Navarro-Frenk-White profile and R_{sp} is the radial extension of the spike. Using the publicly available data for S2, the author was able to exclude $R_{\text{sp}} \geq 10^3\,\text{pc}$, which can be translated into a bound on the total environmental mass of $\delta M \lesssim 4 - 5 \cdot 10^4 M_\odot$, or $\sim 1\% M_\bullet$.

In Ref. [173] the same dataset was used to constrain the presence of ultralight DM, namely matter in the form of a self-gravitating scalar condensate around the SMBH. This assumption fixes the density distribution of the mass profile δM in terms of the scalar particle's mass m_s. They were able to set an upper bound on the core mass $\delta M \sim 5 \cdot 10^4 M_\odot$ for a fundamental scalar field with mass $m_s \sim 4 \cdot 10^{-19}\,\text{eV}$. For $m_s \gtrsim 10^{-18}\,\text{eV}$ the core is confined inside S2 periastron and it becomes degenerate with the BH mass.

Also the possibility of a self-gravitating halo at the GC made of fuzzy DM has been investigated in Ref. [174]. This model predicts that an ultralight boson field with mass $m_\psi < 10^{-18}\,\text{eV}$ and de Broglie wavelength $\lambda_\psi \sim 1\,\text{kpc}$ forms a central, stationary core (a "soliton") surrounded by an halo that resembles a CDM halo [175, 176]. The radial profile of such cores is approximated by [177]

$$\rho_s(r) = \frac{\rho_0}{(1 + Ar^2)^8}\,, \tag{2.5}$$

where A is related to the core radius r_c via $A = (9.1 \cdot 10^{-2})/r_c^2$ and ρ_0 is the central density of the halo. The core radius can be related with the virial mass of the halo via [178]

$$r_c = 1.6 \left(\frac{m_\psi}{10^{-22}\,\text{eV}}\right)^{-1} \left(\frac{M_{\text{halo}}}{10^9 M_\odot}\right)^{-1/3} \text{kpc}\,. \tag{2.6}$$

The authors of Ref. [174] used a mock dataset to show that future measurements of S2 orbit can provide an upper bound on the boson's mass of $m_\psi \lesssim 10^{-19}\,\text{eV}$ at 95% confidence level.

Regarding more general distributions of matter, the GRAVITY Collaboration [167] used S-stars orbits to test a Plummer density profile [179] around SgrA*, as it represents the simplest model to describe stellar clusters. The parametrization of the Plummer profile is given by

$$\rho(r) = \frac{3 f_{\rm PL} M_\bullet}{4\pi a_{\rm PL}^3}\left(1+\left(\frac{R}{a_{\rm PL}}\right)^2\right)^{-5/2}, \tag{2.7}$$

where the scale length is set to be $a_{\rm PL} = 0.3''$ (roughly correspondent to S2's apoastron) and the enclosed mass within R is $M(\leq R) = f_{\rm PL} M_\bullet (R/a_{\rm PL})^3 (1 + R^2/a_{\rm PL}^2)^{-3/2}$. Fitting the parameter $f_{\rm PL}$, they derived an upper limit for the extended mass enclosed within the apocenter of S2 of $\lesssim 3000\, M_\odot$ or $\lesssim 0.1\% M_\bullet$, currently the most stringent bound on the mass distribution around SgrA*.

Very recently, Shen et al. [180] used publicly available data of S-stars to constrain the spike slope $\gamma_{\rm sp}$ of a generalised Navarro-Frenk-White profile adopting the piece-wise function in Eq. (2.4), for which they found that $\gamma_{\rm sp} \geq 0.92$ is excluded at 95% level. In the same work, the authors also tested the Einasto profile, which is a commonly used DM model that better fits the numerical simulations and can be written as

$$\rho_{\rm Ein}(r) = \rho_0 \exp\left(-\frac{2}{\alpha}\left[\left(\frac{r}{r_s}\right)^\alpha - 1\right]\right), \tag{2.8}$$

where ρ_0 and r_s are the normalisation and scale radius respectively, while α characterises the mass concentration of the DM halo. From this density distribution one can consider different values of the parameters ρ_0, r_s and α coming from numerical works. Specifically they considered both the parameters obtained from the numerical simulations of Navarro et al. [181] and the experimental results coming from the GAIA satellite [182], deriving a upper limit on the spike radius $R_{\rm sp}$. In the former case $R_{\rm sp} \lesssim 30\,{\rm pc}$, while in the latter $R_{\rm sp} \lesssim 60\,{\rm pc}$, at 95% probability.

In this work another setup will be considered, based on the idea that new fundamental massive fields, either scalar or vector, can develop quasi-bound states around BHs creating a "condensate". In usual conditions those fields would decay in time leaving no imprints, but if certain conditions are fulfilled the amplitude of the field can grow exponentially, extracting rotational energy from the Kerr BH. This phenomenon is known as *superradiance* and it will be explored in Chapter 6.

2.5 TESTING ALTERNATIVE THEORIES OF GRAVITY WITH S-STARS

As mentioned in Chapter 1 two possibilities were (and are) explored in order to explain those observational effects that are not compatible with either GR or Newtonian gravity. While in Section 2.4 we explored the possibility that a new form of matter exists, in this section we will focus on the second alternative, i.e., the idea that GR is not the final word on gravity.

When dealing with extension of GR, one must consider that any ETG must reproduce GR results in the weak field limit, i.e., at Solar System scale, where constrains are really stringent [28] and also satisfy the bounds imposed by GWs astronomy [183]. In other words, it must reproduce GR in the intermediate scale lengths range $1\mu\text{m} \lesssim \ell \lesssim 10^{11}$ m, where it is well tested, or provide a meaningful explanation on why possible effects are not visible in such a range [184].

The huge number of theories proposed since 1960, when Brans and Dicke introduced the first scalar-tensor theory [185], makes impossible to do a complete review here, so only a brief summary will be presented (a comprehensive review can be found in Ref. [184]).

The starting point of any ETG is the violation of the Lovelock's theorem [186, 187], which states that GR is the only theory of gravity under some specific assumptions. Specifically, it states:

"In four spacetime dimensions the only divergence-free symmetric rank-2 tensor constructed solely from the metric $g_{\mu\nu}$ and its derivatives up to second order, and preserving diffeomorphism invariance, is the Einstein tensor plus a cosmological term."

Hence, in order to have an alternative theory to GR, or an extension of it, one of the assumptions of Lovelock's theorem must be dropped. For instance, one can add an extra field to the theory, in both a dynamical or non-dynamical way[2], include extra (hidden) dimensions or consider theories that explicitly violate the weak equivalence principle, i.e., assume $\nabla_\mu T^{\mu\nu} \neq 0$.

The latter states that the trajectory of a free falling body is not influenced by its internal structure and composition and it has been tested with increasing precision during the years, reaching the current precision of one part in 10^{15} thanks to the MICROSCOPE experiment [188]. Because of this astonishing finding, theories that violate the weak equivalence principle are usually not considered as viable ones.

What is probably the most natural extension of GR is the inclusion of one or more scalar fields coupled to the gravity sector, which take the name of scalar-tensor theories and whose most general form is Horndeski gravity [189]. In these theories the Newtonian gravitational constant G is a dynamical quantity that depends on the coupling function of the scalar field $\omega(\phi)$ and on its asymptotic value at infinity ϕ_0. In the Brans-Dicke theory, for example, the coupling function ω_{BD} is assumed to be a constant. The larger is the value of ω_{BD} the smaller the effect of the scalar field, making it more and more indistinguishable from GR.

It has been shown that also $f(R)$ theories, namely theories where the scalar curvature R appearing in the Einstein-Hilbert action is replaced

---

[2] Here the difference between dynamical and non dynamical field depends on whether the field is introduced directly in the gravity sector, i.e., modifying the Einstein tensor $G^{\mu\nu}$ and hence the left-hand side of Einstein's equations, or in the stress-energy tensor $T^{\mu\nu}$, such that the identity $\nabla_\mu T^{\mu\nu} = 0$ still remains valid.

by a function of it, are equivalent to some scalar-tensor theories and hence propagate a new degree of freedom [190–192].

Another class of theories are the tensor-vector-scalar theories, where a dynamical four-vector field K^{α} together with a dynamical scalar field ϕ are included in the action [193].

Despite the evidence supporting the SMBH scenario at the GC is extremely strong and has passed more tests than other alternatives [194], testing ETGs with S-stars motion gained a lot of attention recently. The main reason resides in the fact that one is able to test the weak field limit of gravity in a setup and environment that is completely different from the Solar System and studying the nature of their geodesic motion is one of the best strategies to look for modified theories [195]. Indeed, in order to make ETG theories compatible with the intermediate energy scales in which GR has been strongly tested, many of them suffer from a *screening* mechanism [196]. How the latter acts depends on the specific theory considered, but the general idea behind this reasoning is the fact that additional degrees of freedom must remain unseen at local scales, otherwise they would have been already discovered.

As illustrative examples, Borka *et al.* [197] took the SP measurement obtained by the GRAVITY collaboration and compared it with the orbital precession angle of some ETGs, namely power law $f(R)$ theories, non-local gravity and scalar tensor gravity. For the latter, the precession angle induced is roughly 10 times larger than in GR and hence it is not compatible with the observed SP.

In some cases, the modification to the orbital precession is so small that S-stars do not carry any information about the ETG considered. This is the case of Einstein-Maxwell-Dilaton-Axion gravity [198] or Brans-Dicke theory [198, 199].

In Ref. [200] quadratic Einstein-Gauss-Bonnet gravity is considered, deriving an expression for the gravitational redshift as function of the theory coupling parameters, i.e., the coupling between the scalar field and the Gauss-Bonnet invariant $\mathcal{G} = R^2 - R^{\mu\nu}R_{\mu\nu} + R^{\mu\nu\alpha\beta}R_{\mu\nu\alpha\beta}$, where $R_{\mu\nu}$ and $R_{\mu\nu\alpha\beta}$ are the Ricci tensor and the Riemann tensor, respectively.

In this doctoral thesis, we will focus on a specific modification of the Newtonian potential that emerges in the weak field limit whenever a massive field is included in the theory, namely a Yukawa-like potential added to the Newtonian one.

2.6 EXPERIMENTAL APPARATUS AT THE VLT

In this thesis we will make use of astrometric and spectroscopic data of S-stars, specifically S2, collected by the GRAVITY Collaboration members at the VLT in Chile, currently the most advanced visible-light astronomical observatory in the world.

Astrometric measurements were initially performed by the NACO camera between 2002 and 2016, which made use of adaptive optics techniques to resolve the atmospheric turbulence [201]. It was composed by two systems: an adaptive optics system and a Near Infrared (NIR) camera, and it worked at wavelengths of $0.8 - 2.5\,\mu$m.

From 2016 astrometric observations are performed by means of the GRAVITY instrument, from which the collaboration gets its name, a pioneering interferometer that combines the light of all four telescopes at VLT (the so-called VLT Interferometer), each assisted by adaptive optics [202, 203]. The signal needs to be further corrected from atmospheric turbulence and other effects, by making use of a fringe tracker and technologies such as lasers, optic fibers and integrated optics. GRAVITY is able to provide images with a angular resolution of 4 mas, measuring positions of stars with precision of few tens μas and becoming the most sensitive instrument in the field. It works at $2.0 - 2.4\,\mu$m wavelengths.

Spectroscopic measurements, from which one can extract the radial velocity (RV) of stars, are instead performed by SINFONI, a spectrograph located at UT4, one of the four telescopes of VLT [204]. The instrument is composed by two systems: SPIFFI, an infrared integral field spectrograph and the SINFONI-AO (adaptive optics) module. The integral field spectrograph allows to observe the full spectrum of each pixel of an image, measuring the intensity of light at each wavelength and deriving the projected velocity of the observed object from it. Thanks to the adaptive optics module, SINFONI can also correct from atmospheric turbulence. It also works in the infrared band, at wavelengths of $1.0 - 2.5\,\mu$m.

2.6.1 *Towards the future: GRAVITY+*

The current performance of GRAVITY is not the ultimate within reach and a new upgrade of the instrument is on its way [205]. The updated instrument will be equipped with new adaptive optics facilities that will significantly increase the flux injection (roughly a factor 10), making faint targets more likely to be observed. GRAVITY+ is expected to measure the flux from objects with magnitude $K > 22$ mag, in contrast with the current upper bound of $K \sim 15 - 21$ mag.

Moreover, with the new off-axis fringe-tracking mode, GRAVITY+ will be able to measure objects that are far more distant from each others than in the previous experiment, reaching separations up to tens of arcseconds. This improvement would lead to observations of several Active Galactic Nuclei, where SMBHs are expected to lie, up to a redshift $z \sim 3$. Specifically, measurements of SMBH masses at $z \sim 2$ will significantly improve our knowledge on star formation in the Universe, since this redshift value corresponds to the peak of star formation [206, 207].

Regarding the GC, GRAVITY+ is expected to measure fainter stars around SgrA*. The discovery of a closer (and fainter) star will provide a way to measure the Lense-Thirring precession [208], namely the secular precession of the longitude of ascending node and the argument of periapsis due to the rotation of the central mass and the consequent frame dragging effect. This secular precession is proportional to the spin parameter of the BH and hence it will open a way to measure it [209]. Waisberg et al. [210] determined what are the parameters of a potential new star needed to detect the Lense-Thirring precession and those requirements are expected to be fulfilled by GRAVITY+.

Part I

GEODESIC MOTION IN THE STRONG-GRAVITY REGIME

3

GEODESICS AND QUASINORMAL MODES OF A TIDALLY PERTURBED BLACK HOLE

In this Chapter the effect of a tidal perturber placed in the Schwarzschild geometry is investigated.

Tidal interactions play a fundamental role in many astrophysical systems. The best known example are the oceans tides in the Earth-Moon system, which drive tidal acceleration and longer days, but their effects are ubiquitous in astrophysics. In the context of GW astronomy, of tests of fundamental physics and of strong-field gravity, tidal effects are precious. In a compact binary emitting GWs, tidal deformations induced by the companion affect the GW phase. The amount of the dephasing (relative to that of pointlike objects) correlates to the equation of state of the inspiralling bodies, hence a precise monitoring of the GW phase evolution can teach us about the equation of state of NS binaries [211–213]. BHs have a particularly simple equation of state, owing to the uniqueness properties in vacuum GR [214, 215]. Hence, the tidal interactions of compact objects are particularly useful to test the Kerr nature of BHs [124, 216, 217].

Previous studies explored the potential of tidal interactions to constrain the presence of a possible massive companion to the SgrA* source [218]. Specifically, data collected by the GRAVITY collaboration [166, 219] on the orbital motion of the star S2 was used to constrain possible orbital parameters of such a companion. It was also shown that a putative companion may give rise to GW emission potentially detectable with the future space-based interferometer LISA.

The effect of tidal fields in Newtonian orbits is, of course, well studied, specially in the restricted three-body problem (see e.g. Refs [220, 221] and references therein).

The aim of this work is to understand the effects of weak tides in the strong-field region and provide simple analytical results. We are particularly interested on the effect of tides on the location and properties of the innermost stable circular orbit (ISCO), and of the photonsphere. As will be shown in the following, these dictate the high-energy behavior of accretion disks and the relaxation properties of BHs [222–225], and so can be useful smoking-guns of companions. Driven by similar motivations, this problem was studied recently, albeit in less realistic setups. The position of the ISCO was studied in a spacetime describing a binary of extremal charged BHs, in particular the Majumdar-Papapetrou dihole spacetime [226, 227]. The photonsphere of binary BH spacetimes may help in understanding the relaxation or ringdown stage of binaries themselves or hold the key to understanding how the individual components quasinormal ringdown is affected by the companion. For this reason, it has been the subject of recent studies [228–230]. These spacetimes include, naturally, tidal effects, but their effects have mostly been studied numerically. The aim of this work is to provide simple analytical results of strong field phenomena.

This chapter is divided as follows: in Sec. 3.1 a metric describing a tidally perturbed Schwarzschild BH is presented, with a brief introduction about BH perturbation theory. In Sec. 3.2 the specific case of companions fixed at the BH pole is considered. This implies a conservation of the axial symmetry which allowed to compute the analytic expression for the fundamental orbits, ISCO and LR (3.2.1), as well as the quasi-normal modes (QNMs) spectrum (3.2.2). In Sec. 3.3 equatorial companions are studied. Here, the axisymmetry is broken, and analytical results are hard to obtain. Hence, null geodesics (3.3.1), static orbits (3.3.2) and circular timelike geodesics disturbed by the advent of a companion coming from infinity (3.3.3) are all studied numerically.

3.1 SETUP: A BLACK HOLE PERTURBED BY A COMPANION

Consider a non-spinning BH of mass M, perturbed by a companion of mass M_c at a distance R. For far-away companions, the tide is weak and one can expand the geometry around its Schwarzschild value,

$$g_{\mu\nu} = g_{\mu\nu}^{\text{Sch}} + \epsilon\, h_{\mu\nu}\,, \tag{3.1}$$

where ϵ represents the strength of the tidal perturbation, assumed to be small ($\epsilon \ll 1$).

Gravitational perturbation on Schwarzschild background were firstly studied by Regge and Wheeler for polar (or even) perturbation [231] and a few years later by Zerilli, for axial (or odd) perturbation [232]. The different classification reflects how the perturbation $h_{\mu\nu}$ behaves under the parity transformation $(\theta, \phi) \to (\pi - \theta, \pi - \phi)$.

Regge-Wheeler formalism is based on the separation of variables: each component of the metric $h_{\mu\nu}$ can be expressed as spherical harmonic functions, that now take the name of "Regge-Wheeler spherical harmonics" and for spin 0 are defined as

$$Y^{\ell m}(\theta, \phi) = \sum_{m=-\ell}^{\ell} \sqrt{\frac{2\ell+1}{4\pi}\frac{(\ell-m)!}{(\ell+m)!}}\, P_\ell^m(\cos\theta)\, e^{im\phi}\,, \tag{3.2}$$

multiplied by a general unknown function of t and r. Specifically, since they focused on static perturbation, the time dependence of the metric perturbation can be expressed as an oscillatory function $e^{-i\omega t}$. In their work, Regge and Wheeler used a gauge choice such that the four components of $h_{\mu\nu}$ that involve angular derivatives of higher order can be set to zero.

The remaining equations for the radial functions result, in both Regge-Wheeler and Zerilli case, in a single Schröedinger-like master equation that in vacuum reads

$$\left(\frac{d}{dr_*}+\omega^2-V_{Z/RW}\right)\Psi_{Z/RW}=0 \tag{3.3}$$

where the "tortoise coordinate" r_* is defined as $dr_*/dr=1/(1-2M/r)$ and the effective potentials are

$$V_{RW}=\left(1-\frac{2M}{r}\right)\left[\frac{\ell(\ell+1)}{r^2}-\frac{6M}{r^3}\right] \tag{3.4}$$

for the axial sector and

$$V_Z=\frac{2}{r^3}\left(1-\frac{2M}{r}\right)\frac{9M^3+3\lambda^2Mr^2+\lambda^2(1+\lambda)r^3+9M^2\lambda r}{(3M+\lambda r)^2} \tag{3.5}$$

for the polar sector, having defined $\lambda=(\ell-1)(\ell+2)/2$. The master function $\Psi_{Z/RW}$ is instead related with the radial functions describing $h_{\mu\nu}$.

In this work only the polar sector will be considered, which, following Regge and Wheeler approach and using the gauge they defined in Ref. [231], can be written as:

$$h_{\mu\nu}^{\text{polar}}=\begin{pmatrix} fH_0^{\ell m} & H_1^{\ell m} & 0 & 0 \\ H_1^{\ell m} & f^{-1}H_2^{\ell m} & 0 & 0 \\ 0 & 0 & r^2K^{\ell m} & 0 \\ 0 & 0 & 0 & r^2\sin^2\theta K^{\ell m}\end{pmatrix}Y^{\ell m} \tag{3.6}$$

where $H_i^{\ell m}=H_i^{\ell m}(t,r)$, $K^{\ell m}=K^{\ell m}(t,r)$, $Y^{\ell m}=Y^{\ell m}(\theta,\phi)$ and

$$f=f(r)=\left(1-\frac{2M}{r}\right). \tag{3.7}$$

To continue, consider a companion far away, such that the orbital timescale is larger than any other scale in the problem and much larger than the timescale of the internal dynamics of the body. In this regime, one can focus on static perturbations and hence neglect the time dependence of the metric functions.

The vacuum Einstein's field equations for the spacetime in Eq. (3.1) provide equations for the metric functions $H_0(r), H_1(r), H_2(r), K(r)$, that should be solved demanding regularity at the horizon. We will mostly focus on quadrupolar modes (i.e., with $\ell=2$), but the analysis can be easily extended to higher modes. The tr and $\theta\theta$ components of the field equations result in

$$H_1=0\,,\qquad H_2=H_0\,. \tag{3.8}$$

The solution for H_2 which is regular across the horizon $r = 2M$ for $\ell = 2$ is given by

$$H_2 = c_1 \frac{3\,(2M - r)\,r}{M^2} = -\frac{3\,c_1}{M^2}\,r^2\,f(r)\,, \tag{3.9}$$

where c_1 is an integration constant that must be determined by studying the asymptotic behaviour of the metric (3.1) in the presence of an external tidal field. This can be done using the definition of multipole moments developed by Thorne [233, 234].

The effects of an external tidal field are entirely encoded in two symmetric and trace-free tensors: the polar tidal field $\mathcal{E}_L$ and the axial tidal field $\mathcal{B}_L$. The polar tidal field can be expanded in spherical harmonics as $\mathcal{E}_L x^L = r^\ell \sum_m \mathcal{E}_{\ell m} Y^{\ell m}(\theta_c, \phi_c)$, where θ_c and ϕ_c are the angular coordinates of the companion in the BH sky [235].

In the most general case, the asymptotic expansion of the metric will depend on the angular index m. Since in this case it is only needed to find the value of the constant c_1, one can fix $m = 0$ without loss of generality and the metric expansion reads

$$\begin{aligned} g_{tt} = & -1 + \frac{2M}{r} + \sum_{\ell \geq 2} \left(\frac{2}{r^{\ell+1}} \left[\sqrt{\frac{4\pi}{2\ell+1}} M_\ell Y^{\ell 0} + (\ell' < \ell\,\text{pole}) \right] \right. \\ & \left. - \frac{2}{\ell(\ell-1)} r^\ell [\mathcal{E}_\ell Y^{\ell 0} + (\ell' < \ell\,\text{pole})] \right)\,, \end{aligned} \tag{3.10}$$

where M_ℓ are the mass multipole moments.

If one considers the dominant quadrupolar contribution with $\ell = 2$, one can match Eq. (3.10) with the tt-component of Eq. (3.1), and find

$$c_1 = \frac{M^2\,\mathcal{E}_2}{3}\,, \tag{3.11}$$

with the explicit value of the tidal moment $\mathcal{E}_2$ still to be determined. This can be done matching the full metric (3.1) with a Post Newtonian (PN) description of the external spacetime [235, 236]. Parameters chosen in this work are always assumed to be such that the system can be captured by a PN description.

The g_{tt} component in the PN approximation is [236]:

$$g_{tt}^{\text{PN}} = -1 + 2U(r, \theta, \phi)\,. \tag{3.12}$$

Assuming the companion is a PN monopole of mass M_c and centering ourselves in the BH frame, the potential can be written as

$$\begin{aligned} U &= \frac{M}{r} + \frac{M_c}{|\mathbf{r} - \mathbf{R}|} \\ &= \frac{M}{r} + M_c \sum_{\ell m} \frac{4\pi}{2\ell+1} \frac{r^\ell}{R^{\ell+1}} Y^*_{\ell m}(\theta_c, \phi_c) Y_{\ell m}(\theta, \phi). \end{aligned} \tag{3.13}$$

Finally, for $\ell = 2$, it becomes

$$g_{tt}^{\rm PN} = -1 + \frac{2M}{r} + \frac{8\pi M_c}{5}\frac{r^2}{R^3}\sum_m Y_{2m}^*(\theta_c,\phi_c)\, Y_{2m}(\theta,\phi)\,, \qquad (3.14)$$

and comparing (3.14) with the g_{tt} component of the perturbed metric one finds that

$$\mathcal{E}_2 = -\frac{8\pi M_c}{5R^3}\sum_m Y_{2m}^*(\theta_c,\phi_c) = -\frac{8\pi\epsilon}{5M^2}\sum_m Y_{2m}^*(\theta_c,\phi_c)\,, \qquad (3.15)$$

where in the last step the strength of the tidal deformation has been defined as

$$\epsilon = \frac{M^2 M_c}{R^3}\,. \qquad (3.16)$$

Eq. (3.15) agrees with the expression for $\mathcal{E}_2$ in Ref. [237]. The metric functions in (3.6) are now completely determined and they read:

$$H_0(r) = H_2(r) = \frac{8\pi\epsilon}{5M^2}\, r^2 f(r)\sum_m Y_{2m}^*(\theta_c,\phi_c)\,, \qquad (3.17)$$

$$K(r) = \frac{8\pi\epsilon}{5M^2}\,(r^2 - 2M^2)\sum_m Y_{2m}^*(\theta_c,\phi_c)\,. \qquad (3.18)$$

For completeness, we report that the master function in Eq. (3.3) can be expressed in terms of the metric functions (3.17)-(3.18) as

$$\Psi_Z = \frac{r}{\lambda+1}\left[K(r) + \frac{1-2M/r}{\lambda+3M/r}\,(H_2(r) - r\partial_r K(r))\right]\,. \qquad (3.19)$$

3.2 POLAR COMPANIONS

We will specialize our calculations to two specific setups, where the orbits lie in the BH-companion plane or orthogonal to it. Equivalently, and this is the approach we follow, we restrict to equatorial orbits, and place the companion either at the equator or at the pole.

We start with the latter case, imposing the angular coordinates of the companion to be $\theta_c = 0$, $\phi_c = 0$, which preserves the azimuthal symmetry of the BH.

3.2.1 *ISCO and light ring properties*

The four components of the metric with $\ell = 2$ on the equatorial plane are:

$$g_{tt}^{\rm polar} = -f(r)\left[1 + f(r)\,\frac{r^2\,\epsilon}{M^2}\right]\,, \qquad (3.20)$$

$$g_{rr}^{\rm polar} = g(r) - \frac{r^2\,\epsilon}{M^2}\,, \qquad (3.21)$$

$$g_{\theta\theta}^{\rm polar} = g_{\phi\phi}^{\rm polar} = r^2\left[1 - \frac{(r^2-2M^2)}{M^2}\,\epsilon\right]\,. \qquad (3.22)$$

In the equatorial plane, the Lagrangian is found to be

$$2\mathcal{L} = g_{tt}^{\text{polar}}\dot{t}^2 + g_{rr}^{\text{polar}}\dot{r}^2 + g_{\phi\phi}^{\text{polar}}\dot{\phi}^2\,, \tag{3.23}$$

with dots standing for derivatives with respect to the proper time along the geodesic. The Lagrangian is time and azimuth independent, giving rise to two conserved quantities, specific energy E and angular momentum L, such that one can express the quadrivelocities in terms of these constants of motion,

$$\dot{t} = \frac{E}{f(r)(1+\epsilon f r^2/M^2)}\,, \tag{3.24}$$

$$\dot{\phi} = \frac{L}{r^2(1+(2-r^2/M^2)\,\epsilon)}\,. \tag{3.25}$$

The equations of motion are easier to handle via an effective radial potential, which can be obtained substituting (3.24)-(3.25) in the normalization for the quadrivelocity

$$g_{\mu\nu}\,u^\mu u^\nu = \delta\,, \tag{3.26}$$

where $\delta = 0, -1$ for null and timelike geodesics, respectively. One finds,

$$\dot{r}^2 = E^2 - V_\delta(r)\,, \tag{3.27}$$

where

$$\begin{aligned} V_\delta(r) &= \frac{L^2\,(2M-r)\left(2Mr\epsilon - 2r^2\epsilon + M^2(2\epsilon-1)\right)}{M^2r^3} \\ &+ \delta\frac{(2M-r)\,(M^2-2Mr\epsilon+r^2\epsilon)}{M^2r}\,. \end{aligned} \tag{3.28}$$

To understand the ISCO properties, one can expand all relevant quantities in Eq. (3.28) to first order in ϵ, e.g., $r_{\text{ISCO}} = r^{(0)} + \epsilon\, r^{(1)}$, with $r^{(0)} = 6M$ the unperturbed Schwarzschild BH value.

By definition, at the ISCO, $E^2 - V_{(\delta=-1)} = dV_{(\delta=-1)}/dr = d^2V_{(\delta=-1)}/dr^2 = 0$. One finds

$$r_{\text{ISCO}} = 6M(1-256\epsilon)\,, \tag{3.29}$$

$$E_{\text{ISCO}} = \frac{2\sqrt{2}}{3}\,(1+38\epsilon)\,, \tag{3.30}$$

$$L_{\text{ISCO}} = 2\sqrt{3}M(1+7\epsilon)\,, \tag{3.31}$$

$$\Omega_{\text{ISCO}} = \frac{1+491\epsilon}{6\sqrt{6}\,M}\,. \tag{3.32}$$

Note that Ω_{ISCO} is simply $\dot{\phi}/\dot{t}$ evaluated at the ISCO, and it is the angular velocity as measured by far away observers.

High frequency photons or gravitons are well described by null geodesics. Among those, there is one that stands out: a close null

Numerical results

ϵ	r/M	E	L/M
10^{-7}	5.9998	0.94281	3.4641
10^{-6}	5.9985	0.94284	3.4644
10^{-5}	5.9849	0.94317	3.4671
10^{-4}	5.8657	0.94633	3.4932

Table 3.1: Numerical results for the ISCO properties of a tidally deformed BH spacetime. The analytical results (3.29)-(3.32) agree with these values up to the last digit.

geodesic which for non-rotating, isolated BHs is located at $r = 3M$ and defines the LR or, more broadly, a photosphere. In the presence of a polar companion, one finds

$$r_{\text{LR}} = 3M(1+5\epsilon)\,, \tag{3.33}$$
$$b_{\text{LR}} = 3\sqrt{3}M(1-5\epsilon)M\,, \tag{3.34}$$
$$\Omega_{\text{LR}} = \frac{1+5\,\epsilon}{3\sqrt{3}\,M}\,. \tag{3.35}$$

where $b = L/E$ is the impact parameter.

These analytical estimates can be compared to a numerical solution of the geodesic equations. Those results are shown in Table 3.1 for some selected values of ϵ. The perturbative analytical results agree with these numbers to all digits listed. These results can be compared and contrasted to those referring to an extremally-charged BH binary, the Majumdar-Papapetrou geometry. This is done in Appendix A.

3.2.2 *The relaxation of tidally perturbed black holes: light ring modes and quasinormal modes*

Consider now fundamental fields in the BH vicinities, such as gravitational or electromagnetic waves. As stated previously, the dynamical evolution of the field in the simple Schwarzschild geometry is described by Eq. (3.3). Chandrasekhar and Detweiler [238] found a one-to-one mapping from polar perturbation to axial perturbations. Specifically, for even parity there is a radial function that satifies Eq. (3.3) with exactly the same effective potential as of odd parity. Because the effective potential is the same, the spectrum of frequencies ω is also identical in both cases, i.e., the two equations are isospectral [238].

In order to find the spectrum of frequencies ω, one needs to impose boundaries conditions on Eq. (3.3) at both infinity and at the event horizon. Those reads:

$$\Psi = A_{\text{in}}e^{-i\omega(t+r_*)} \qquad \text{for } r_* \to 2M\,, \tag{3.36}$$
$$\Psi = A_{\text{out}}e^{-i\omega(t-r_*)} \qquad \text{for } r_* \to \infty\,, \tag{3.37}$$

which correspond to purely ingoing waves at the horizon and purely outgoing waves at infinity. Eq. (3.3) with boundary conditions (3.36)-(3.37) was firstly solved numerically by Vishveshwara [239] and subsequently in both numerical and quasi-analytical frameworks [238, 240–244].

The resulting spectrum is given by discrete, complex frequencies $\omega_{n\ell m} = \omega_R + i\omega_I$, each for any mode number (ℓ, m) which are called QNMs of the BH. The term "quasi" is needed to underline the dissipative nature of the system, both at infinity and at the event horizon, which results in having a damping time of the mode $\tau_I = \omega_I^{-1}$. The index n is the overtone number, with $n = 0$ representing the fundamental mode, that usually dominates the ringdown signal of GWs.

A good description of the QNMs frequencies is obtained in the eikonal limit, i.e., for modes with $\ell \gg 1$ [223, 245]. In this approximation, the early time ringdown of a signal Ψ is an exponentially damped sinusoid,

$$\Psi \sim e^{-\omega_I^{\mathrm{LR}} t} \sin \omega_R^{\mathrm{LR}} t \,. \tag{3.38}$$

Cardoso et al. [223] showed that both the real and the imaginary part of the frequencies are dictated by the LR, that is, they can be interpreted as high frequency waves trapped at the unstable null orbit. Specifically,

$$\omega_R = \ell \Omega_{\mathrm{LR}} \,, \tag{3.39}$$

where Ω_{LR} is the angular frequency at the LR, and

$$\omega_I = -\left(n + \frac{1}{2}\right) |\lambda_{\mathrm{LR}}| \,, \tag{3.40}$$

where λ_{LR} is the Lyapunov exponent defined as

$$\lambda_{\mathrm{LR}} = \left(\frac{V_r(r_{\mathrm{LR}})''}{2\dot{t}^2}\right)^{1/2} \,. \tag{3.41}$$

The expression for the radial potential V_r can be taken from Eq. (3.28) setting $\epsilon = \delta = 0$ and evaluating it at the LR. A complete derivation of the Lyapunov exponent is provided in Appendix B. Despite being formally valid only for $\ell \gg 1$, the above approximation gives excellent predictions even for lower values of ℓ [246].

The discussion in Sec. 3.1 on gravitational perturbations can be naturally extended to any other kind of perturbation. In this Chapter, we will focus on scalar ($s = 0$) perturbation. The dynamics of the scalar field is described by the Klein Gordon equation:

$$\Box \varphi = \frac{1}{\sqrt{-g}} \partial_\mu \left(g^{\mu\nu} \sqrt{-g}\, \partial_\nu \varphi \right) = 0 \,, \tag{3.42}$$

with $g = \det g_{\mu\nu}$. In the Schwarzschild case, the spacetime admits two Killing vectors ∂_t and ∂_ϕ, and one can use the following anzats for the scalar field:

$$\varphi(t,r,\theta,\phi) = e^{i(m\phi-\omega t)}\frac{\psi_\ell(r)}{r}Y_{\ell m}(\theta)\,. \tag{3.43}$$

Substituting (3.43) into Eq. (3.42) one gets a radial wave equation as in (3.3) with an effective potential:

$$V_s = f\left[\frac{\ell(\ell+1)}{r^2}+\frac{f'}{r}\right], \tag{3.44}$$

where the prime represents a derivative with respect to the radial coordinate.

In general, the time evolution of the system is characterized by a prompt signal, followed by a ringdown which is caused by the "leaky" boundary conditions at the boundaries. In particular, the LR controls the early-time relaxation of BHs via Eqs. (3.39)-(3.40), whereas the late-time ringdown is dictated by boundary conditions (3.36)-(3.37) [124, 223, 224, 245, 247]. For isolated BHs, these two decays coincide and the dynamical properties of BHs are relatively simple.

When new structure is added, such as a change of boundary conditions at large distances or in the near-horizon region, new features appear. In case of a tidally perturbed BH, two stages in the dynamical evolution of fundamental massless fields are expected. Indeed, there is evidence in the literature for such distinctive behavior [229]. Consider, first, the LR relaxation.

Here, the ringdown frequency $\omega_R^{\rm LR}$ and the damping rate $\omega_I^{\rm LR}$ are given by the angular frequency in Eq. (3.35) and the Lyapunov exponent defined in Eq. (3.41), respectively.

For $\ell = m = 2$ those result in

$$M\omega_R = \frac{2\,(1+5\,\epsilon)}{3\sqrt{3}}, \quad M\omega_I = \left(n+\frac{1}{2}\right)\frac{1-10\,\epsilon}{3\,\sqrt{3}}\,. \tag{3.45}$$

We thus have a clear prediction for the changes in the early ringdown of GWs, induced by a companion.

Now, as we mentioned, the late time behavior of the GW signal is sensitive to the entire geometry and not only to the local properties around the LR. In order to assess the QNM spectrum one needs to solve the dynamics. To understand the possible changes, we focus on the relatively simpler problem of a massless scalar field propagating on a fixed, background geometry whose components are given by (3.20)-(3.21)-(3.22).

Since the spacetime keeps its spherical symmetry in this configuration, one can still use the ansatz (3.43) to solve Eq. (3.42) with $g_{\mu\nu} = g_{\mu\nu}^{\rm polar}$. Doing so, one gets a system of differential equations that are not separable anymore. Following Ref. [248], one can solve the problem expanding the box operator in Eq. (3.42) at first order in ϵ:

$$\Box = \Box_{(0)} + \epsilon\,\Box_{(1)}\,, \tag{3.46}$$

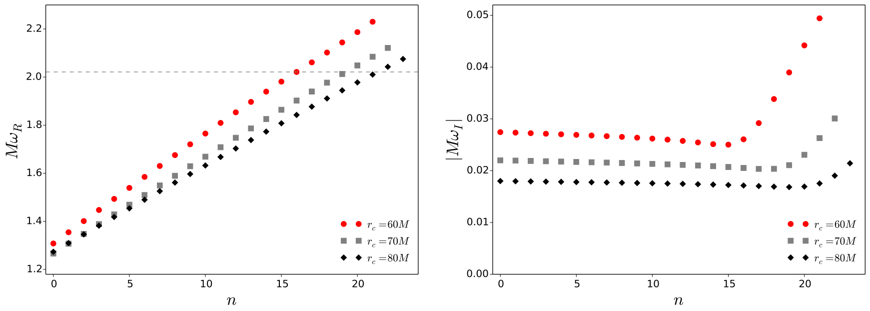

Figure 3.1: Real (left panel) and imaginary (right panel) part of the frequencies for different values of the "cutoff point" r_c in the function $H(r)$. In this case $\epsilon = 10^{-4}$, $k = 100$, and $\ell = m = 10$. The dashed line represents the Schwarzschild frequency (not shown in the right panel since its value $|M\omega_I|^{\rm Sch} \simeq 0.09$ is out of the range chosen).

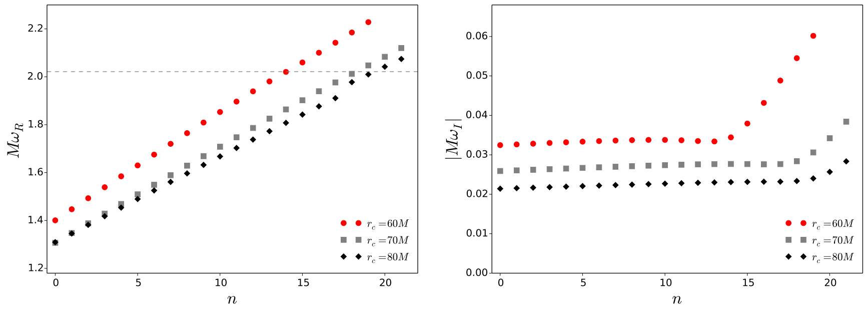

Figure 3.2: Real (left panel) and imaginary (right panel) part of the frequencies for different values of the "cutoff point" r_c in the function $H(r)$. In this case $\epsilon = 10^{-4}$, $k = 2$ and $\ell = m = 10$. The dashed line represents the Schwarzschild frequency (not shown in the right panel since its value $|M\omega_I|^{\rm Sch} \simeq 0.09$ is out of the range chosen).

taking into account that the zeroth order part is separable while the non-separable terms come only from the perturbative correction to the metric. The explicit form of the operator is

$$\begin{aligned} \Box_{(0)}\varphi_{m,\omega}(r,\theta) &= \frac{1}{r^2}\partial_r\left(r(r-2M)\partial_r\varphi\right) \\ &+ \frac{1}{r^2\sin\theta}\partial_\theta\left(\sin\theta\,\partial_\theta\varphi\right) + \left[\frac{r\,\omega^2}{r-2M} - \frac{m^2}{r^2\sin^2\theta}\right]\varphi\,, \end{aligned} \tag{3.47}$$

$$\begin{aligned} \frac{2M^2}{1+3\cos 2\theta}\Box_{(1)}\varphi_{m,\omega}(r,\theta) &= \frac{2M^2-r^2}{r^2}\cot\theta\,\partial_\theta\varphi \\ &+ \frac{2M^2-r^2}{r^2}\partial_\theta^2\varphi - \frac{2(r-2M)^2}{r}\partial_r\varphi - (r-2M)^2\partial_r^2\varphi \\ &+ \left(r^2\omega^2 + \frac{(r^2-2M^2)}{r^2\sin^2\theta}m^2\right)\varphi\,. \end{aligned} \tag{3.48}$$

Since the zeroth-order solution for a given ℓ_0 is $\varphi(r,\theta) = \psi_{\ell_0}(r)/r\, Y_{\ell_0 m}(\theta)$, it is possible and consistent to assume that any term with $\ell \neq \ell_0$ comes from the perturbative correction. Hence, the solution can be expanded such as,

$$\varphi_{m,\omega}(r,\theta) = \frac{\psi_{\ell_0}(r)}{r} Y_{\ell_0 m}(\theta) + \epsilon \sum_{\ell \neq \ell_0} \frac{\psi_{\ell(r)}}{r} Y_{\ell m}(\theta)\,. \tag{3.49}$$

Applying the operator in (3.46) to the solution (3.49) and neglecting terms $\mathcal{O}(\epsilon^2)$ one gets:

$$\begin{aligned} &\Box_{(0)}\left[\frac{\psi_{\ell_0}(r)}{r} Y_{\ell_0 m}(\theta)\right] + \epsilon \sum_{\ell \neq \ell_0} \Box_{(0)}\left[Y_{\ell m}(\theta)\frac{\psi_{\ell(r)}}{r}\right] + \\ &+\epsilon\, \Box_{(1)}\left[\frac{\psi_{\ell_0}(r)}{r} Y_{\ell_0 m}(\theta)\right] + \mathcal{O}(\epsilon^2) = 0\,. \end{aligned} \tag{3.50}$$

Projecting Eq. (3.50) onto $Y_{\ell_0 m}(\theta)$ results in having a single radial equation that can be solved numerically to find the QNM frequencies:

$$\begin{aligned} &\left(\Box_{(0)} - \ell(\ell+1)\right) \frac{\psi_{\ell_0}(r)}{r} \\ + \quad &\epsilon \int_0^{\pi} \Box_{(1)}\left[\frac{\psi_{\ell_0}(r)}{r} Y_{\ell_0 m}(\theta)\right] Y_{\ell_0 m}(\theta) d\theta = 0\,. \end{aligned} \tag{3.51}$$

The asymptotic behavior of the solutions of the above equation are as follows,

$$\psi_{\ell_0} \sim (r-2M)^{2Mi\omega}\,, \qquad r \to 2M\,, \tag{3.52}$$

$$\psi_{\ell_0} \sim e^{\pm\omega r}\,, \qquad r \to \infty\,. \tag{3.53}$$

The boundary condition at the horizon is similar to that of isolated BHs in Eq. (3.36) [244]. However, the boundary behavior at large spatial distances, imposed by the equations of motion, are completely different from those of an asymptotically flat spacetime (cfr. Eq. (3.37)). Indeed, the metric perturbation of the tidally perturbed BH considered in this work is *not* asymptotically flat since the diverging piece of the metric perturbation is used to impose the presence of a companion far away.

In a complete setup, the companion is at finite distance and the spacetime is still flat at spatial infinity. In other words, this description of the binary system is only accurate for distances $r \lesssim R$.

The boundary conditions imposed on us within this setup are similar to those of asymptotically anti-de Sitter or other spacetimes where radiation is confined [244, 249]. Accordingly, the confining nature of the tidal perturbations indicates that one will find a QNM spectrum which differs substantially from that of a single Schwarzschild BH, reflecting the fact that perturbations should be less damped as the only dissipation channel is now the event horizon.

Thus, the unacceptable behavior at large spatial distances must be fixed. This will be done without entering the challenge of matched asymptotic expansions to correctly reproduce the geometry everywhere [229]. Instead, one can simply "cutoff" the tidal effects with an auxiliary function, which is rather arbitrarily chosen to have the form $H(r) = 1/1 + e^{2k(r-r_c)}$. In other words, the regularization procedure consists on the replacement

$$\epsilon \to \frac{\epsilon}{1 + e^{2k(r-r_c)}}\,, \tag{3.54}$$

since the ϵ terms are precisely the ones responsible for the divergence at infinity. In general, results will depend on the smoothness parameter k and the *cutoff point* r_c. It seems reasonable to ask that $r_c \sim R$, whereas k is at least of the order M_c to describe a smooth transition.

Figures 3.1-3.2 show the QNMs for three different values of the cutoff radius $r_c/M = 60, 70, 80$ and $k = 100$ (Fig. 3.1) or $k = 2$ (Fig. 3.2). Notice that what is shown are the first overtones.

Since the idea is to compare with the eikonal limit, we fix $\ell = m = 10$. The tidal parameter is set to $\epsilon = 10^{-4}$, but results for other ϵ are similar.

As already anticipated, the most salient feature of Figs. 3.1-3.2 is that the QNM spectrum of a tidally deformed BH is completely different from that of an isolated BH. Despite our curing the asymptotic behavior artificially, remains of this behavior remain in the perturbation via the existence of quasi-bound states. For example, for a perturbation parameter $\epsilon = 10^{-4}$, one could expect a correspondingly small change in the QNM spectrum. However, as can be seen in the plots, the QNM frequencies change by $\mathcal{O}(1)$.

These features were seen in the past [124, 224, 250, 251] and are connected with the asymptotic properties of the effective potential for wave propagation (and of the corresponding solutions). In fact, the tidal effects act to create a long-distance "well" that traps low frequency radiation. This explains why the damping of the lowest modes (see right panels in Figs. 3.1-3.2) is so much lower than the isolated-BH counterpart. Once the vibration frequency ω_R is sufficiently large for fluctuations to tunnel out through the LR, $\omega_R \simeq \omega_R^{\rm Sch}$ [223], a new channel for dissipation is open, and the damping timescale decreases.

Numerical results are well described by a real component

$$\omega_R \approx \omega_R^{(0)} + \alpha\, n\,, \quad n = 0, 1, 2... \tag{3.55}$$

where the offset $\omega_R^{(0)}$ corresponds to the fundamental mode $n = 0$ of this system, and α is a constant, which decreases increasing r_c and it is independent (or only weakly dependent) on ϵ. Our results indicate a very weak dependence of $\omega_R^{(0)}$ on r_c and ϵ. At very small ϵ the Schwarzschild fundamental QNM is recovered, but it does not correspond necessarily to the fundamental mode of this perturbed spacetime.

This is the spectrum characteristic of a confined system and differs markedly from that of an isolated BH, for which the (real part) of the QNM frequencies asymptote to a constant [244]. For $k = 100$, $\alpha = 0.44$, 0.39, 0.35 for $r_c/M = 60$, 70, 80 respectively, while for $k = 2$, $\alpha = 0.52, 0.48, 0.41$.

Regarding the imaginary part of the QNM frequencies, the fundamental mode are well described by

$$M\omega_I^{(0)} \approx \frac{3M}{5\, r_c\, \epsilon^{1/8}}\,. \tag{3.56}$$

As already stressed, these results are sensitive to the cutoff function and radius chosen. For this reason, we have also investigated the auxiliary function $H(r) = \Theta(r_c - r)$, with Θ being the Heaviside function. In this case there is no explicit dependence on r and k as in (3.54) and nevertheless the QNM spectrum shows the same qualitative behaviour as in Figs. 3.1-3.2. Although the numerical values are slightly different, the overall structure is the same, with real frequencies below the Schwarzschild fundamental mode. Also the transition in the spectrum at $\omega_R \simeq \omega_R^{\rm Sch}$ is recovered, as before. This lends strength to the claim that Figs. 3.1-3.2 represent a good qualitative description of the spectrum.

In conclusion, there are two different stages to consider in the relaxation of binaries [229]. The first one is associated with a prompt ringdown phase and the local properties of the BHs LR, which are affected by the presence of the companion via Eqs. (3.45). This is a local property of the spacetime and hence is not affected by the asymptotic structure at infinity.

The second one is associated with the late time decay of the field which instead strongly depends on the global properties of the spacetime and that can be captured solving Eq. (3.51). Although it is impossible for the naive cutoff procedure to fully capture all the physics, the structure of the spectrum confirms that there is a very different late-time relaxation induced by the different scales in the problem. These features have already been seen in the numerical studies of Ref. [229].

3.3 EQUATORIAL COMPANIONS

The analysis is now specialized to equatorial companions, for which $\theta_c = \pi/2$. Without loss of generality one can impose $\phi_c = 0$. The presence of the companion, which is still assumed to be at rest, breaks the axisymmetry of the metric. As a consequence, the orbits that now lie on the BH-companion plane, have an explicit dependence on the azimuthal angle. For $\ell = 2$, the metric components read:

$$g_{tt}^{\mathrm{eq}} = \frac{f(r)}{2M^2}\left[-2M^2 + f(r)\, r^2\epsilon\,(1+3\cos 2\phi)\right] , \tag{3.57}$$

$$g_{rr}^{\mathrm{eq}} = \frac{g(r)}{2M^2}\left[2M^2 - 2Mr\epsilon + r^2\epsilon + 3r(r-2M)\epsilon\cos 2\phi\right] , \tag{3.58}$$

$$\begin{aligned} g_{\theta\theta}^{\mathrm{eq}} &= g_{\phi\phi}^{\mathrm{eq}} \\ &= \frac{r^2}{2M^2}\left[2M^2(1-\epsilon) + r^2\epsilon + 3(r^2-2M^2)\epsilon\cos 2\phi\right] . \end{aligned} \tag{3.59}$$

3.3.1 *Null geodesics*

Due to the non-axisymmetry of the spacetime, solving geodesic motion analytically is challenging. Instead, one can perform a numerical integration of geodesic equations and find the best fit values for the motion's parameters. Consider first null geodesics and the "shape" of closed null orbits. To calculate these, the geodesic equations are integrated subjected to initial conditions given by,

$$x_0^\alpha = (0, r_0, \pi/2, 0) , \quad u_0^\alpha = \left(u_0^\phi/s, 0, 0, u_0^\phi\right) , \tag{3.60}$$

where $s = \sqrt{-g_{tt}(r_0, \pi/2, 0)/g_{\phi\phi}(r_0, \pi/2, 0)}$. These conditions ensure that the integration is performed for a null particle. Varying the affine parameter τ in an interval $[0, \Upsilon]$ one can fine-tune the value $r_0 \sim 3M$ such that the orbit closes in the same interval. The period (in proper or affine time) Υ is roughly given by $\sim 2\pi/u_0^\phi$.

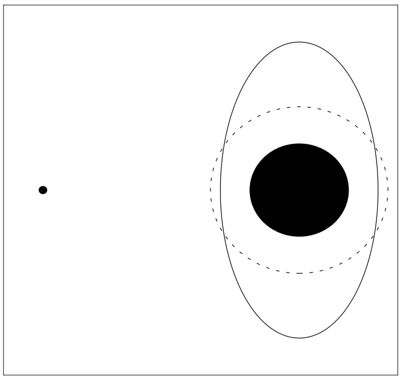

Figure 3.3: Graphic representation of the closed null orbit in Eq. (3.64) (solid line) when the companion is fixed at the equator. The dashed circle represents the LR in the Schwarzschild spacetime. Not in scale.

Our results show an interesting, perhaps expected feature (cf. Fig. 3.3): the null geodesic is no longer circular, but there *are* closed null orbits,

ϵ	$3 - r_0^{\text{num}}/M$	$3 - r_0^{\text{an}}/M$
10^{-6}	1.2×10^{-5}	1.2×10^{-5}
10^{-5}	1.2×10^{-4}	1.2×10^{-4}
10^{-4}	1.2×10^{-3}	1.2×10^{-3}
10^{-3}	1.2×10^{-2}	1.2×10^{-2}

Table 3.2: Coordinate value of r_0 at $\theta = \pi/2, \phi = 0$ for which the null geodesic is closed. Both the numerical result r_0^{num} and the analytical prediction r_0^{an} given in Eq. (3.64) and valid for small ϵ are represented.

which are elliptical. In fact, one can describe them analytically at small ϵ, looking for an expansion with the functional form

$$\begin{aligned} r(\phi) &= 3M - \epsilon(x_0 + A\cos 2\phi(\tau))M\,, & (3.61)\\ \phi(\tau) &= (c_1 + \epsilon c_2)\frac{\tau}{M}\,, & (3.62)\\ t(\tau) &= t_0\tau + \epsilon(t_1 + B\sin 2\phi(\tau))M\,. & (3.63) \end{aligned}$$

The geodesic equations, together with the normalization for quadri-velocities, yield the solution

$$\begin{aligned} r(\phi) &= 3M - \epsilon\left(\frac{15}{2} + \frac{9}{2}\cos 2\phi(\tau)\right)M\,, & (3.64)\\ t(\tau) &= t_0\tau + \frac{45\sqrt{3}}{4}\epsilon\sin 2\phi(\tau)M\,, & (3.65)\\ \phi(\tau) &= t_0\left(\frac{1}{3\sqrt{3}} - \frac{5}{6\sqrt{3}}\epsilon\right)\frac{\tau}{M}\,, & (3.66) \end{aligned}$$

where t_0 is a scale-factor of the affine parameter τ, which has no influence on observables. Table 3.2 reports the values of r_0 (at $\phi = 0$) obtained via numerical integration and the analytical prediction of Eq. (3.64).

Once the radial solution in Eq.(3.64) is known, one can find the parameters of the ellipse in terms of ϵ. Namely, $a = (3 - 3\epsilon)M$ and $b = (3 - 12\epsilon)M$ are the semi-major and semi-minor axes respectively, while the eccentricity is given by $e = \sqrt{\frac{6\epsilon}{1-4\epsilon}}$. Imposing $\phi(\Upsilon) = 2\pi$, one can find the period of the orbit, which in the t-coordinate is

$$T = t(\Upsilon) = 3\sqrt{3}\pi(2 + 5\epsilon)\,M\,. \qquad (3.67)$$

3.3.2 *Timelike geodesics: particles at rest*

The spacetime described by Eqs. (3.57)-(3.59) seems to admit new types of motion. We also find new results concerning static particles,

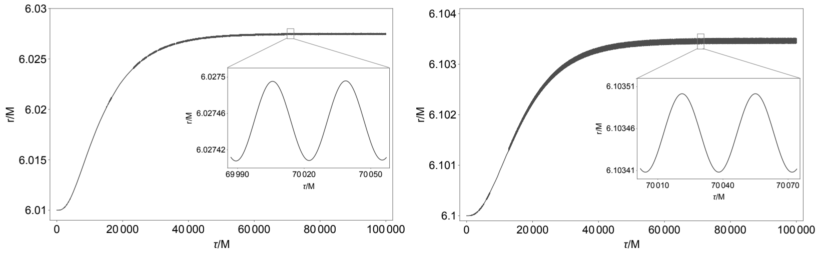

Figure 3.4: Orbital radius of a particle, as function of proper time τ. The particle is placed initially on a circular trajectory of radius $r_i = 6.01M$ (left panel) and $r_i = 6.10M$ (right panel) and perturbed by a companion such that $\epsilon(\tau) = R_0/(1 - e^{-\lambda(\tau+\delta)})$, with $\lambda = 10^{-4}$, $\delta = 10^{-4}$, $R_0 = 200M$. The inset shows the behaviour of the radial coordinate on shorter timescales for $r_i/M = 6.01, 6.10$. Oscillations with periodicity $\sim 45\,M$ can be seen, which correspond to orbital periods $\sim 90\,M$ in the (r, ϕ)- plane, in accordance with Fig. 3.5 and Table 3.4. Note that at early times there are some gaps in the oscillatory behaviour. These gaps are due to a mere technical problem in drawing the plots and have no physical meaning.

ϵ	r_s^{num}/M	r_s^{an}/M
10^{-6}	80.037	79.713
10^{-5}	37.507	37.195
10^{-4}	17.766	17.479
10^{-3}	8.604	8.372

Table 3.3: Location r_s where static equilibrium of particles in a tidally deformed BH spacetime is possible. Numerical values are denoted r_s^{num} and can be compared against the analytical prediction r_s^{an} of Eq. (3.69).

i.e., orbits which satisfy $\dot{r} = \dot{\phi} = 0$. At $\tau = 0$, we set initial conditions $\phi = 0$, $r = r_s$ and the radial motion is governed by

$$\dot{r}^2 = E^2 + (2M - r_s)\left(\frac{1}{r_s} - \frac{2(r_s - 2M)\epsilon}{M^2}\right) . \tag{3.68}$$

Solving $\dot{r} = \ddot{r} = 0$, one finds:

$$r_s = \left(\frac{2}{3} + \frac{1}{(2\epsilon)^{1/3}}\right) M + \mathcal{O}(\epsilon) , \tag{3.69}$$

$$E^2 = 1 + \mathcal{O}(\epsilon) . \tag{3.70}$$

Estimates in Eq. (3.69) can be tested solving numerically the geodesic equations imposing $u_0^t = \sqrt{-1/g_{tt}^{\text{eq}}(r_s, \pi/2, 0)}$ as initial condition. Table 3.3 reports the results obtained with these two approaches, with an overall good agreement.

The result in Eq. (3.69) is also in agreement with a Newtonian solution of the problem [252, 253]. Consider a binary system with masses M and M_c separated by a distance R. Let a test particle with mass μ be located at distance r from the primary mass M. The test particle will be at rest if the gravitational force exerted by the primary mass is compensated by the tidal force exerted by the secondary mass on the primary. Namely,

$$\frac{M\mu}{r^2} = \frac{M_c\mu}{(R-r)^2} - \frac{M_c\mu}{R^2} \simeq \frac{2M_c\mu r}{R^3}\,, \tag{3.71}$$

where one can exploit the fact that $r/R \ll 1$. Solving this equation for r one finds:

$$r = R\left(\frac{M}{2M_c}\right)^{1/3}\,, \tag{3.72}$$

which is proportional to the value of r_s in (3.69) if one substitutes in it the definition of ϵ given by Eq. (3.16).

3.3.3 *Timelike geodesics: disturbing circular motion*

An analytical description of the ISCO is challenging to find in these non-symmetric setups. Without attempting to find an analytical solution to this problem, it is interesting to show what happens when one disturbs circular orbits by slowly lowering a companion coming from infinity. This process could mimic for example the inspiral of a binary and its effect of the disk of one of them.

To do so, a toy model of a time-dependent perturbation is used, described by $\epsilon = M^2 M_c/R^3$ with R a time-dependent quantity,

$$R(\tau) = \frac{R_0}{1 - e^{-\lambda(\tau+\delta)}}\,. \tag{3.73}$$

This behavior is meant to describe the appearance of a companion in a smooth way, so that one is able to study the transition from no-companion to a tidally distorted BH. The results discussed below are not dependent on δ, and converge to a universal behaviour for small λ. We set $\delta = M^2\lambda = 10^{-4}M$, so that initially the companion is at $R \sim 10^8 R_0$ and asymptotically approaches $R = R_0$. We focus on $R_0 = 200M$.

The particle is initially placed at $r = r_i$ and perform a circular orbit, i.e.,

$$u_0^\mu = \left(\sqrt{\frac{r_i}{r_i - 3M}}, 0, 0, \frac{1}{r_i}\sqrt{\frac{M}{r_i - 3M}}\right)\,, \tag{3.74}$$

and the geodesic equation is numerically integrated up to $\tau \sim 10\lambda^{-1}$.

As the companion approaches its asymptotic location R_0, the particle is pulled to a slightly larger orbital radius, while the orbits become slightly eccentric, as shown in Fig. 3.4. Assuming that the orbit is

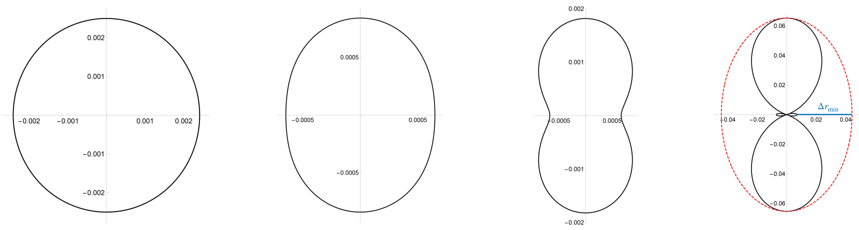

Figure 3.5: Orbits in the $(r(\tau) - r_i, \phi(\tau))$ plane for initial radii (from left to right) $r_i/M = 6.01, 7, 10, 25$ in a single period T. For graphical reason in the first case the radial coordinate is obtained as $r(\tau) - 6.025M$. In the last panel the blue line represents $\Delta r_{\rm min}$ mentioned in the main text.

elliptic, one can extract the local maximum and minimum values of the radial coordinate to compute an eccentricity-like quantity

$$e = \sqrt{1 - (r_{\rm min}/r_{\rm max})^2}\,, \tag{3.75}$$

as well as its period T. Specifically, these quantities are evaluated for a single period T and extracted when the companion is almost steady, so at late times. Results are reported in Table 3.4. Note that T is to a good precision the orbital period of a particle in circular motion, given by Kepler's law. Not surprisingly, e increases as the particle moves away from the BH and get closer to the companion. Specifically, it scales as

$$e \propto \left(\frac{r_i}{M}\right)^{1.78}\,. \tag{3.76}$$

In fact, the motion is not really eccentric in these coordinates. For large r_i, the motion acquires a peanut-like shape, as shown in Fig. 3.5. If one takes the $\phi = 0$ direction as the apoapsis $r_{\rm min}$ direction, then deviations from a perfect elliptic shape are of order $\Delta r_{\rm min}/r_{\rm min} \sim 10^{-3}$ (blue line in the last panel of Figure 3.5). As a consequence, the eccentricity-like parameter e can still be considered an adequate measure of deviation from circularity.

Likewise, both the period T and the shapes of the orbits in Figure 3.5 are unaffected by the change in the final position. The only relevant difference is in the numerical values of $r_{\rm min}$ and $r_{\rm max}$, as well as in their ratio. Indeed, as expected, these values become larger (smaller) if the companion is at $R_0/M = 100$ (300). As a consequence, orbits have a larger (smaller) value of the parameter e, though its scaling with r_i is still well described by Eq. (3.76). To be more precise, the exponent is 1.71 for $R_0 = 300\,M$ and 1.88 for $R_0 = 100\,M$.

The final position of the particle, due to the presence of a companion, is dependent both on the strength of the perturbation and the initial radius. Denoting by $r_{\rm fin}$ the average value between $r_{\rm min}$ and $r_{\rm max}$,

r_i/M	T/M	e
6.01	92	0.0055
6.05	95	0.0055
6.10	96	0.0057
6.50	104	0.0063
7	116	0.0074
8	142	0.0099
10	198	0.0148
15	363	0.0317
20	562	0.0522
25	786	0.0759

Table 3.4: Period T in time coordinate and eccentricity-like parameter $e = \sqrt{1-(r_{\rm min}/r_{\rm max})^2}$ of the orbits performed by a timelike particle starting with initial radius r_i when the companion is slowly approaching from infinity to $R_0 = 200M$.

extracted when the companion is now steady, one finds that for radii $r_i \geq 10\,M$ the displacement $\Delta r = r_{\rm fin} - r_{\rm i}$ is given by

$$\frac{\Delta r}{r_i} \approx A\left(\frac{r_i}{M}\right)^3 \epsilon\,, \tag{3.77}$$

with the constant A of order unity.

3.4 DISCUSSION

The understanding of accretion disks or of the orbital motion of stars is a fundamental aspect in the interpretation of astrophysical observations. In addition, the location and properties of the LR around BHs are crucial in the understanding of the dynamics in the strong-field regime. Thus, peculiarities in motion in deep strong-field regions could indicate either new physics or simply the presence of an unseen companion [218]. Motivated by this possibility, we studied the geodesic motion of both null and timelike orbits when tidal perturbations induced by an external companion are present.

There are several new features of tidally distorted BH geometries relative to BHs in isolation. When the orbital plane is orthogonal to that of the BH-companion, one is able to analytically quantify the linear deviations in the characteristic orbits induced by the companion. Specifically, with respect to the unperturbed configuration, the LR has larger radius and orbital frequency, while the ISCO is located closer to the BH and, consequently, has a larger angular frequency. In this framework the QNM frequencies are also obtained for the $\ell = m = 2$ modes, finding that the ringdown frequency (the damping rate) is shifted to a slightly larger (smaller) value with respect to that of a Schwarzschild BH.

Instead, studying the late-time behaviour of the field showed that the structure of the modes of such a geometry is noticeably different from that of a single BH and is instead typical of confined systems. These properties had already been observed previously [229]. However, in order to correctly capture all the physical properties of the relaxation stage, it is necessary to construct a spacetime which correctly reproduces the asymptotic behaviour at infinity [229]. Further investigations in this direction are left for future work.

On the other hand, when orbits lie in the same plane as that of the BH-companion system, a numerical study is needed. It has been shown that the LR is still a closed orbit but with an elliptical shape characterized by eccentricity and axes proportional to ϵ (cfr. Fig. 3.3). Timelike orbits displayed a similar behaviour but other effects took place as well. The companion induces a relaxing of the orbit of point particles, which moves toward larger radii and are tidally distorted as seen in Fig. 3.5. The possibility for the spacetime to admit static orbits was also explored and an expression for their initial radius r_s was found, in agreement with the Newtonian treatment of the problem.

Recently, this work has been extended to a more general setup describing a binary in a tidal environment generated by a Kerr BH by Camilloni et al. [254]. Their results generalise (and recover, in the weak tidal field limit) the estimates found above for the photonsphere.

4

THE LUMINOSITY OF MATTER ACCRETED BY A SCHWARZSCHILD BLACK HOLE

In most of the physical processes involving BHs there is a notion of a stationary "background" spacetime, on which "matter probes" move and evolve. These setups are particularly appropriate at providing detailed information of the geometry and underlying theory. In these circumstances, the geometry is effectively fixed and can be inferred by measuring accurately the motion of probes.

Examples are ubiquitous. The gravitational multipole moments of the Earth, for example, can be determined in this way by studying the motion of orbiting satellites [255–257].

In astrophysics, accretion flows around supermassive, otherwise isolated BHs, can also be well described as flows on a fixed Kerr background. The reason is simply that the matter content and density outside the BH is so small that its backreaction can be neglected for all practical purposes [215]. Thus, a fixed Kerr geometry is sufficient to understand and study the physics associated with observations by the EHT [15] or GRAVITY [166].

The appearance of BHs, when illuminated by external sources, such as an accretion disk, is of course dictated by those photons reaching far-away observers [258–263]. It is therefore no surprise that the separatrix between photons escaping to infinity and those eventually plunging into the BH horizon plays an important role in BH imaging.

In particular, photons sent in from large distances with a decreasing impact parameter will be deflected with a larger angle, probing stronger-gravity regions before being scattered to observers far-away. Below a critical impact parameter, such photons simply fall onto the BH. At the critical value of impact parameter, the photon circles the BH an infinite number of times. These trajectories asymptote to a closed, unstable, photon orbit, which we will call the LR. As we have seen in the previous Chapter, for non-rotating BHs with mass M, it is located at areal radius $r_{\text{LR}} = 3M$.

The LR thus controls the amount of information that one can gather, related to the BH geometry. But this fact concerns only matter external to the LR itself. Here, we are interested in the appearance of luminous matter as it falls down a BH.

As mentioned in Chapter 2, such events seem to occur periodically in the vicinities of the SgrA* source [116, 264]. Similar events were also reported in the past in connection with the Cyg X-1 BH. In particular, dying pulses from BH accretion were discussed in the context of Cyg X-1, some years ago [265, 266]. The dynamical appearance of bright sources was studied by Zeld'ovich and Novikov [267], Podurets [268], and Ames and Thorne [269], but the analysis was based on a number of approximations and restricted to spherically symmetric gravitational collapse. Here, we investigate how a pointlike source, emitting GWs or electromagnetic waves, fades out as it is accreted by a Schwarzschild BH.

4.1 LIGHT-RINGS: THE KEY TO COMPACT OBJECTS

Consider a non-spinning BH of mass M described in standard Schwarzschild (t, r, θ, φ) coordinates

$$ds^2 = -f dt^2 + f^{-1} dr^2 + r^2 (d\theta^2 + \sin^2\theta d\varphi^2)\,, \tag{4.1}$$

with $f = 1 - 2M/r$. Take high-frequency radiation (both electromagnetic or GWs), which is described by null geodesics in this limit. The motion of null particles in the Schwarzschild spacetime is given by

$$g_{\mu\nu} \frac{dx^\mu}{d\lambda} \frac{dx^\nu}{d\lambda} = 0\,, \tag{4.2}$$

where λ is the affine parameter of the geodesic. Due to spherical symmetry, one can set $\theta = \pi/2$ $(\dot{\theta} = 0)$ and obtain the following equations of motion:

$$\begin{aligned} \dot{t} &= \frac{E}{f}\,, \\ \dot{\varphi} &= \frac{L}{r^2}\,, \\ \dot{r}^2 &= E^2 \left(1 - f\frac{b^2}{r^2}\right) \equiv V\,, \\ b &= \frac{L}{E}\,, \end{aligned} \tag{4.3}$$

where b is the impact parameter of the null particle, E and L are conserved energy and angular momentum of the null particle, respectively. Dots stand for derivative with respect to the affine parameter of the geodesic λ.

The radial equation in (4.3) allows for a closed circular geodesic at some $r = r_c$. Circularity requires that

$$\dot{r} = \ddot{r} = 0\,, \tag{4.4}$$

and one finds

$$\begin{aligned} b^2 &= \frac{r_c^2}{f}\,, \\ r_c f' - 2f &= 0\,, \end{aligned} \tag{4.5}$$

where the prime represents a derivative with respect to the radial coordinate. In Schwarzschild spacetime, the solution is

$$r_c = 3M\,, \qquad b_{\rm crit} = 3\sqrt{3}M\,. \tag{4.6}$$

This orbit has an angular frequency, measured by asymptotically far observers, $\Omega_{\rm LR} \equiv d\varphi/dt = 1/(3\sqrt{3}M)$. Such coordinate position defines, on the equatorial plane, a so-called LR. Since this is a spherically symmetric spacetime, it defines more broadly a photon sphere. This is the only closed null orbit outside the horizon and high-frequency photons or GWs can be trapped at this location. However, as shown in Appendix B, it is an unstable trapping, since any small perturbation δ will grow exponentially as

$$\delta \sim e^{\lambda_L t}\,, \tag{4.7}$$

with $\lambda_L = 1/(3\sqrt{3}M) = \Omega_{\rm LR}$. In other words, a null ray slightly displaced off the light ring will orbit on a timescale $t \sim \log\delta/\lambda_L$. During this timescale, the null particle does a number of orbits

$$n \sim \frac{\Omega t}{2\pi} = -\frac{\log\delta}{2\pi}\,, \tag{4.8}$$

close to the LR. For further details and refined estimates see Chandrasekhar's classical work [238].

Due to the above trapping properties and critical impact parameter for absorption onto a BH, LRs play a crucial role in our understanding of BHs. As already mentioned, LRs are responsible for features of BH imaging but they also dictate the stability of the spacetime [270, 271].

Moreover, the timescale reported in Eq. (4.7) dictates the "relaxation" stage of BHs, after they have been perturbed and vibrate at the QNMs frequencies. In Chapter 3 it has been shown that the ringdown stage can be interpret as high-frequency waves trapped at the LR that fade out at infinity. The real part is determined by the LR frequency $\Omega_{\rm LR}$, while the imaginary one is related with the instability timescale, namely how fast particles can escape form the LR [223, 240, 272].

In the following we will show that the LR also dictates the late-time behaviour of the luminosity of sources falling into the BH, as observed at infinity.

4.2 HOW DO BRIGHT BODIES FADE OUT?

4.2.1 *An outward-pointing beam*

In order to understand how bright objects fade out when falling into a BH, one can start with a single, collimated light source which free falls from rest into a Schwarzschild BH, and points radially outward.

In Schwarzschild coordinates, one finds the emitter four-velocity to be

$$v_e^\mu = \frac{dx_e^\mu}{d\tau_e} = \left(\frac{1}{f}, -x_e, 0, 0\right) , \tag{4.9}$$

$$x_e \equiv \sqrt{\frac{2M}{r_e}} . \tag{4.10}$$

In these conditions, the position of the laser pointer as function of proper time is

$$r_e = 2M \left(-\frac{3\tau_e}{4M}\right)^{2/3} , \tag{4.11}$$

and the coordinate time at the laser pointer position is given implicitly by

$$\frac{dt}{d\tau_e} = \frac{1}{f} = \frac{1}{1 - 2M/r_e} . \tag{4.12}$$

Assume that a photon is emitted at proper time τ_e with proper frequency $\omega_e = -(v_\mu k^\mu)_e$, with k^μ being the photon 4-momentum and v the laser pointer four-velocity. The photon is observed when it intersects the observer world-line, and it is observed with frequency $\omega_o = -(v_\mu k^\mu)_o$. For a static observer at large distances from the BH, the spacetime is flat and its four-velocity is $v_o^\mu = (1, 0, 0, 0)$. Radial null geodesics are described by the momentum

$$k^\mu = E\left(\frac{1}{f}, 1, 0, 0\right) , \quad k_\mu = E\left(-1, \frac{1}{f}, 0, 0\right) . \tag{4.13}$$

and thus

$$\omega_o = \omega_e(1 - x_e) . \tag{4.14}$$

If one wants to compute the redshift as seen by a distant observer as function of the time coordinate t, one needs to take into account that the null particle is being emitted by a source which is getting closer to the horizon, and which also needs time to reach the observer. An outward-directed photon obeys

$$\frac{dt_{\text{travel}}}{dr} = \frac{1}{f} . \tag{4.15}$$

Integrating the equation above allows to find the arrival time of the null particle as measured by a far-away observer

$$t_o = t_e + (r_o - r_e) + 2M \log \frac{r_o - 2M}{r_e - 2M} . \tag{4.16}$$

Using Eqs. (4.14) and (4.16) one can obtain the behaviour of the emitter when it is close to the BH by solving

$$\frac{dr_e}{dt_e} = -\sqrt{\frac{2M}{r_e}} f_e , \tag{4.17}$$

for sources close to the horizon, $r_e \sim 2M$.

We find that $t_e \sim -2M \log(r_e - 2M)$ and substituting it in Eq. (4.16) one gets $r_e - 2M \propto e^{-t_o/(4M)}$, $\omega_o \sim r_e - 2M$ and thus a redshift

$$\omega_o \sim e^{-t_o/(4M)}\,, \tag{4.18}$$

at late times. The total luminosity dE_o/dt_o can be calculated in a similar way. At late times it behaves as $dE_o/dt_o \sim e^{-t_o/(2M)}$.

Figures 4.1-4.2 show the numerical solution of this problem. An emitter starts falling at $r_i = 30.65M$ and emits 20000 null particles, one every (proper) time interval $\delta\tau = 4 \times 10^{-3}M$. This corresponds to a monochromatic source of frequency $\omega_e = 2\pi/\delta\tau$. An observer located at $r_o = 100M$ collects these photons. Our numerical results show that at late times the frequency as measured by far-away observer decreases exponentially as described by Eq. (4.14).

Note that the frequency measured by the observer at r_o is always *redshifted*. The luminosity, i.e., energy per second collected by this same observer, measured in units of proper luminosity, is shown in Fig. 4.2. At late times, it falls exponentially as just described.

4.2.2 *An isotropically-emitting star*

Most sources are not collimated and do not appear as laser beams. The simplest object that can simulate a realistic source is a isotropically emitting one. Assume this source emits in its rest frame with total luminosity $\mathcal{L}_e$ while it falls radially toward the BH. To compute the observed luminosity at infinity, one needs to track any particle emitted. Again, since the system is spherically symmetric, one can assume the particle is on the equatorial plane $\theta = \pi/2$ without loss of generality.

Null geodesics are characterized by their energy E and their angular momentum L computed at infinity, that can be obtained from

$$\begin{aligned} p_\varphi &\equiv r^2\dot{\varphi} = L\,, & (4.19)\\ -p_t &\equiv f\dot{t} = E\,, & (4.20)\\ \dot{r}^2 &\equiv f(p_r)^2 = E^2 - f\frac{L^2}{r^2}\,. & (4.21) \end{aligned}$$

Those conserved quantities need to be related with observables in the local free-falling frame of the particle, where they have energy ω_e and are emitted with an angle α with respect to the radial direction.

One finds the redshift and the impact parameter to be

$$\begin{aligned} \omega_o &= \omega_e\,(1 + x\cos\alpha)\,, & (4.22)\\ b \equiv \frac{L}{E} &= r_e\frac{\sin\alpha}{1 + x\cos\alpha}\,. & (4.23) \end{aligned}$$

A detailed calculation on how to obtain Eqs. (4.22)-(4.23) is reported in Appendix C. One can study the infall of such a source shooting null particles uniformly distributed in α and collecting them at some radius r_o where the observer is located.

Those particles for which

$$b < b_{\rm crit} = 3\sqrt{3}M\,, \tag{4.24}$$

will fall into the BH and are not considered in the calculation.

Eqs. (4.22)-(4.23) can be solved for the redshift of particles with $b = b_{\rm crit}$. One finds

$$\frac{\omega_o}{\omega_e} = \frac{r_e^3 + \sqrt{2M}\sqrt{r_e^5 - b^2 r_e^2(r_e - 2M)}}{2Mb^2 + r_e^3}\,, \tag{4.25}$$

The solution is shown in Fig. 4.3. It shows that as the star falls, radiation with near-critical impact parameter is blueshifted for values of around $1.2 - 1.3$ for most of the fall (in particular, it is larger than 1.2 for $6.7M < r_e < 49M$). The blueshift peaks at $r_e = 12M$ and crosses unit at $r_e = b$, i.e.,

$$\left.\frac{\omega_o}{\omega_e}\right|_{\rm max} = \frac{4}{3}\,, \quad r = 12M\,, \tag{4.26}$$

$$\frac{\omega_o}{\omega_e} = 1\,, \quad r = 3\sqrt{3}M\,, \tag{4.27}$$

in agreement with previous results [273].

Now one can distribute 1600 particles uniformly in α and reproduce the same analysis of the laser beam. Our results are summarized in Figs. 4.1-4.2. The first important aspect is that light from an isotropically-emitting object (or other general source) reaches far-away observers with a range of different redshifts as Fig. 4.1 shows. The lower part of the region agrees very well with the collimated "beam" curve, meaning that the most redshifted null rays are those emitted radially.

On the other hand, blueshifted rays can also be produced during infall. For example, a ray with a near-critical impact parameter can be bent by π, i.e., it can make a U-turn and be reflected back. This is similar to what was observed in Ref. [261], where they studied a moving source and a mirror, and they found null rays to be blueshifted. Note that as the critical impact parameter is approached, the rays linger longer closer to the light ring, and take longer to reach the observer.

The redshift distribution discussed above and reported in Fig. 4.1 refers to particles collected in the whole sky, at fixed radial coordinate $r_o = 100M$. To understand what specific observers see, one can select among all of the outgoing photons, those that reach the observer with $\cos\varphi > 0.99$ (which are labeled with "$\varphi = 0$") and those with $\cos\varphi < -0.99$ (which are labeled with "$\varphi = \pi$"). The corresponding distribution is shown in Fig. 4.4 for observers at $r_o = 100M$. Observers with "$\varphi = 0$" see the BH behind the star, and the three lie on the same axis. Observers with "$\varphi = \pi$" see the star behind the BH.

At early times, the former observer ("$\varphi = 0$") only sees radially-moving particles because they reach the observer first. In terms of actual observations, this initial stage will not be visible to an observer at infinity, who only sees late-time phenomenology. After some time, photons with near critical impact parameter have circled the BH and can reach the observer too. Those photons will be blueshifted, leading to a sort of "phase transition". The delay time of blueshifted particles with respect to the first ones is $\Delta_1 t \sim T_{\rm LR}/2 + 60M \sim 76M$, with $T_{\rm LR}/2$ being the time it takes to circle the LR and come back in the opposite direction.

On the other hand, an observer on the opposite side of the BH would see the first null particles to be always blueshifted, since the observer see a moving, approaching source, a time $\Delta_2 t \sim 60M$ after the first signal arrives at the $\varphi = 0$ observer. These estimates do not take into account Shapiro delay, but the estimate $\Delta_1 - \Delta_2 \sim T_{\rm LR}/2 \sim 16M$ should be more reliable. All these features are apparent in Fig. 4.4.

The total luminosity $\mathcal{L}$, which corresponds to the flux integrated across sky, is shown in Fig. 4.2 and follows the same trend. Note that due to the finite number of "photons" used in the numerical study, the total luminosity shown in Fig. 4.2 is not smooth. The jagged features carry no physical information and are purely a result of the numerical method used to estimate the luminosity. We opted to "bin" 20 particles at a time, explicitly checking that larger binnings produce smoother luminosity functions, as it should. For realistic sources the true curve is single-valued and smooth, while the numerical approximation is thick and rough and approximates the real curve when the flux in the rest-frame increases. At late times our results are consistent with a decay $\mathcal{L} \sim e^{-t_o/(3\sqrt{3}M)}$.

4.2.3 *An isotropic, scalar emitting body*

Once the geometric optics limit is mastered, one can try to solve the full problem of wave propagation on Schwarzschild background. To do so, we consider a toy model representing a source with scalar charge q emitting scalar waves. This results in having a Klein-Gordon equation for massless scalar field sourced by the trace of the stress energy tensor T describing a pointlike source with mass m_e, vibrating at a (constant) proper frequency ω_e. The source thus emits spherically symmetric waves in its rest frame [274, 275] and it couples to the scalar field though a scalar charge q,

$$\Box\Psi = q\,T\,\sin\left(\omega_e \tau_e(t)\right)\,. \tag{4.28}$$

Denoting the worldline of the pointlike body by

$$z^\mu(\tau_e) = \left(t_e(\tau_e), r_e(\tau_e), \theta_e(\tau_e), \varphi_e(\tau_e)\right), \tag{4.29}$$

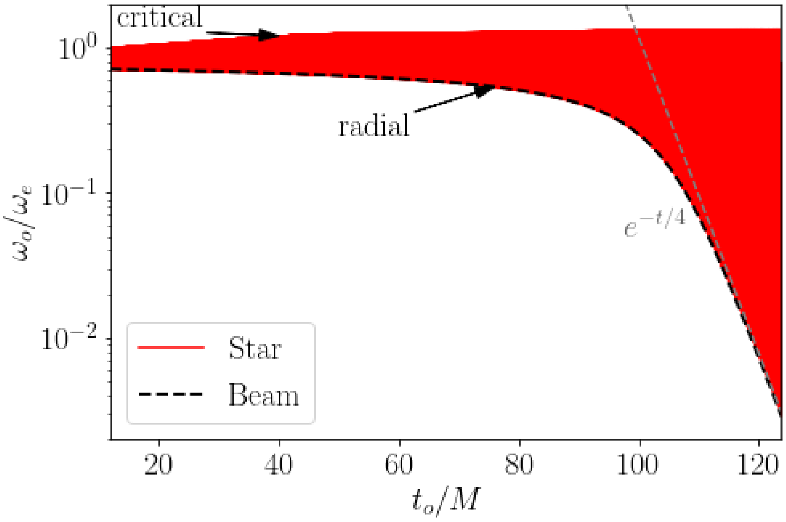

Figure 4.1: Redshift of two different sources as they plunge radially into a Schwarzschild BH, emitting null particles (e.g. photons, gravitons) of fixed proper frequency ω_e. The source, located in the equatorial plane at $\theta = \pi/2$, $\varphi = 0$ begins from rest at infinity, but (for numerical purposes) starts emitting only when it crosses $r = 30.65M$. **Beam:** this source emits only radially outwards. The observer is located at $r_o = 100M$, $\theta = \pi/2$, $\varphi = 0$, and receives particles whose frequency/energy decreases with time. At late times, the frequency ω_o measured by the observer decays exponentially as $\omega_o \sim \omega_e e^{-t/(4M)}$, according to our analytic prediction (4.14). **Isotropic star:** the second source is a pointlike "star" emitting isotropically in its local rest frame. At a fixed instant, far-away observers distributed along the sphere at $r_o = 100M$ receive a wide range of redshifts. The lower part of the curve is due to radially propagating null particles, whereas the top part of the curve is due to particles with a near critical impact parameter $b_c \approx 3\sqrt{3}M$ that linger close to the LR, which can be blueshifted [261].

the explicit form of the stress-energy tensor is

$$T^{\mu\nu} = m_e \int_{-\infty}^{+\infty} \frac{\delta^{(4)}(x^\alpha - z(\tau)^\alpha)}{\sqrt{-g}} \frac{dz^\mu}{d\tau} \frac{dz^\nu}{d\tau} d\tau \,, \tag{4.30}$$

where one can take $m_e \ll M$. Since all results scale trivially with q and m_e, both are set to 1 henceforth. The scalar star has non-zero angular momentum L_e and it is put along the equatorial plane, again with no loss of generality due to spherical symmetry.

Its equations of motion are

$$\frac{dr_e}{dt} = -\sqrt{E_e^2 - \left(1 - \frac{2M}{r_e}\right)\left(1 + \frac{L_e^2}{r_e^2}\right)} \,, \tag{4.31}$$

$$\frac{d\varphi_e}{dt} = \frac{L_e}{E_e} \frac{1 - 2M/r_e}{r_e^2} \,. \tag{4.32}$$

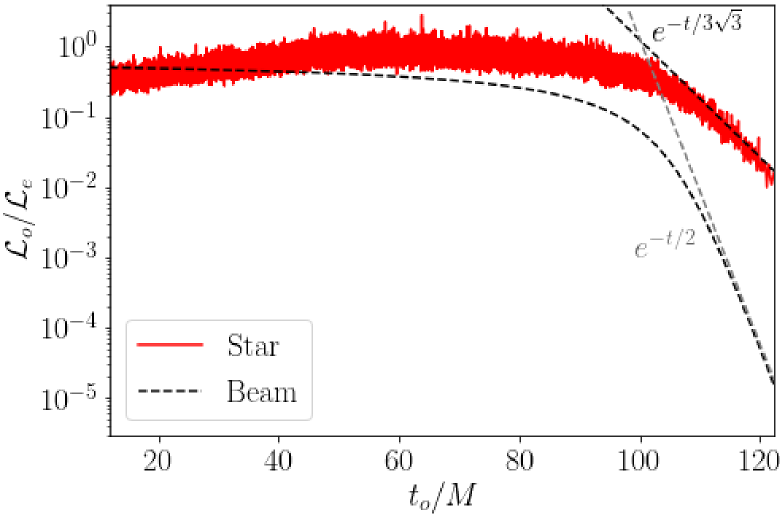

Figure 4.2: Normalized luminosity ($\mathcal{L} = dE/dt$) of the two different sources discussed in Fig. 4.1. The observed luminosity of the radial beam scales as $\mathcal{L} \sim e^{-t/(2M)}$ at late times, again in agreement with our prediction. The luminosity of the isotropic star was calculated by "binning" null particles in packets of 20, to avoid large scatters. At late times, the luminosity is dominated by those particles lingering on the LR, hence $\mathcal{L} \sim e^{-t/(3\sqrt{3}M)}$.

Eq. (4.28) is solved using a time domain code that smoothens the pointlike source and was previously developed, tested and reported [276–280].

Fig. 4.5 shows the total luminosity for this system for a monochromatic source with $M\omega_e = 2.5$, with and without angular momentum. The flux of energy at spatial infinity is computed through

$$\begin{aligned}\dot{E}^{\infty} = \mathcal{L}_o &= \lim_{r\to\infty} \int_{^2S} d\Omega \sqrt{-g} T^{tr}_{\Phi} = \\ &= \lim_{r\to\infty} \int_{^2S} d\Omega\, r^2 \sin\theta\, \partial_t \Phi\, \partial_r \Phi\,. \end{aligned} \tag{4.33}$$

Even though the source is now emitting radiation whose wavelength is comparable to the BH size, the late time behavior is still described by the exponential decay, $\mathcal{L}_o \propto e^{-t_o/(3\sqrt{3}M)}$, independently of whether the body falls with non-zero angular momentum or not.

The luminosity per solid angle at different angular positions is presented in Fig. 4.6. The global LR decay is the same but one can notice the presence of additional structure. In particular, there are periodic oscillations whose period may differ for different observers. Their frequency is a multiple of half of the frequency of the LR, $M\omega_{\rm LR} \approx 0.192$ (corresponding to a period $T_{\rm LR} \approx 32.6M$). Each of these LR pulsations is succeeded by a sharp, fast transition, lasting for $\sim 5M$, a behavior and a timescale that are not fully understood.

As we might have anticipated, the spectral content is dominated by blueshifted radiation emitted in the past with a near-critical an-

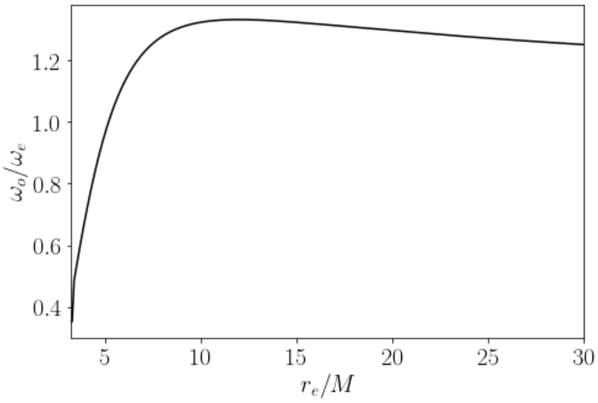

Figure 4.3: The blueshift distribution of photons with near-critical impact parameter, emitted from a object freely-falling onto a BH. The blueshift is maximum, $\omega_o = 4\omega_e/3$ at $r_e = 12M$, and is unit at $r_e = 3\sqrt{3}M$ (see also Ref.[273]).

gle, which is absorbed by the LR and re-emitted later. Referring to Fig. 4.3, such radiation is blueshifted to $\omega_o \sim 1.2 - 1.3\omega_e$, in this case corresponding to $M\omega_o \sim 3.0 - 3.1$ during most of the infall.

4.2.4 *A gravitational-wave emitting binary*

As final case, a binary system emitting GWs as it falls into the BH is considered. This system is composed of two masses orbiting each other, for instance stellar BHs, both small enough to be negligible compared to the BH mass. Thus, the binary system can be studied as a perturbation of the background geometry and can be represented by two pointlike particles with stress energy tensor given by Eq. (4.30). In this way, it constitutes a hierarchical triple system [280].

Emission of GWs can be studied using Teukolsky's master equation [281]

$$\mathcal{L}_s \Psi = \mathcal{T} \,, \tag{4.34}$$

where $\mathcal{L}_s$ is a second-order differential operator, s refers to the "spin weight" of the perturbation field ($s = -2$ for GWs), and $\mathcal{T}$ is a spin-dependent source term [281] built from the stress-energy tensor in Eq. (4.30). A detailed explanation on how to solve Teukolsky's equation is given in Refs. [279, 280].

For the binary motion, we follow the framework of Cardoso *et al.* [280] and take the binary to be on a very-eccentric orbit around its center-of-mass (CM), while the CM itself is on a radial plunging trajectory, according to Eqs. (4.9)-(4.11). The motion of the binary around its CM can be parametrized by

$$r^{\pm} = r_{\rm CM}(t) \,, \qquad \theta^{\pm} = \theta_{\rm CM}(t) \,, \tag{4.35}$$

$$\varphi^{\pm} = \varphi_{\rm CM} + \epsilon \sin(\omega_e \tau_e) \,, \tag{4.36}$$

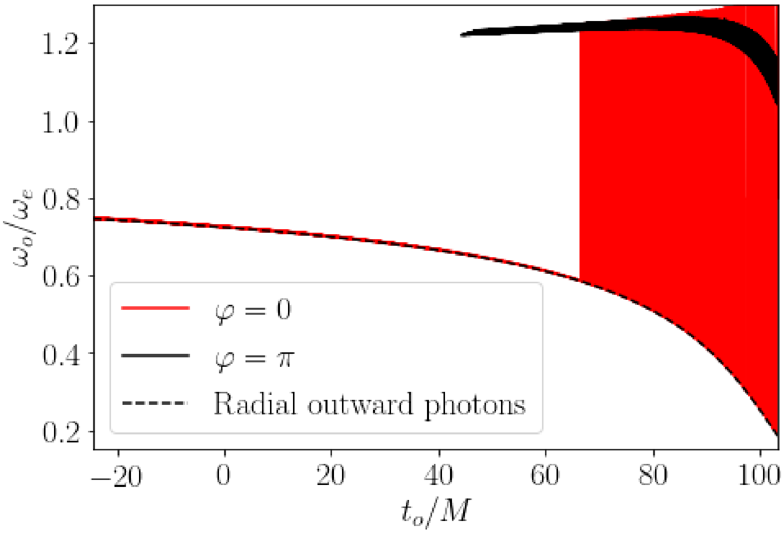

Figure 4.4: The redshift distribution of light emitted by an infalling (isotropic) star as measured by observers at $r = 100M$ on the infalling axis. For $\varphi = 0$ the star is between the BH and the observer, whereas observers at $\varphi = \pi$ only see the star due to gravitational lensing, as the BH sits between them and the star. Note the delay with which the $\varphi = \pi$ observer receives the first signal, with respect to $\varphi = 0$. Note also that the signal is mostly Doppler blueshifted for $\varphi = \pi$, as the observer sees light emitted from an approaching source. Some of the details of this figure, in particular the graininess and isolated points, are due to insufficient number of null particles being sent from the star.

where ± refers to the two bodies composing the binary and $\epsilon = \epsilon(r_{\rm CM})$ defines the axis of the very eccentric ellipse defined by the binary

$$\epsilon = \left(1 - \frac{2M}{r_{\rm CM}}\right) \frac{\delta r}{r_{\rm CM}}\,, \tag{4.37}$$

where δr is the proper length of the axis of the binaries' motion around its CM and it is chosen to be $\delta r = 0.1M$. Results are independent of the choice of δr. These two point particles both enters as source term of Teukolsky's equation (4.34).

The flux of energy carried by GWs at infinity is given by

$$\dot{E}^{\infty} = \lim_{r\to\infty} \frac{r^2}{4\pi} \int_{^2S} d\Omega \int_{-\infty}^{\infty} dt' \Psi(t', r, \theta, \varphi)\,. \tag{4.38}$$

Fluxes at different angular locations are shown in Figs. 4.6-4.7.

Notice that the emission mechanisms and details vary depending on the angular position of the observer. For example, it is impossible to decouple the motion of the CM induced by GW emission from that of the binary itself. Nevertheless, all these sources give rise to the same late time global exponential decay $\mathcal{L}_o \sim e^{-t/(3\sqrt{3}M)}$.

The peculiar nature of gravity is manifest on the low-frequency components in Fig. 4.7: these are CM contributions. Superposed on these

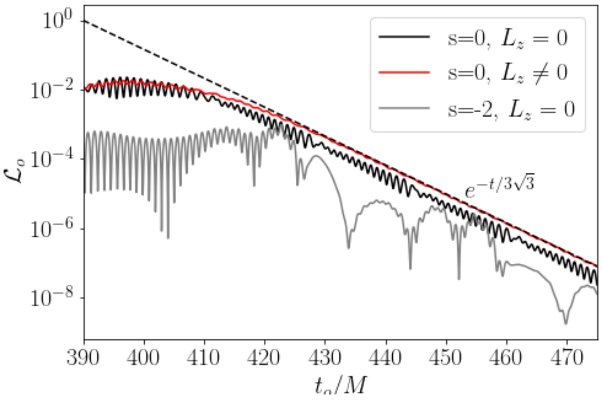

Figure 4.5: Total luminosity in scalar waves ($s = 0$) and GWs ($s = -2$) from a source plunging into a Schwarzschild BH, and emitting at fixed proper frequency $M\omega_e = 2.5$. The source is located on the equatorial plane at $\theta = \pi/2$, $\varphi = 0$ and starts from rest at $r = 35M$. We consider both a radial ($L_e = 0$) plunge and one with finite angular momentum ($L_z \neq 0$, for which we fix $L_e = 3.0M$). For both types of waves and plunging process, the luminosity follows the exponential decay dictated by the LR $\mathcal{L}_o \sim e^{-t/(3\sqrt{3}M)}$ at late times, as seen in the geometric optics limit for the isotropic star in Fig. 4.2. The differences in features between scalar and GWs can be explained by the difference in the source structure. In particular, the low frequency oscillations in the GW spectrum are due to the plunge of the CM of the binary system (they are a consequence of the first 5 multipolar modes). The high-frequency content of the signal for both scalar and GWs is dominated by frequencies around $M\omega_o \sim 3.0$, higher than the proper frequency of emission by a factor ~ 1.2, consistent with these waves having been emitted during infall and trapped at the LR, cf. Fig. 4.3.

low-frequency components one can find the high frequency signal from the binary. Thus, for certain directions, such as $\theta = \pi/2, \phi = 0, \pi$, the high frequency contribution coming from the binary dominates the spectrum whereas for other angles the signal is controlled by the lower frequencies coming from the plunge of the CM.

4.3 TESTING THE EVENT HORIZON

Previous results strengthen the point of view that the late-time appearance of BHs illuminated by matter is tightly connected to the photon sphere. Light rings control the way that dynamical processes look like to an outside observer. One can take this program a step further and ask how these results change when the near horizon region changes, or equivalently if the source is affected close to or within the LR. To do so, two different types of processes are considered:

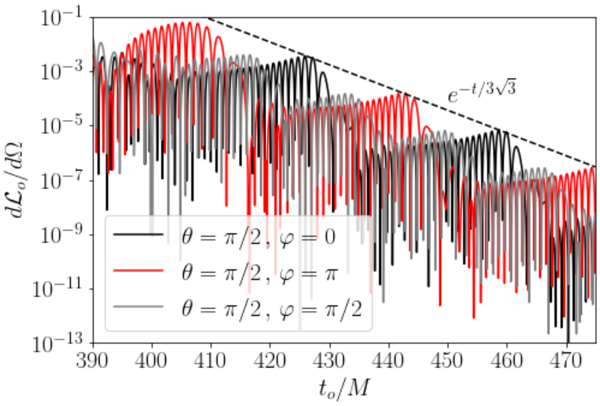

Figure 4.6: Energy flux for a scalar source plunging radially into a BH (from $r_e = 30M$ as in Fig. 4.5), extracted at specific angular positions on the equator. Results are normalized in units of qm_e. All signals exhibit the same global exponential decay dictated by the LR as seen in Figs. 4.2 and Fig. 4.5. Observers see now a periodic structure, whose period may differ for different observers (notice that at $\varphi = \pi/2$ the period is half that at $\varphi = 0, \pi$). These features could mimic "revivals" reported in the literature [265, 266], but are independent of the motion of source, and rather related only to the LR properties. Once again, the high frequency content of the spectrum corresponds to waves with of $M\omega_o \sim 3.0$, in accordance with the blueshift predictions of Fig. 4.3.

- First, the source is turned off after it reaches a selected radius (e.g. $r = 4M, 2.5M$). This could represent a merging binary before its CM plunges on the BH or - in case of scalar waves - it simply stops shining. Results are summarized in Figs. 4.8-4.9. The spectrum is mostly independent of the cutoff radius as long as this is located close or inside the LR, for both scalars and GWs. Overall, the flux of energy only shows a mild change in the amplitude. The late-time decay is still given by the exponential law observed previously, which reinforces the interpretation that it really describes waves trapped close to the LR (which accumulated during the infall), and are slowly leaking out to infinity (and the horizon). This result also indicates that two different compact objects with similar LR structures may be hard to distinguish based on observations of matter surrounding it, whether they possess a horizon or not.

- In the second case the source becomes suddenly brighter, increasing its proper luminosity after it falls within some radius. Fig. 4.8 shows results when the proper luminosity is increased by a factor of 100. As before, the late-time behavior decay is unaltered and the change in the luminosity measured by far-away observers is small when the burst occurs inside the LR.

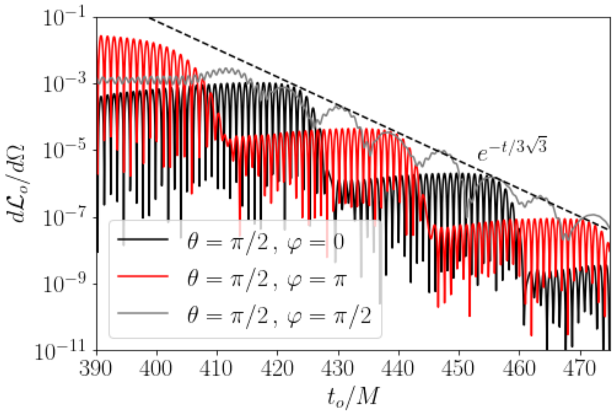

Figure 4.7: Same as Fig. 4.6, but for a source emitting high-frequency GWs. The source is a binary, and is plunging radially onto a massive BH, while emitting GWs of proper frequency $M\omega_e = 2.5$. The frequency of the signal measured by far away observers is blueshifted to $M\omega_o \sim 3$.

The results of this section indicate that it is indeed the LR and not near horizon details that are relevant for how matter accreted onto a BH appears to distant observers at late times. In other words, *what happens inside the light ring stays inside the light ring*.

4.4 DISCUSSION

In this Chapter the role of the LR was investigated in the context of BH imaging, namely the appearance of matter accreted onto a Schwarzschild BH. The LR can be seen as a region where high-frequency waves are trapped with a timescale given by the LR frequency itself $\sim 3\sqrt{3}M$ or larger. When a source emitting radiation falls into the BH, it transfer its energy to the LR, heating it up. When the source crosses the photonsphere, the transfer of energy is maximum. Afterwards, the source gets redshifted and the emission is dominated by emission from the LR. An external observer located far away from the source will only see the late-time appearance of infalling matter as it is dominated by the LR cooling process: the signal would be slightly blueshifted with respect to its proper frequency and would have a luminosity decay given by

$$\mathcal{L} \sim e^{-t/(3\sqrt{3}M)}\,. \tag{4.39}$$

This behavior is best understood within a null-particle approach. Instead, literature on waves around BHs usually discusses a mode analysis where the late-time behavior is dominated by quasinormal ringdown and power-law tails [242, 244]. GWs, for example, are emitted by coherent motion of sources, and usually excite only a few of the modes (specifically, the LIGO-Virgo-Kagra Collaboration has only

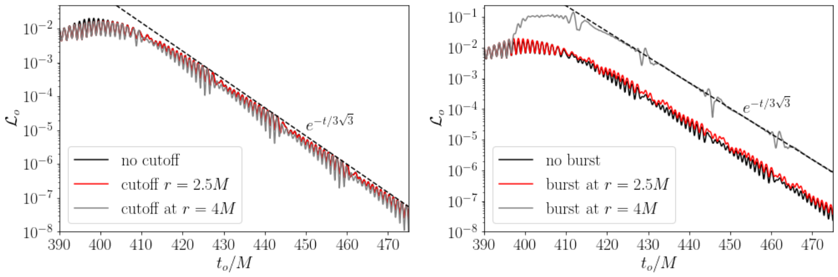

Figure 4.8: **Left panel:** Luminosity in scalar waves for the system studied in Section 4.2.3. Now, the source is turned off below a certain radius (either $r = 2.5M$ or $r = 4M$). When the source is turned off inside or close to the LR, the flux is nearly unchanged, as it is controlled by waves emitted in the past and lingering close to the photonsphere. **Right panel:** Luminosity for the scalar system studied in Section 4.2.3 but whose source is suddenly increased by a factor of 10 at the same radii as in the left panel. In flat spacetimes, this would correspond to a luminosity 100 times higher. However, since the process takes place close to the LR, the luminosity is very weakly affected and has the same global exponential decay. As expected, when the increase in amplitude occurs deep inside the light ring, the increase in the luminosity is less significant.

confirmed the presence of the fundamental $\ell = m = 2$ mode in its ringdown catalog [282, 283]).

For high-frequency sources, however, a large number of multipoles are excited. The QNM frequencies at large mode number ℓ, are described by $\omega_{\rm QNM} = \Omega_{\rm LR}\,(\ell + 1/2 - i/2)$ [244]. In the ringdown stage the field amplitude is $\Phi \sim \sum_\ell e^{-i\omega_{\rm QNM} t}$. If one plugs the asymptotic expression above in this sum over all the multipoles, one obtains a ringdown stage with a global modulation given by $\Phi \propto e^{-\Omega_{\rm LR}\,t/2}$, which in the Schwarzschild case corresponds exactly to the observed decay in luminosity ($\mathcal{L} \propto |\Phi|^2$). In other words, both the geometric optics and wave propagation results are compatible.

Finally, tails are extremely challenging to observe in the presence of these sources, as their amplitude is expected to be many orders of magnitude below the ringdown signal [284]. Consequently, they should only appear at later timescales than the ones probed in this work and for this reason are not expected to be astrophysically relevant.

The decay timescale depends on the BH spin. Here only non-spinning BHs were considered, but geometric-optics approximation can be used to predict that rapidly spinning BHs will show a much larger relaxation timescale, and a breaking of degeneracy with respect to different angular directions [223, 245]. This raises the interesting property of determining the BH spin from the ratio of amplitudes of different redshifts, but requires significant further work.

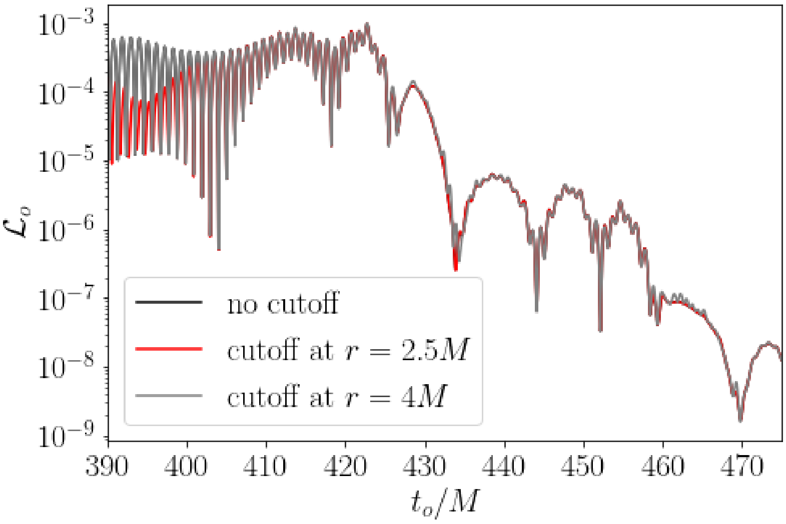

Figure 4.9: Luminosity in GWs from the system described in Section 4.2.4, for which the binary is shut off below a certain radius, signaling for example a sudden merger of the binary. In line with the findings for scalar waves in Fig. 4.8, near-horizon details are irrelevant for the appearance of these objects, and it is the LR that controls the late time signal.

Dying pulses from BH accretion were discussed in the context of Cygnus X-1, years ago [265, 266]. These works assume that light from such pulses mimics the motion of the source, which as we discussed is not correct. It is challenging to explain such observations through LR properties, since timescales seem to be off by almost an order of magnitude. Nevertheless, these observations show how LR relaxation could show up in observations with enough precision. This is relevant for BH imaging [15, 21, 262, 285], in particular for the next generation EHT [286, 287]. This collaboration plans to add 10 new observation points to the current EHT, which will increase the precision of current images and open the possibility of producing movies monitoring the evolution of matter being accreted by BHs, which could be compared with our general results for the luminosity decay.

Part II

TESTING THE GALACTIC CENTER WITH S2 MOTION

5

DATA AND NUMERICAL METHODS

Since their discovery, S-stars at the GC have played an important role in determining the parameters describing SgrA* and its environmental features. In this doctoral thesis we focus on the orbit of star S2, one of the closest to the GC and the one that has been monitored the longest. In this Chapter we present the set of available data and explain the numerical methods used in the fitting procedure. Indeed, for any model considered in this thesis, both the numerical integration of the equations of motion and the fitting method are performed in the same way, the only difference being the number of fitted parameters and their physical interpretation.

5.1 AVAILABLE DATA

The available data for star S2 can be divided in two different sets: the astrometric measurements in the plane of the sky, i.e., right ascension (RA) and declination (DEC), expressed in arcseconds, and the radial velocity (RV) measurements, that come from the analysis of the shift in the spectral lines of S2 and correspond to the total space velocity of the star in its reference frame $v = \sqrt{v_x^2 + v_y^2 + v_z^2}$, projected onto the line of sight. The latter is measured in km/s.

At the moment of writing the dataset D counts the following data points:

a) Astrometric data DEC, R.A.
   - 10 data points collected using the SHARP camera at the New Technology Telescope between 1992 and 2002 (accuracy $\approx 4\,\mathrm{mas}$);
   - 118 data points collected at the NACO imager at the VLT between 2002 and 2019 (accuracy $\approx 0.5\,\mathrm{mas}$);
   - 76 data points collected by GRAVITY at VLT Interferometer between 2016 and April 2022 (accuracy $\approx 50\,\mu\mathrm{as}$).

b) Spectroscopic data V_R
   - 2 data points collected by NIRC2 at Keck in 2000 and 2002;

  - 100 data points collected by SINFONI at the VLT between 2002 and March 2022 (accuracy in good conditions $\approx 10-15\,\mathrm{km/s}$).

5.2 NUMERICAL INTEGRATION

Most of S2 motion happens in a weak field regime, since the star orbits quite far from the central SMBH, its orbital range being between $\approx 1400\,r_S$ and $\approx 22500\,r_S$. For this reason, the initial conditions for the motion can be borrowed from the Keplerian two body problem solutions. Specifically, one can define the SMBH reference frame in which S2 motion happens via the usual spherical coordinates $\{r, \theta, \phi\}$, where the origin corresponds to the location of SgrA*. Following this convention, the six initial conditions necessary to solve the equations of motion are computed at the time of apoastron passage, i.e., the point of farthest approach, $t_{\mathrm{apo}} = t_0 = 2010.356$ and they read:

$$\begin{aligned}
r_0 &= \frac{a(1-e^2)}{1+e\cos\phi_0}\,, \\
\theta_0 &= \frac{\pi}{2}\,, \\
\phi_0 &= 2\arctan\left(\sqrt{\frac{1+e}{1-e}}\tan\frac{\mathcal{E}}{2}\right), \\
\dot{r}_0 &= \frac{2\pi e a\sin\mathcal{E}}{P(1-e\cos\mathcal{E})}\,, \\
\dot{\theta} &= 0\,, \\
\dot{\phi}_0 &= \frac{2\pi(1-e)}{P(e\cos\mathcal{E}-1)^2}\sqrt{\frac{1+e}{1-e}}\,,
\end{aligned} \tag{5.1}$$

where the dot represents the derivative with respect to time and e is the eccentricity of the orbit, a the semi-major axis, P the period and $\mathcal{E}$ the so-called eccentric anomaly. The latter can be obtained solving Kepler's equation:

$$\mathcal{E} - e\sin\mathcal{E} - \mathcal{M} = 0\,, \tag{5.2}$$

where $\mathcal{M}$ is the mean anomaly and it is defined as the angular distance at time t from the periastron passage t_p: $\mathcal{M} = n(t - t_p)$, with $n = 2\pi/P$ being the *mean angular motion* of the body. Kepler's equation can be only solved numerically and for the specific case at $t = t_0$ ($\mathcal{M} = \pi$) we solved it using a Python's root finder (**scipy.optimize.newton**) which implements a Newton-Raphson method. The latter solves Eq. (5.2) with precision of $\mathcal{O}(10^{-16})$.

Moreover, the observational dates are different from the actual emission dates of the signal due to the finite value of the speed of light. In order to keep this into consideration one needs to solve numerically the Rømer's equation:

$$t_{\mathrm{obs}} - t_{\mathrm{em}} - z_{\mathrm{obs}}(t_{\mathrm{em}}) = 0\,, \tag{5.3}$$

that can be approximated with its first order Taylor expansion around t_{em}:

$$t_{\mathrm{em}} = t_{\mathrm{obs}} - \frac{z_{\mathrm{obs}}(t_{\mathrm{obs}})}{1 + v_{z_{\mathrm{obs}}}(t_{\mathrm{obs}})} \,. \tag{5.4}$$

The difference between Eq. (5.3) and its approximation in Eq. (5.4) is at most $\sim 4\,\mathrm{s}$ along S2 orbit and therefore negligible. The Rømer effect affects both the astrometry and the spectroscopy, with an impact of $\approx 450\,\mu$as on positions and ≈ 50 km/s at periastron on RV. Our results recover the previous estimates for this effect computed in Refs. [219, 288].

Once the numerical integration is performed at the emission dates, the coordinates of the star are expressed in a Cartesian form, using the usual transformation:

$$\begin{cases} x_{\mathrm{BH}} = r\cos\phi\sin\theta \\ y_{\mathrm{BH}} = r\sin\phi\sin\theta \\ z_{\mathrm{BH}} = r\cos\theta \end{cases} \tag{5.5}$$

where the notation "BH" means that those coordinates are still evaluated in the BH reference frame. The transformation of coordinates from the orbital plane $\{x_{\mathrm{BH}}, y_{\mathrm{BH}}, z_{\mathrm{BH}}\}$ to the observer frame $\{x_{\mathrm{obs}}, y_{\mathrm{obs}}, z_{\mathrm{obs}}\}$ is carried out introducing the three Euler angles needed to perform a rotation of the reference frame, namely the longitude of ascending node Ω, the inclination i, the argument of periastron ω, and the so-called Thiele-Innes parameters [288, 289]:

$$\begin{aligned} A &= \cos\Omega\cos\omega - \sin\Omega\sin\omega\cos i \\ B &= \sin\Omega\cos\omega + \cos\Omega\sin\omega\cos i \\ F &= -\cos\Omega\sin\omega - \sin\Omega\cos\omega\cos i \\ G &= -\sin\Omega\sin\omega + \cos\Omega\cos\omega\cos i \\ C &= -\sin\omega\sin i \\ H &= -\cos\omega\sin i \,. \end{aligned} \tag{5.6}$$

The transformation then reads:

$$\begin{aligned} x_{\mathrm{obs}} &= Ax_{\mathrm{BH}} + Fy_{\mathrm{BH}} & v_{x_{\mathrm{obs}}} &= Av_{x_{\mathrm{BH}}} + Fv_{y_{\mathrm{BH}}} \\ y_{\mathrm{obs}} &= Bx_{\mathrm{BH}} + Gy_{\mathrm{BH}} & v_{y_{\mathrm{obs}}} &= Bv_{x_{\mathrm{BH}}} + Gv_{y_{\mathrm{BH}}} \\ z_{\mathrm{obs}} &= -(Cx_{\mathrm{BH}} + Hy_{\mathrm{BH}}) & v_{z_{\mathrm{obs}}} &= -(Cv_{x_{\mathrm{BH}}} + Hv_{y_{\mathrm{BH}}}) \,, \end{aligned} \tag{5.7}$$

where $v_{z_{\mathrm{obs}}} = V_R$, i.e., it corresponds to the measured RV of the star. With this convention, the z-axis is pointing from Earth toward the SMBH.

The final step in order to obtain the measured DEC and RA, is to convert the physical distances into angular distances. This can be achieved introducing the GC distance R_0 via:

$$\begin{aligned} \mathrm{DEC} &= \arctan\left(\frac{x_{\mathrm{obs}}}{R_0}\right) \approx \frac{x_{\mathrm{obs}}}{R_0}\,, \\ \mathrm{RA} &= \arctan\left(\frac{y_{\mathrm{obs}}}{R_0}\right) \approx \frac{y_{\mathrm{obs}}}{R_0}\,. \end{aligned} \tag{5.8}$$

5.2.1 *Relativistic corrections to the radial velocity*

As previously stated, the RV measurements are mostly performed using SINFONI, which is a NIR integral field spectrograph. Hence, in order to analyse correctly those data one needs to consider possible shifts in the spectral lines due to relativistic effects.

Specifically, in the region near the periastron, S2 reaches a total space velocity of $v \approx 10^{-2}$, which means that both the relativistic Doppler shift and the gravitational redshift affect the measurements in a significant way. Quantitatively, the combination of the two effects counts up to $\approx 200\,\mathrm{km/s}$ difference at periastron passage, while it remains lower than $\approx 10\,\mathrm{km/s}$ near apoastron, with respect to the same RV computed without relativistic effects.

The direct measurement of the gravitational redshift on S2 motion was the first proof that the orbit is inconsistent with a pure Newtonian model and it is instead well described by a Post Newtonian (PN) orbit [219]. The contribution due to the relativistic Doppler shift reads:

$$1 + z_D = \frac{1 + v_{z_{\mathrm{obs}}}}{\sqrt{1 - v^2}}\,, \tag{5.9}$$

while the gravitational redshift is given by

$$1 + z_G = \frac{1}{\sqrt{1 - 2M/r_{\mathrm{em}}}}\,, \tag{5.10}$$

where r_{em} means that the radial coordinate is evaluated at the time of emission. Following Grould et al. [288] the two shifts can be combined in a single expression for the RV as

$$V_R \approx \frac{1}{\sqrt{1-\epsilon}} \cdot \frac{1 + v_{z_{\mathrm{obs}}}/\sqrt{1-\epsilon}}{\sqrt{1 - v^2/(1-\epsilon)}} - 1\,, \tag{5.11}$$

where $\epsilon = 2M/r_{\mathrm{em}}$.

5.2.2 *The Schwarzschild precession*

In 2020, the GRAVITY collaboration published a paper announcing the detection of the SP for the first time, in correspondence of the periastron passage of S2 on May 19, 2018 (2018.38) [166].

The shift in the position angle of the star in the plane of sky $\delta\phi = \arctan(\mathrm{RA}/\mathrm{DEC})$ is parametrized using the Parametrized Post Newtonian (PPN) formalism developed in Ref. [290] and the variation per orbital period can be written as [1]:

$$\Delta\phi = f_{\mathrm{SP}} \frac{3\pi r_S}{a(1-e^2)} = f_{\mathrm{SP}} \times 12.1' \,, \tag{5.12}$$

where the parameter f_{SP} is introduced *ad hoc* and it is equal to 1 in GR and 0 in Newtonian theory. To include the SP in the equations of motion the collaboration used the formalism developed by Will [291], neglecting both the terms due to the quadrupole moment Q_2 and the spin J, in which the acceleration reads:

$$\mathbf{a}_{1\mathrm{PN}} = \frac{M_\bullet}{r^2}\left[\left(2(\gamma+\beta)\frac{M_\bullet}{r} - \gamma v^2\right)\frac{\mathbf{r}}{r} + 2(\gamma+1)\dot{r}\mathbf{v}\right] . \tag{5.13}$$

In terms of the new parameter f_{SP}, Eq. (5.13) becomes:

$$\mathbf{a}_{1\mathrm{PN}} = f_{\mathrm{SP}}\frac{M_\bullet}{r^2}\left[\left(\frac{4M_\bullet}{r} - v^2\right)\frac{\mathbf{r}}{r} + 4\dot{r}\mathbf{v}\right] . \tag{5.14}$$

There is no exact comparison between f_{SP} and the PPN parameters γ and β, since the parameter f_{SP} only quantifies how relativistic the orbit is. However, since the orbit of S2 is highly eccentric, the precession induces an almost instantaneous change in the pericenter angle ω. In the limit where one only compares the orbit pre and post pericenter passage, $3f_{\mathrm{SP}} = 2 + 2\gamma - \beta$.

In the SP paper, the GRAVITY collaboration measured $f_{\mathrm{SP}} = 1.11 \pm 0.21$. The latter measurement improved in Ref. [167] where multiple stars in the S-cluster (S29, S38 and S55) were included in the fit, finding

$$f_{\mathrm{SP}} = 0.99 \pm 0.15 \,, \tag{5.15}$$

and hence excluding a pure Newtonian motion at 7σ confidence level.

In this thesis the SP will be always included in the fit, adding the 1PN acceleration in Eq. (5.14) to the equations of motion and assuming $f_{\mathrm{SP}} = 1$, unless otherwise stated.

Before proceeding, it is important to address the issues that emerge when one considers the relativistic acceleration in Eq. (5.14) and performs the projection of the orbit via Eqs. (5.7), which instead is obtained working in a Euclidean space. Indeed, while the equations of motion in Euclidean space are valid whatever is the system of coordinates considered, the 1PN correction in Eq. (5.14) is derived assuming harmonic, or isotropic, coordinates. Hence, the expression for $\mathbf{a}_{1\mathrm{PN}}$ depends explicitly on the system of coordinates used and the Euclidean projection performed via Eq. (5.7) is in principle no longer valid, leading to an ambiguous determination of the orbit in a semi-Riemannian space [292].

How to treat astrometric measurements in relativistic settings is a long-standing problem [293–296] that the Collaboration is addressing at the time of writing. Preliminary results on the topic suggests that the error computed in performing an Euclidean projection while using the 1PN acceleration in Eq. (5.14) is of order of few tens of μas in the astrometry of S2 and overall negligible [297]. However, with the advent of GRAVITY+ and the consequent possible discovery of stars closer to SgrA*, these effects may become very significant and alter consistently the determination of the orbital parameters of stars [292]. Consequently, a common strategy must be adopted and a possible solution to this dilemma is to determine the angular separation of the star as a coordinate-independent quantity [297].

5.3 MONTE CARLO MARKOV CHAIN ANALYSIS

The fitting method employed to analyse S2 data relies on Markov Chain Monte Carlo (MCMC) sampling. The latter is not a fitting method *per se* but instead it is a *sampler*. This means that the sampling process does not provide with a best-fitting parameters vector $\boldsymbol{\Theta}$, but rather with a sample of parameters that reasonably describe the model considered.

In the context of Bayesian inference, the MCMC process requires the knowledge of the prior distributions of the parameters in order to calculate their posterior distributions $P(\boldsymbol{\Theta}|D)$. The aim of the MCMC is to maximize $P(\boldsymbol{\Theta}|D)$, i.e., it is to select the parameters that are more likely to describe the data. The posterior can be calculated via the well-known Bayes' theorem:

$$P(\boldsymbol{\Theta}|D) = \frac{P(D|\boldsymbol{\Theta})P(\boldsymbol{\Theta})}{P(D)}, \tag{5.16}$$

where

- $P(D|\boldsymbol{\Theta})$ is the **likelihood** function, i.e., the probability of the data given the model. In general, the latter produces a curve that aims to fit the data and, in the specific case considered here, it returns positions and RV that describe the trajectory of S2.

- $P(\boldsymbol{\Theta})$ is the **prior** distribution of the parameters $\boldsymbol{\Theta}$, i.e., the knowledge *a priori* on the parameter itself. Generally, Gaussian distributions are used as priors when the parameter is well constrained by independent experiments/observations, while flat (or uniform) priors are used where no prior knowledge is available and only an interval of possible values is known.

- $P(D)$ is the **evidence** or **marginalised likelihood**, i.e., the probability of the data. This is a single number that represents the likelihood of the observed data given a certain model. Once the model is chosen, it is independent of the set of parameters $\mathbf{\Theta}$, which are integrated out. This quantity is not included in the fit, since it is possible to sample $P(\mathbf{\Theta}|D)$ without computing it, unless the aim is to compare two different generative models (see Section 5.4).

The MCMC estimates (samples) the LHS of Eq. (5.16) numerically integrating the RHS for some given value of the parameters $\mathbf{\Theta}$.

A sampling $\mathbf{\Theta}_{t=1}^{T}$ from some Probability Density Function (PDF) $P(\mathbf{\Theta}|D)$ is a set of T values of $\mathbf{\Theta}_t$ that are drawn from the PDF. If T is huge, the histogram of the sampling will look like the original function $P(\mathbf{\Theta}|D)$.

Given $P(\mathbf{\Theta}|D)$, the conditioned expectation value for $\mathbf{\Theta}$ is

$$E[\mathbf{\Theta}|D] = \int \mathbf{\Theta} P(\mathbf{\Theta}|D) d\mathbf{\Theta} \,, \tag{5.17}$$

which correspond to the mean values of $\mathbf{\Theta}$. Since the integral on the RHS of Eq. (5.17) is generally impossible to compute analytically, it is replaced by

$$E[\mathbf{\Theta}|D] \approx \frac{1}{T} \sum_{t=1}^{T} \mathbf{\Theta}_t \,. \tag{5.18}$$

A good sampling is one for which, in the limit $T \to \infty$, the approximation in Eq. (5.18) becomes exact.

A family of MCMC methods with the *affine invariant* property was introduced in Ref. [298]. A sampler is affine invariant if the sampling is invariant under linear transformations of the parameters, i.e., the algorithm samples equally well a posterior that depends on $\mathbf{\Theta}$ and one that depends on $f(\mathbf{\Theta})$, for any linear function f. As a consequence, the algorithm proposed in Ref. [298] produces independent samples with a much shorter autocorrelation time with respect to standard MCMC algorithms, such as the Metropolis-Hastings, and it can easily run in parallel, making it faster. In this work, the affine invariant MCMC sampling has been performed by means of the Python package EMCEE, developed by Foreman-Mackey et al. [299].

The process of running a MCMC with EMCEE is the following:

1. Set a function that outputs a model given the set of input parameters $\mathbf{\Theta}$. The set of parameters will be specified in each chapter, according to the different models tested. However, in any fit there will be 13 parameters that will always be included, namely:

$$\mathbf{\Theta} = \{e, a, \Omega, i, \omega, t_p, M_\bullet, R_0, x_0, y_0, v_{x0}, v_{y0}, v_{z0}\} \,, \tag{5.19}$$

where e, a, Ω, i, ω and t_p characterize the orbit of S2, R_0 and $M_\bullet$ describe the central SMBH and $\{x_0, y_0, v_{x0}, v_{y0}, v_{z0}\}$ are offset parameters needed to make the origin of the observer reference frame coincide with the position of SgrA* for some specific datasets (NACO and SINFONI data). For completeness, the best-fit values of the parameters in Eq. (5.19) are reported in Tables 5.1-5.2 together with their prior distributions, which are assumed to be flat for all the physical parameters and Gaussian for the offsets [300]. Those values are obtained in the non perturbative case, i.e., when the system is described by the 1PN equations of motion.

2. Set an ensemble of K walkers, each one defined by a D-dimensional vector $\mathbf{\Theta}$ that contains a set of initial guesses for the parameters. Those vectors are generally obtained spreading the walkers around a single initial guess $\mathbf{\Theta}$, which we choose to be the set of parameters that minimize the χ^2. In this way a grid with dimension $K \times D$ is created.

3. Each walker explores the parameters space by moving toward a new value of $\mathbf{\Theta}$ and generating a model with that $\mathbf{\Theta}$. The newly generated model is then compared to the given data via the likelihood function. In this work a Gaussian likelihood is always implemented, defined as:

$$P(D|\mathbf{\Theta}) = \exp\left[-\frac{1}{2}\left(\frac{(\mathbf{x}_{\rm data}-\mathbf{x}_{\rm model})^2}{\Delta\mathbf{x}^2_{\rm data}} + \frac{(\mathbf{y}_{\rm data}-\mathbf{y}_{\rm model})^2}{\Delta\mathbf{y}^2_{\rm data}} + \frac{(\mathbf{v}_{\rm data}-\mathbf{v}_{\rm model})^2}{\Delta\mathbf{v}^2_{\rm data}}\right)\right], \tag{5.20}$$

where $\mathbf{x}_{\rm data} = $ DEC, $\mathbf{y}_{\rm data} = $ RA and $\mathbf{v}_{\rm data} = $ RV.

4. **The stretch move**. How each walker moves in the parameter space is dictated by the algorithm of Ref. [298]. Given an ensemble of K walkers $S = \{X_k\}$, the proposal move for one walker k depends on the positions (in the parameter space) of the $K-1$ walkers in the complementary ensemble $S_{[k]} = \{X_j, \forall j \neq k\}$. For each walker X_k a walker X_j is randomly extracted from $S_{[k]}$ and the new (proposed) position is:

$$X_k(t) \to Y = X_j + Z\left[X_k(t) - X_j\right], \tag{5.21}$$

where Z is a random variable extracted from the distribution $g(z = Z)$:

$$g(z) \propto \begin{cases} \frac{1}{\sqrt{z}} & \text{if } z \in \left[\frac{1}{a}, a\right] \\ 0 & \text{otherwise} \end{cases} \tag{5.22}$$

with $a = 2$. The proposed move will be accepted with probability given by

$$q = \min\left(1,\, Z^{D-1}\frac{P(Y|D)}{P(X_k(t)|D)}\right) . \tag{5.23}$$

This means that a random number n will be extracted in the interval $[0, 1]$ and if $n \leq q$ then the new position Y is accepted and the walker moves there, otherwise it is discarded, the walker remains in the same position and a new move is proposed to another walker.

Parameter	Best-fit value	Lower bound	Upper bound
e	0.88441 ± 0.00007	0.83	0.93
a[as]	0.12497 ± 0.00013	0.119	0.132
i_{orb} [°]	134.69 ± 0.03	100	150
ω_{orb} [°]	66.28 ± 0.03	40	90
Ω_{orb} [°]	228.19 ± 0.03	200	250
t_p[yr]	2018.37902 ± 0.00009	2018	2019
M [$10^6\, M_\odot$]	4.299 ± 0.013	4.1	4.8
R_0 [10^3 pc]	8.28 ± 0.01	8.1	8.9

Table 5.1: Best-fit values (with 1σ uncertainty) for the physical parameters involved in the fit, together with uniform priors used in the MCMC analysis.

Parameter	Best-fit value	ξ	σ
x_0 [mas]	-0.24 ± 0.07	-0.055	0.25
y_0 [mas]	-0.618 ± 0.095	-0.570	0.15
v_{x_0} [mas/yr]	0.059 ± 0.006	0.063	0.0066
v_{y_0} [mas/yr]	0.074 ± 0.009	0.032	0.019
v_{z_0} [km/s]	-2.46 ± 1.47	0	5

Table 5.2: Best fit values (with 1σ uncertainty) and Gaussian priors used in the MCMC analysis of the offset parameters. ξ and σ represent the mean and the standard deviation of the distributions, respectively, taken from [300].

Steps 3 and 4 will be repeated by all K walkers in the ensemble, N iterations each.

In our fits, $K = 64$ walkers and $N = 10^5$ iterations are used. Since the MCMC starts at the minimum of the χ^2 found by the Python package **optimize.minimize**, the initial 20% of moves were discarded for the burning-in phase while the last 80% of the chains is used to compute mean and standard deviation of the posterior distributions.

Since the samples in the MCMC are not independent from each other, one can define the autocorrelation time τ_f as the number of steps needed in order to have independent chains. Foreman-Mackey et al. [299] defined the autocorrelation time as:

$$\tau_f(M) = 1 + 2\sum_{\tau=1}^{M} \rho_f(\tau)\,, \tag{5.24}$$

for some $M \ll N$, with ρ_f representing the normalized autocorrelation function of the stochastic process that generates the chains. Using a finite chain $\mathbf{\Theta}_{n=1}^{N}$, the latter can be estimated as follows:

$$\rho_f(\tau) = \frac{\hat{c}_f(\tau)}{\hat{c}_f(0)}\,, \tag{5.25}$$

where

$$\hat{c}_f(\tau) = \frac{1}{N-\tau}\sum_{n=1}^{N-\tau}(\mathbf{\Theta}_n - \mu_f)(\mathbf{\Theta}_{\tau+n} - \mu_f) \tag{5.26}$$

and

$$\mu_f = \frac{1}{N}\sum_{n=1}^{N}\mathbf{\Theta}_n\,. \tag{5.27}$$

In EMCEE it is generally sufficient to run N iterations such that $N \gg 50\,\tau_f$ in order to assure the convergence of the chains.

The numerical framework described above and used in this thesis has been tested and compared with other codes independently developed by the GRAVITY collaboration members.

5.4 MODEL SELECTION

When a new theory describing a certain system is proposed, it is necessary to understand *if* and *how much* the new model better fits the data if compared to the old one. In the specific cases considered in this thesis, the idea is to compare the BH model in vacuum described by 1PN equations of motion (that we call model M_0), which results in having the S2 orbit described by the parameters in Table 5.1, with the perturbative models described in Sec. 6.2-6.3 (that we call model M_1).

This can be achieved by considering the theories as Bayesian models and compare their predictive power via the so-called Bayes factor [301, 302]. The latter is defined as

$$K = \frac{P(D|M_1)}{P(D|M_0)}\,, \tag{5.28}$$

i.e., it corresponds to the ratio of the evidences of the two models being compared. Hence, in order to determine the Bayes factor, the evidence must be computed. This is defined as

$$P(D|M_m) = \int P(D|\mathbf{\Theta}_m, M_m) P(\mathbf{\Theta}_m|M_m) d\mathbf{\Theta}_m \qquad m = 0, 1\,, \tag{5.29}$$

where $\mathbf{\Theta}_m$ is the vector of parameters in model m and $P(\mathbf{\Theta}_m|M_m)$ is its prior density. Getting an estimate of the integral in Eq. (5.29) is generally far from being easy and some analytical approximations have been proposed [302].

In our case, EMCEE does not allow to compute the evidences automatically and hence in order to perform the integral we made use of the Python library **MCEvidence** developed by Heavens et al. [303]. The code takes as an input the posterior distributions and the likelihoods generated by EMCEE and returns the logarithm of the marginalised likelihood using the kth nearest neighbour distances algorithm.

As a consequence, one can evaluate the logarithm of the Bayes factor as

$$\log_{10} K = \log_{10}(P(D|M_1)) - \log_{10}(P(D|M_0)) \tag{5.30}$$

and compare the result with the table in Ref. [301] in order to check whether or not the new model is preferred by observations.

6

BOSONIC CLOUDS AT THE GALACTIC CENTER

6.1 BLACK HOLE SUPERRADIANCE

The term *superradiance* was firstly coined by Dicke in 1954 in the context of coherent emission of quantum optics [304] and lately extended to BH physics by Press and Teukolsky [305, 306]. The authors showed that when a spinning BH is immersed in a radiation field, it can both absorb waves or amplify them, depending on the angular mode and the frequency of the wave.

In a pioneering work, Teukolsky showed that linear perturbations on the Kerr geometry described by the line element in Eq. (1.1), could be described by a single master equation that only depends on the spin s of the field, using the Newman-Penrose formalism [307]. In Boyer-Lindquist coordinates, Teukolsky's equation reads:

$$\begin{aligned}
&\left[\frac{(r^2+j^2)^2}{\Delta} - j^2\sin^2\theta\right]\partial_t^2\Psi - \Delta^{-2}\partial_r\left(\Delta^{s+1}\partial_r\Psi\right)\\
&\frac{4jMr}{\Delta}\partial_t\partial_\phi\Psi + 2s\left[r + \frac{M(j^2-r^2)}{\Delta} + ij\cos\theta\right]\partial_t\Psi\\
&-\frac{1}{\sin\theta}\partial_\theta(\sin\theta\Psi) - 2s\left[\frac{j(r-M)}{\Delta} + \frac{i\cos\theta}{\sin^2\theta}\right]\partial_\phi\Psi\\
&-\left[\frac{1}{\sin^2\theta} - \frac{j^2}{\Delta}\right]\partial_\phi^2\Psi + \left(s^2\cot^2\theta - s\right)\Psi = 4\pi\Sigma T\,,
\end{aligned} \tag{6.1}$$

where T is the source term and corresponds to the trace of the energy-momentum tensor.

In vacuum, i.e., $T = 0$, because of the axi-symmetry of the Kerr metric, one can use the following ansatz for the field Ψ

$$\Psi(t,r,\theta,\phi) = \frac{1}{2\pi}\int d\omega e^{-i\omega t} e^{im\phi} S(\theta) R(r) \tag{6.2}$$

and the master equation in (6.1) becomes separable in a radial and angular part. These read

$$\Delta^{-s}\frac{d}{dr}\left(\Delta^{s+1}\frac{dR}{dr}\right) + \left(\frac{K^2 - 2is(r-M)K}{\Delta} + 4is\omega r - \lambda\right)R = 0 \tag{6.3}$$

and

$$\begin{aligned}&\frac{1}{\sin\theta}\frac{d}{d\theta}\left(\sin\theta\frac{dS}{d\theta}\right)+\left(j^2\omega^2\cos^2\theta-\frac{m}{\sin^2\theta}-2j\omega s\cos\theta\right.\\&\left.-\frac{2ms\cos\theta}{\sin^2\theta}-s^2\cot^2\theta+s+A_{s\ell m}\right)S=0\,,\end{aligned} \tag{6.4}$$

where $K \equiv (r^2+j^2)\omega - jm$ and $\lambda \equiv A_{s\ell m} + j^2\omega^2 - 2jm\omega$.

The solutions to the angular equation (6.4) are known as spin-weighted spherical harmonics $e^{i\omega\phi}S \equiv S_{s\ell m}(j\omega, \theta, \phi)$, which reduce to the spin-weighted spherical harmonics $Y_{s\ell m}(\theta, \phi)$ when $j\omega = 0$, and for spin 0 fields are given by the expressions in Eq. (3.2) [308].

Introducing the tortoise coordinate r_* as $dr/dr_* = \Delta/(r^2+j^2)$, the radial equation in (6.3) has asymptotic solutions given by

$$\begin{aligned}R_{s\ell m} &\sim \mathcal{T}\Delta^{-s}e^{-ik_H r_*}+\mathcal{O}e^{ik_H r_*} && \text{for} \quad r\to r_+\,,\\ R_{s\ell m} &\sim \mathcal{I}\frac{e^{-i\omega r}}{r}+\mathcal{R}\frac{e^{i\omega r}}{r^{2s+1}} && \text{for} \quad r\to\infty\,,\end{aligned} \tag{6.5}$$

where $k_H = \omega - m\Omega_H$ and $\Omega_H = j/(2Mr_+)$ is the angular velocity of the BH horizon $r_+ = M + \sqrt{M^2 - j^2}$.

These boundary conditions correspond to an incident wave with amplitude $\mathcal{I}$ from spatial infinity which is reflected back with amplitude $\mathcal{R}$ and transmitted at the horizon with amplitude $\mathcal{T}$. For BHs the presence of a one-way membrane at the horizon $r = r_+$ implies $\mathcal{O} \equiv 0$, meaning that there is no outgoing flux across the horizon.

Since the background is stationary, the field equations are invariant under the transformation $t \to -t$ and $\phi \to -\phi$. Hence, there exist a linearly independent solution $\bar{\Psi}$ that satisfies the complex conjugate boundary conditions. This implies that their Wronskian is constant and thus independent from the radial coordinate r_*, since both solutions satisfy Eq. (6.3). Thus, the Wronskian evaluated at the horizon must be equal to the Wroskian evaluated at infinity. This condition implies (for the specific case considered with $\mathcal{O} = 0$) that

$$|\mathcal{R}|^2 = |\mathcal{I}|^2 - \frac{k_H}{\omega}|\mathcal{T}|^2\,. \tag{6.6}$$

From Eq. (6.6) one can see that $|\mathcal{R}|^2 < |\mathcal{I}|^2$ when $k_H > 0$, as it is expected from absorbers. However, when $k_H < 0$, then $|\mathcal{R}|^2 > |\mathcal{I}|^2$, meaning that the reflected wave is amplified with respect to the incident wave. The condition $k_H < 0$ is equivalent to

$$\omega - m\Omega_H < 0\,, \tag{6.7}$$

which is exactly the superradiance condition. It is interesting to note that this result is valid whatever is the spin of the field considered and hence can be applied to scalar ($s = 0$), vector ($s = \pm 1$) and tensor ($s = \pm 2$) fields, indistinctly.

It can be shown that BHs satisfying the superradiant condition in Eq. (6.7) and confined within a closed system trigger instabilities due to the exponentially increasing pressure of the field on the boundary, and this process takes the name of *black hole bomb* [305]. In a realistic scenario, massive fields provide a natural confinement of low frequency radiation because of the Yukawa-like suppression $\sim e^{-\mu r}/r$, being μ the mass of the field.

6.1.1 *Black holes as particle detectors*

As mentioned in Chapter 1, ultralight bosons are among the possible candidates for DM and have gained a lot of attention due to their connection with particle physics. An example of such a light boson is the Peccei-Quinn axion, which was firstly introduced to solve the strong CP problem in quantum cromodynamics [48]. The mechanism proposed by Peccei and Quinn is based on a spontaneous symmetry breaking associated to a new particle, the axion, similarly to the Higgs mechanism. Axions also arises naturally in string theory, which is currently the most developed theory for quantum gravity [49].

As we have seen, the frequencies ω that appears in the ansatz (6.2) are generally complex numbers, due to the boundary conditions imposed at the event horizon and at infinity. The superradiant instability is triggered when the eigenfrequency has $\omega_I > 0$, which always happens if the real part of the frequency satisfies the superradiant condition in Eq. (6.7), i.e., $\omega_R < m\Omega_H$.

When this condition is fulfilled, the field grows exponentially in time, with a timescale dictated by $\tau_I = 1/\omega_I$. In general, the instability timescale depends on the coupling of the two fields $\alpha = \mu M$, on the spin of the BH j and on the mode numbers (ℓ, m, n). The fastest growing mode is the fundamental one ($n = 0$), which is characterised by different quantum numbers depending on the spin of the field, and its growth goes faster the more the BH is spinning. The dimensionless coupling α can be written as (reintroducing fundamental constants for clarity)

$$\alpha = \left[\frac{GM}{c^2}\right]\left[\frac{m_{s,v}\,c}{\hbar}\right] = 0.752\left(\frac{M}{10^6 M_\odot}\right)\left(\frac{m_{s,v}}{10^{-16}\,\mathrm{eV}/\mathrm{c}^2}\right), \qquad (6.8)$$

where $m_{s,v}$ represents the mass of the scalar or vector field.

During the instability growth, the field extracts mass and angular momentum from the BH, until they saturate to specific values. Indeed, due to the loss of spin by the BH, the angular frequency Ω_H decreases, until it reaches the value $\Omega_H(M_f, J_f) = \omega_R/m$, where M_f and J_f are the BH mass and angular momentum at the end of the instability phase. At this point, the field is entirely described by a single mode with real frequency $\omega_R \sim \Omega_H$ and the growth stops [309–312]. The final BH spin J_f can be estimated in the small coupling limit ($\alpha \ll 1$) as

$$J_f \approx \frac{4mM_f^3\mu}{m^2 + 4M_f^2\mu^2}, \tag{6.9}$$

and assuming no other processes happen during the instability phase, the mass of the cloud at the end of the superradiant process is given by

$$M^f_{\rm cloud} = M_i - M_f = -\delta M = -\frac{\omega_R}{m}\delta J \tag{6.10}$$

where M_i is the initial BH mass and δJ is the variation of the BH angular momentum, which is negative if superradiance occurs ($\delta J < 0$ therefore implies $M^f_{\rm cloud} > 0$) [313].

Hence, the superradiant instability leads to the formation of a boson cloud around the BH that can extract up to 10% of the initial BH's mass [311, 314]. In the specific case of Proca fields, it has been shown that the final stage of superradiant growth corresponds to a stationary "hairy" BH solutions found in Ref. [315], where the authors constructed a solution corresponding to a rotating BH surrounded by a complex Proca field that oscillates with frequency $\omega = m\Omega_H$, but still generates a stationary stress-energy tensor (and hence circumventing the no-hair theorem).

When the BH spin reaches the value in Eq. (6.9), the boson cloud starts to slowly decay due to the emission of GWs on a timescale $\tau_{GW} = M^f_{\rm cloud}/\dot{E}_{GW}(t=0)$, where $t = 0$ is defined as the moment in which the cloud has mass $M^f_{\rm cloud}$. The exact GW flux can be computed solving Teukolsky equation numerically, but in the small coupling limit can be approximated as

$$\dot{E}_{GW} \approx A_{\ell ms}\left(\frac{M_{\rm cloud}}{M}\right)^2 \alpha^{4\ell+4s+10}, \tag{6.11}$$

where the constant $A_{\ell ms}$ depends on the spin of the field.

The possibility that boson clouds can grow around BHs open a new way to detect and constrain new fundamental fields in the Universe, with particular attention to those candidates that have escaped detection in Earth-based accelerators.

In the following sections we consider the hypothesis that a boson (scalar and vector) cloud clustered around SgrA* by means of superradiance or other processes. It is a tantalizing possibility that SMBHs might then be used as particle detectors, a possibility that we explore, using the motion of S2 as a probe of the matter content to constrain the mass of such a cloud at the GC. These fields might be a significant component of DM, or simply as-yet unobserved forms of matter.

The suggestion that the stars' motion can be used to probe light fields around BHs is not new [316–318], but here it is explored explicitly with the inclusion of data from the GRAVITY instrument.

6.2 CONSTRAINING SCALAR CLOUDS USING S2 MOTION

Thus far, the profile of the matter distribution at the GC has been mostly ad-hoc, clear examples being the Plummer profile in Ref. [167] or the spike density distribution in Ref. [171]. Here, the possibility that new fundamental fields exist and "condense" in a bound state around the BH is explored. It can be argued that also in the context of fuzzy DM, composed of an ultralight scalar, the near-horizon region is controlled by BH physics, hence governed by the same type of profile considered in this work [319].

6.2.1 *The setup*

Consider a particle moving in a potential given by a central mass $M_\bullet$ surrounded by a scalar field cloud. Our starting point is the setup developed in Ref. [320]. For clarity, we will reintroduce fundamental constants in the following.

A system composed of a central BH with mass $M_\bullet$ and a scalar field minimally coupled to the gravity sector is described by the action

$$S = \int d^4x\sqrt{-g}\left(\frac{R}{16\pi G} - \frac{1}{2}g^{\alpha\beta}\psi^*_{,a}\psi^*_{,b} - \frac{\mu^2}{2}\psi\psi^*\right)\,, \tag{6.12}$$

where R is the Ricci scalar, $g_{\mu\nu}$ and g are the metric and its determinant. As already mentioned, we assume that the BH spins along the $z-$axis, with adapted spherical coordinates (t, r, θ, ϕ), and $\theta = \pi/2$ defining the equator. The scalar field $\psi(t, r, \theta, \phi)$ is a complex field, and μ is a mass parameter related to the physical mass m_s via $\mu = m_s c/\hbar$ and to the (reduced) Compton wavelength of the particle via $\lambda_C = \mu^{-1}$.

The principle of least action results in the Einstein-Klein-Gordon system of equations, which in general must be solved numerically to obtain the dynamics of a test particle in such a setup. However, since the final aim is to fit S2 orbit, which happens to be in weak field region of space, there is no need to proceed in this way and perform expensive numerical computations.

Instead, one can compute the energy-momentum tensor of the scalar field as

$$T_{\mu\nu} = \frac{1}{2}\left[\psi_{,\mu}\psi^*_{,\nu} + \psi_{,\nu}\psi^*_{,\mu} - g_{\mu\nu}\left(\psi^{,\sigma}\psi^*_{,\sigma} + \mu^2|\psi|^2\right)\right] \tag{6.13}$$

and obtain the energy density taking the T_{00} component of (6.13) in the low-energy limit, i.e., neglecting terms of $\mathcal{O}(c^{-4})$. In this approximation, the energy density of the field reads

$$\rho = \frac{m_s^2c^2}{\hbar^2}|\psi|^2 = \mu^2|\psi|^2 = \left(\frac{\alpha}{M_\bullet}\right)^2|\psi|^2\,, \tag{6.14}$$

where the dimensionless mass coupling α was introduced in Eq. (6.8).

From now on, we will continue using geometric units.

In the limit of small coupling ($\alpha \ll 1$) and assuming the same ansatz for the field of Eq. (6.2), the radial part $R(r)$ is proportional to the generalised Laguerre polynomials L_n^{2l+1}, while the angular part reduces to $S_{\ell m}(\theta) = P_\ell^m(\cos\theta)$, where $P_\ell^m(\cos\theta)$ are the associated Legendre polynomials. In this approximation, the fundamental mode $n = 0$, $\ell = m = 1$ of the scalar field is given by [321]

$$\psi = A_0 e^{-i(\omega t - \phi)} \frac{r}{M_\bullet} \alpha^2 e^{-\frac{r\alpha^2}{2M_\bullet}} \sin\theta \,. \tag{6.15}$$

As already mentioned, generally the frequencies ω of the field in equation (6.15) are complex numbers, characterised by a real and an imaginary part. The imaginary part quantifies the exponential growth of the scalar profile, while the real part is associated with the oscillations frequency of the field. However, the former has an associated timescale given by $\tau_I = 1/\omega_I \sim M_\bullet \alpha^{-9}$, while the latter has $\tau_R = 1/\omega_R \sim M_\bullet \alpha^{-1}$. This results to have $\tau_R \ll \tau_I$ and consequently one can neglect the exponential growth phase and focus only on the dynamics of the scalar field oscillations (i.e., assuming $\omega = \omega_R$), as already done in Refs. [317, 320, 321].

The amplitude of the field A_0 can be related to the mass of the cloud via

$$M_{\text{cloud}} = \int \rho s^2 \sin\theta d\theta ds d\phi = \frac{64\pi A_0^2}{\alpha^4} M_\bullet \,, \tag{6.16}$$

and the density takes the form:

$$\rho = \frac{\Lambda}{64\pi M_\bullet^4} r^2 \alpha^{10} e^{-r\alpha^2/M_\bullet} \,. \tag{6.17}$$

Being S2 in the weak field regime, the energy density of the field in Eq. (6.17) can be used as source term in Poisson's equation $\nabla^2 U_{\text{sca}} = 4\pi\rho$. The latter can be solved using the spherical harmonic decomposition implemented in Poisson and Will [236], i.e., expanding all quantities in spherical harmonics $Y_{\ell m} = Y_{\ell m}(\theta, \phi)$.

For the energy density computed in Eq. (6.17) the only non-zero terms that contribute to the scalar potential U_{sca} are the $\ell = m = 0$ and $\ell = 2$, $m = 0$ terms, resulting in a potential given by

$$\begin{aligned} U_{\text{sca}} &= 4\pi \left[\frac{q_{00}}{r} Y_{00} + p_{00} Y_{00}\right] + \frac{4\pi}{5}\left[\frac{q_{20}}{r^3} Y_{20} + p_{20} r^2 Y_{20}\right] \\ &= \Lambda\left(P_1(r) + P_2(r)\cos^2\theta\right) \,, \end{aligned} \tag{6.18}$$

where $\Lambda = M_{\text{cloud}}/M_\bullet$ is the fractional mass of the scalar field cloud to the BH mass,

$$\begin{aligned} P_1(r) = \frac{M_\bullet}{r} + \frac{3M_\bullet^3}{r^3\alpha^4} - \frac{e^{-\frac{r\alpha^2}{M_\bullet}}}{16M_\bullet^2 r^3 \alpha^4}\Big(&48M_\bullet^5 + 48M_\bullet^4 r\alpha^2 + 40M_\bullet^3 r^2\alpha^4 \\ &+20M_\bullet^2 r^3\alpha^6 + 6M_\bullet r^4\alpha^8 + r^5\alpha^{10}\Big) \,, \end{aligned}$$

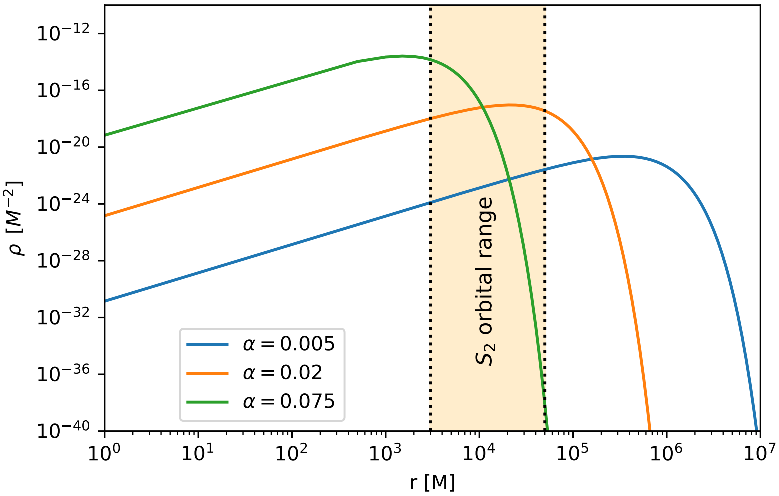

Figure 6.1: Energy density of Eq. (6.17) for different values of the coupling α. Only for some specific values of α the peak of the density distribution intersects S2 orbital range, represented by the orange vertical band. Here $\Lambda = 10^{-3}$.

(6.19)

and

$$P_2(r) = -\frac{9M_\bullet^3}{r^3\alpha^4} + e^{-\frac{r\alpha^2}{M_\bullet}}\left(\frac{9M_\bullet}{2r} + \frac{9M_\bullet^3}{r^3\alpha^4} + \frac{9M_\bullet^2}{r^2\alpha^2} + \frac{3\alpha^2}{2} + \frac{3r\alpha^4}{8M_\bullet} + \frac{r^2\alpha^6}{16M_\bullet^2}\right). \tag{6.20}$$

The energy density in Eq. (6.17) is plotted in Fig. 6.1 for different values of the mass coupling α and $\Lambda = 10^{-3}$, together with S2's orbital range represented by the orange vertical band.

In Ref. [320] the authors showed that a scalar field cloud described by the potential in Eq. (6.18) can leave imprints in the orbital elements of S2 if its mass coupling constant is in the range

$$0.005 \lesssim \alpha \lesssim 0.05\,, \tag{6.21}$$

which corresponds to a mass of the field in the range $10^{-20}\,\text{eV} \lesssim m_s \lesssim 10^{-18}\,\text{eV}$, if one assumes a fixed direction of the BH spin axis with respect to the plane of the sky. This result is related with the behaviour of the density displayed in Fig. 6.1, which indeed shows a maximum that only intersects S2 orbital range for some specific values of α, namely the range reported in (6.21).

However, Kodama and Yoshino [322] showed that for a SMBH with the mass of SgrA*, the allowed range of effective masses that can engage a superradiant instability on a timescale shorter than the cosmic age is $10^{-18}\,\text{eV} \lesssim m_s \lesssim 10^{-15}\,\text{eV}$, correspondent to $0.01 \lesssim \alpha \lesssim 10$. Hence, if a scalar cloud exists and leaves detectable imprints in the orbit of

S2, then its formation and existence must be explained by means of a different physical process.

One possibility is that the scalar soliton existed on its own, for example, if it is part of DM, in which case the placing of a BH at its centre will lead to a long-lived structure (a "cloud") which on BH scales resembles the superradiant bound states [319, 323]. In this work we will be agnostic regarding the origin of the scalar structure, but we will use our knowledge about the spatial profile of bound states around BHs.

Whatever is the origin of the scalar cloud, since the variations in the orbital elements of S2 induced by the cloud are potentially detectable with the current precision of the GRAVITY instrument, it is worth comparing these theoretical expectations with the available data. In particular we are interested in fitting the fractional mass of the cloud $\Lambda = M_{\rm cloud}/M_\bullet$ for fixed values of the mass coupling constant α.

6.2.2 *The equations of motion*

To obtain the equations of motion of a particle moving in a central potential plus the toroidal scalar field distribution described by the profile in Eq. (6.15), the starting point is the Lagrangian

$$\mathfrak{L} = \frac{1}{2}\left(\dot{r}^2 + r^2\dot{\theta}^2 + r^2\sin^2\theta\dot{\phi}^2\right) + U(r,\theta)\,, \tag{6.22}$$

where

$$U(r,\theta) = \frac{M_\bullet}{r} + \Lambda\left(P_1(r) + P_2(r)\cos^2\theta\right)\,, \tag{6.23}$$

is the sum of the Newtonian potential generated by the SMBH and the perturbation induced by the scalar cloud. Solving Euler-Lagrange equations translates into having the following equations of motion,

$$\begin{aligned}
\ddot{r} &= -\frac{M_\bullet}{r^2} + r\left(\dot{\theta}^2 + \sin^2\theta\dot{\phi}^2\right) + \Lambda\left(P_1'(r) + P_2'(r)\cos^2\theta\right)\,,\\
\ddot{\theta} &= \cos\theta\sin\theta\dot{\phi}^2 - \frac{2}{r}\dot{r}\dot{\theta} - \frac{\Lambda P_2(r)\sin 2\theta}{r^2}\,,\\
\ddot{\phi} &= -\frac{2\dot{\phi}}{r}\left(\dot{r} + \cot\theta\, r\dot{\theta}\right)\,,
\end{aligned} \tag{6.24}$$

where the dot represents a derivative with respect to time.

At those equations of motion one should add the 1PN contribution reported in Eq. (5.14). We followed the procedure described in Chapter 5 to obtain the astrometry, DEC and RA, and the RV of S2 in this framework.

6.2.3 *Constraints on the scalar cloud's mass*

We fit the datasets reported in Sec. 5.1 with the scalar cloud model, adding the fractional mass Λ to the list of parameters in (5.19).

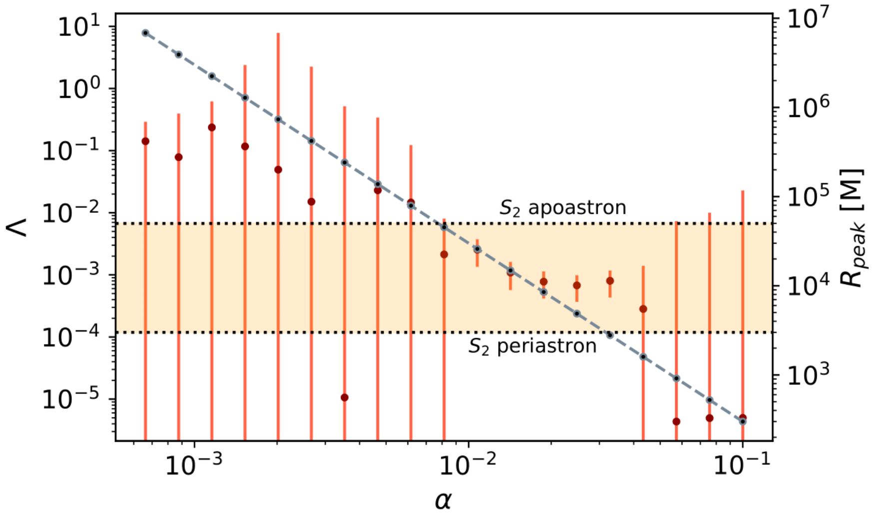

Figure 6.2: Best fit values of Λ with 1σ uncertainty when α is fixed and it is varied over the range $[0.0006, 0.1]$. The dashed grey line represents R_{peak} as a function of α as illustrated in (6.25). The yellow band represents the orbital range of S2 delimited by its apoastron and periastron positions. Although a nonzero value of Λ is apparent for a restricted range of α, the statistical significance of this finding is not significant, see Table 6.1.

Before running the MCMC algorithm following the procedure in Sec. 5.3, we used the Python library **optimize.minimize** to minimise the χ^2 and evaluate the best-fit values of Λ and how accurately one can constrain the scalar cloud mass. Results are summarised in Fig. 6.2. For very small ($\alpha \lesssim 0.0035$) or large ($\alpha \gtrsim 0.045$) values of α, Λ has very large uncertainties, and the results are all compatible with $\Lambda = 0$, i.e., having a vacuum environment.

Uncertainties on Λ become much smaller in the range $0.01 \lesssim \alpha \lesssim 0.04$, that roughly corresponds to the range in (6.21), predicted by Ref. [320]. The underlying reason can be understood computing the effective peak position of the scalar density distribution,

$$R_{\text{peak}} = \frac{\int_0^\infty \rho \bar{r} d\bar{r}}{\int_0^\infty \rho d\bar{r}} = \frac{3M_\bullet}{\alpha^2} \,. \tag{6.25}$$

For the range of α above, one finds

$$3000 M_\bullet \lesssim R_{\text{peak}} \lesssim 30000\, M_\bullet \,, \tag{6.26}$$

which means that the peak R_{peak} is located between S2's apoastron and periastron and hence the star is crossing regions of higher scalar density. This is also shown in Fig. 6.2, where the behaviour of R_{peak} as dictated by Eq. (6.25) is represented by a dashed grey line, and compared with S2's apoastron and periastron.

Notice that Fig. 6.2 seems to indicate that the motion of S2 is compatible with a cloud of scalar field for $0.01 < \alpha < 0.03$. However, as we now discuss, the statistical evidence for a nonzero Λ is not significant.

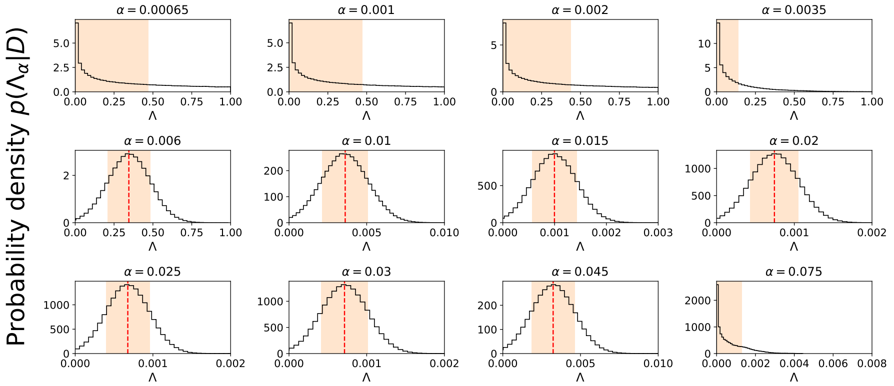

Figure 6.3: Posterior probability densities $P(\Lambda_\alpha|D)$ for different values of α. Red dashed lines represent the mean value of Gaussian distributions (which coincides with the MLE $\hat{\Lambda}$), while orange bands correspond to 1σ confidence level, i.e. $\approx 68\%$ of $P(\Lambda_\alpha|D)$ lies in that region.

MCMC results confirm the trend observed in Fig. 6.2 but provide more insights into how Λ is distributed when one fixes the value of α and hence the cloud's position. In particular, once the posterior distributions $P(\boldsymbol{\Theta}|D)$ are obtained from the MCMC, one can look for the Maximum Likelihood Estimator (MLE) of Λ, i.e., $\hat{\Lambda} = \arg\max \mathcal{L}(\Lambda; \mathrm{D})$. Because of the flat priors implemented and the use of the Gaussian likelihood in Eq. (5.20), looking for the MLE of Λ corresponds to find the value that maximises the posterior distribution $P(\Lambda_\alpha|D)$.

Results of the MCMC analysis are shown in Figure 6.3, which represents the one-dimensional projection of the (marginalised) posterior distributions of Λ for any value of α reported in Table 6.1.

Correlations between S2's parameters in the fit are shown by means of corner plots in Appendix D.1, for two illustrative cases $\alpha = 0.01$ and $\alpha = 0.001$.

One can firstly focus on the range $0.006 \leq \alpha \leq 0.045$, where the posteriors $P(\Lambda_\alpha|D)$ are normal distributions. Here the MLE $\hat{\Lambda}$ and associated uncertainties coincide with mean and standard deviation of the distributions, and they are roughly the same reported in Fig. 6.2. In Fig. 6.3 the mean and the 1σ confidence interval are represented by a red dashed line and an orange band, respectively.

As soon as one moves away from this range of α, the posteriors start to be peaked around zero and $\hat{\Lambda}$ does not coincide with the mean value of the distribution anymore, as a result of the prior bounds imposed on Λ. Since in these cases $\hat{\Lambda}$ is always very close to zero, and hence induces changes in the orbit far below what can be currently measured with data, we estimated Λ_1 and Λ_2 such that $P(\Lambda_\alpha < \Lambda_1|D) \approx 68\%$ and $P(\Lambda_\alpha < \Lambda_2|D) \approx 99\%$ of the posterior $P(\Lambda_\alpha|D)$. In this way one is able to obtain a rough upper bound on the fractional mass at 1 and 3σ confidence levels, respectively, and those values are reported in

α	$\hat{\Lambda}$	$\log_{10} K$
0.00065	$\lesssim (0.470\,,0.980)$	0.09
0.001	$\lesssim (0.470\,,0.980)$	0.08
0.002	$\lesssim (0.440\,,0.978)$	-0.06
0.0035	$\lesssim (0.140\,,0.780)$	-10.58
0.006	0.34671 ± 0.13666	1.44
0.01	0.00361 ± 0.00147	1.29
0.015	0.00101 ± 0.00042	1.24
0.02	0.00075 ± 0.00030	1.33
0.025	0.00068 ± 0.00028	1.35
0.03	0.00073 ± 0.00029	1.33
0.045	0.00328 ± 0.00135	1.27
0.075	$\lesssim (0.0013\,,0.0052)$	0.0001

Table 6.1: MLE $\hat{\Lambda}$ with associated 1σ error and Bayes factors $\log_{10} K$ for different values of α. The measurements for each α are not independent (the same orbit was used to derive them) and therefore cannot be combined to derive a more stringent upper limit. For non-normal distributions we report Λ_1 and Λ_2 defined such that $P(\Lambda_\alpha < \Lambda_1|D) \approx 68\%$ and $P(\Lambda_\alpha < \Lambda_2|D) \approx 99\%$ of $P(\Lambda_\alpha|D)$.

parenthesis in Table 6.1. In Fig. 6.3 the 1σ confidence interval evaluated as explained above is again represented by an orange band.

To be more specific, for $\alpha \leq 0.0035$, the posterior $P(\Lambda_\alpha|D)$ starts to flatten out, showing the difficulties of finding a meaningful MLE $\hat{\Lambda}$, and basically no relevant information can be extracted from those confidence intervals when $R_{\rm peak}$ is far from S2's apoastron (cfr. Table 6.2).

On the other hand, when $\alpha = 0.075$, which corresponds to $R_{\rm peak} \approx 530\, M_\bullet$, i.e., a cloud which is entirely confined within S2's periastron, we found that $\Lambda \lesssim 5 \cdot 10^{-3}$ at 3σ confidence level, roughly recovering the upper bound $\delta M \lesssim 10^{-3}\, M_\bullet$ found in Ref. [167].

As mentioned at the beginning of this discussion, when the posteriors are normal the MLE is roughly $\hat{\Lambda} \sim 10^{-3}$, and hence the motion is compatible with a cloud having mass $M_{\rm cloud} \sim 0.1\% M_\bullet$. In order to determine the statistical significance of these results we computed the logarithm of the Bayes factor K as described in Sec. 5.4.

According to Kass and Raftery [301] if $1 \leq \log_{10} K \leq 2$ there is a strong evidence that model M_1 is preferred over model M_0, while if $\log_{10} K > 2$ the strength of evidence is decisive. Negative values of $\log_{10} K$ correspond to negative evidence, i.e., M_0 is preferred over M_1.

As expected, $\log_{10} K \ll 1$ every time the cloud is located far away from S2 orbital range. In contrast, when $r_{\rm apo,S2} \lesssim R_{\rm peak} \lesssim r_{\rm peri,S2}$ there is only mild evidence that M_1 is preferred over M_0, since $\log_{10} K < 2$ always.

To summarise, scalar clouds with mass couplings in the range $\alpha \in [0.01, 0.045]$ can be ruled out, for cloud masses $\Lambda \gtrsim 0.1\%$ of the central SMBH mass (equivalent to $\delta M \sim 4000\, M_\bullet$). This is similar to the result of Ref. [167], who provided a 1σ upper bound of 0.1% of $M_\bullet$ on the observational dark mass within the orbit of S2 assuming a Plummer profile for the density distribution.

For certain scalar couplings α, observational data are well fitted by a non-zero value of Λ of order 10^{-3}. However, all these values of Λ are consistent with zero within the $3\,\sigma$ confidence interval. The computation of the Bayes factor showed that this perturbed model is only mildly preferred over the non-perturbed model predicting a single central BH in vacuum.

In conclusion, the evidence is no strong enough to claim the existence of a scalar cloud around SgrA* as described by this setup.

6.2.4 *Discussion*

Stronger constraints on the scalar cloud's mass require more years of observations or the inclusion of other stars of the S-cluster in the fit. However, since the potential describing the cloud is non-spherically symmetric, the inclination of stars with each other plays a fundamental role - at least in theory - and this same analysis can not be performed straightforwardly.

For the same reason, we were forced to set an initial angular position for S2 co-planar with the BH equator ($\theta = \pi/2$). This is the simplest choice but also the one that maximises the scalar potential in Eq. (6.18), i.e., the chances to actually detect the cloud. One can try to quantify the error in setting the initial angular position of the star by looking at the difference in the orbits for two different initial inclinations: $\theta = \pi/2$ and $\theta = 0$, focusing on the interesting range of α: $0.01 \leq \alpha \leq 0.045$. The maximum relative (percentage) difference in the astrometry is achieved for $\alpha = 0.01$, where ΔDEC $\sim$ ΔR.A. $\approx 25\%$, while the maximum difference in the RV is found to be $\Delta V_R \approx 15\%$ for $\alpha = 0.045$.

Although these differences may seem significant, one should notice that: (i) they would be smaller for any values of $\theta \in [0, \pi/2]$ and (ii) they are only reached in correspondence of the two periastron passages, while they remain much smaller over the rest of the orbit. Hence we are relatively confident that there will be no significant changes in the best-fit parameters we found for different initial inclinations of S2.

In addition, Ref. [320] showed that also the inclination of SgrA*'s spin with respect to the observer frame plays an important role in the effects the cloud has on S2 motion. Indeed, results including the motion of other S-stars and SgrA*'s spin direction are left for future works.

The increased sensitivity of GRAVITY+ and the patrol field of view of ERIS strongly increase the prospects of detecting and tracking further stars in inner orbits, allowing to test also those values of the mass coupling α that would be compatible with a superradiant growth of the cloud.

6.3 CONSTRAINING VECTOR CLOUDS USING S2 MOTION

In the previous section, the possibility that a massive scalar field clusters around SgrA* in the form of a cloud was investigated. Here, we focus on a similar system: a massive vector cloud. As scalar fields, massive vector fields can form bound states around Kerr BHs, giving rise to stationary clouds.

At the linear level and using the small coupling approximation, it has been shown that the superradiant instability is triggered on a timescale $\tau_I \propto \alpha^{-7}$ for vector clouds when compared to the scalar case of $\tau_I \propto \alpha^{-9}$ [324–327]. Hence, vector clouds grow faster than their scalar counterparts and the field's mass m_v needed to make them grow in a timescale shorter than the cosmic age is much smaller, making them more likely to be observed.

6.3.1 *Setup*

A massive vector field, or Proca field, A_μ is described by the Lagrangian

$$\mathfrak{L} = -\frac{1}{4}F_{\mu\nu}F^{\mu\nu} - \frac{1}{2}\mu^2 A_\mu A^\mu \,, \tag{6.27}$$

with A^μ being the electromagnetic four-potential and satisfying the Proca equation of motion

$$D_\mu F^{\mu\nu} = \mu^2 A^\nu \,, \tag{6.28}$$

where $F_{\mu\nu} \equiv \partial_\mu A_\nu - \partial_\nu A_\mu$ is the usual electromagnetic tensor. Usually the Proca equation (6.28) can only be solved numerically if evaluated on Kerr metric. However, if the Compton wavelength of the vector field is much larger than the Schwarzschild radius r_S, the bound states of the field are said to be non relativistic and have an hydrogen-like spectrum. Specifically, these states oscillate with frequency $\omega_f \simeq \mu$ and the four-potential can be written as [328]

$$A^\mu(t,x) = \frac{1}{\sqrt{2\mu}}\left(\Psi^\mu(x)e^{-i\omega_f t} + \text{c.c.}\right) . \tag{6.29}$$

In the limit $r \gg r_g$, one can assume that the field Ψ^μ varies on a timescale μ^{-1} and hence that the components of its momentum are non relativistic. In this approximation, the Proca equation becomes a Schröedinger-like equation,

$$\left(\omega_f^2 - \mu^2\right)\Psi^\nu \simeq -\nabla^2\Psi^\nu + \omega^2(1+g^{00})\Psi^\nu \,, \tag{6.30}$$

where the 00 component of the metric is given by $g^{00} = -(1 - r_S/r)$. Hence, the equation takes its Schröedinger-like form which describes the motion in a $1/r$ potential,

$$(\omega_f - \mu)\Psi^\nu \simeq -\frac{\nabla^2}{2\mu}\Psi^\nu + \frac{\alpha}{r}\Psi^\nu \,, \tag{6.31}$$

where we have introduced the dimensionless mass coupling α defined in Eq. (6.8). Because of the Lorentz condition $\partial_t A_0 \simeq \partial_i A_i$, the Ψ_0 component can be expressed in terms of Ψ_i and one can solve Eq. (6.31) only for the spatial components. Since the radial part of the potential is spherically symmetric, Ψ_i can be decomposed as

$$\Psi_i = R^{n\ell}(r) Y_i^{\ell,jm}(\theta,\phi)\,, \tag{6.32}$$

where the $Y_i^{\ell,jm}(\theta,\phi)$ are the so-called pure-orbital vector spherical harmonics and are the eigenfunctions of the orbital angular momentum operator $-r^2\nabla^2 Y_i^{\ell,jm} = \ell(\ell+1)Y_i^{\ell,jm}$ [233, 329]. The radial functions $R^{n\ell}$ are instead hydrogen-like wavefunctions, labeled by the orbital angular momentum index ℓ and the overtone number n.

The fundamental mode of the field, which is also the mode that grows fastest due to superradiant mechanisms [328], is given by $\ell = 0$, $m = j = 1$ and $n = 0$. At leading order in α the term A_0 can be neglected and one can consider only the spatial components of the field, which can be written as [330]

$$A_i^{1011} = \Psi_0 e^{-\frac{\alpha^2 r}{M_\bullet}} \left(\cos(\mu t), \sin(\mu t), 0\right)\,. \tag{6.33}$$

Once the profile is known, the energy-momentum tensor can be computed following Ref. [315], whose general form is given by

$$\begin{aligned} T_{\mu\nu} = {} & \frac{1}{2}\left(F_{\mu\sigma}\bar{F}_{\nu\gamma} + \bar{F}_{\mu\sigma}F_{\nu\gamma}\right) g^{\sigma\gamma} - \frac{1}{4} g_{\mu\nu} F_{\sigma\tau}\bar{F}^{\sigma\tau} \\ & + \frac{1}{2}\mu^2\left(A_\mu \bar{A}_\nu + \bar{A}_\mu A_\nu - g_{\mu\nu} A_\sigma \bar{A}^\sigma\right)\,. \end{aligned} \tag{6.34}$$

Assuming the field is real (cfr. Eq. (6.33)) and taking the leading order in α, i.e., neglecting all the spatial derivatives, one obtains

$$T_{\mu\nu} \approx \left(\mu \Psi_0 e^{-\alpha^2 r/M_\bullet}\right)^2 \times \begin{pmatrix} 1 & 0 & 0 & 0 \\ 0 & \cos(2\mu t) & \sin(2\mu t) & 0 \\ 0 & \sin(2\mu t) & -\cos(2\mu t) & 0 \\ 0 & 0 & 0 & 0 \end{pmatrix}\,. \tag{6.35}$$

As done in Sec. 6.2, the energy density can be obtained taking the 00 component of $T_{\mu\nu}$ and it reads

$$\rho = \frac{\Psi_0^2 \alpha^2}{M_\bullet^2} e^{-\frac{2\alpha^2 r}{M_\bullet}}\,, \tag{6.36}$$

which coincides with the expression derived in Ref. [330].

One can integrate the energy density in (6.36) to relate the amplitude of the field Ψ_0 with the mass of the vector cloud, obtaining

$$M_{\rm cloud} = \frac{\pi \Psi_0^2 M_\bullet}{\alpha^4}. \tag{6.37}$$

In Fig. 6.4 we report the density in Eq. (6.36) for different values of α and $\Lambda = 10^{-3}$, compared with S2 orbital range. As in the case of scalar clouds, ρ only reaches its maximum in correspondence of S2 orbital range for some specific values of the coupling α.

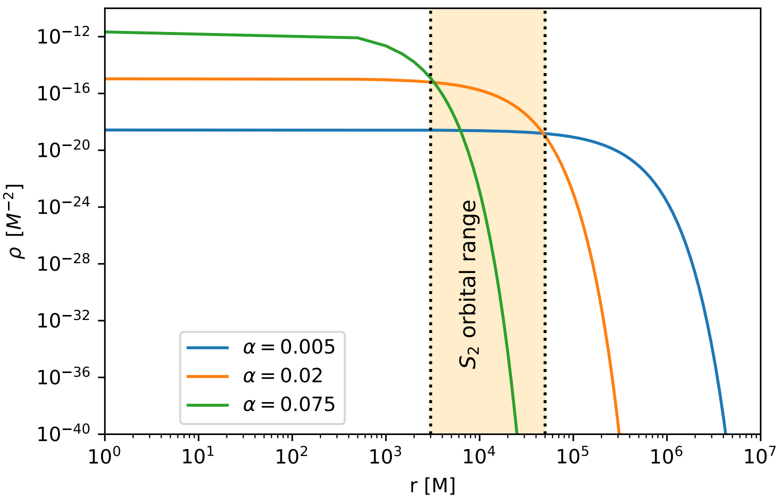

Figure 6.4: Energy density of Eq. (6.36) for different values of the coupling α. As in the case of scalar cloud, ρ reaches its maximum in correspondence of S2 orbital range only if specific values of α are considered. Here $\Lambda = 10^{-3}$.

Again, from the energy density in Eq. (6.36) one can get the potential generated by the cloud solving Poisson's equation: $\nabla^2 U_V = 4\pi\rho$ and using the spherical harmonic decomposition of Ref. [236] to get:

$$U_V = \frac{\Lambda}{r}\left(M_\bullet - e^{-2r\alpha^2/M_\bullet}\left(M_\bullet + r\alpha^2\right)\right). \tag{6.38}$$

6.3.2 *Effects of the cloud on S2 orbit with osculating elements*

We start our analysis of the effects of vector cloud on S2 motion applying the method of osculating elements, following the treatment of Poisson and Will [236]. The basic idea is to treat the effect of the vector cloud as a perturbation of the Newtonian acceleration, assuming that the Keplerian description of the orbit is still approximately true.

In this way, one is able to express the equations of motion in terms of the Keplerian elements $e, a, i, \omega, \Omega, \mathcal{M}_0$ (that we recall to be eccentricity, semi-major axis, inclination, argument of the periastron, longitude of the ascending node and mean anomaly at epoch, respectively), which would be constant in a pure Newtonian setup, and see how the perturbing force modifies them.

In order to do so, one needs to introduce a vectorial basis adapted to the orbital motion of the binary system BH-S2: $(\mathbf{n}, \boldsymbol{\lambda}, \mathbf{e}_z)$, where $\mathbf{n} = \mathbf{r}/r$, $\mathbf{e}_z = \mathbf{h}/h$ with $\mathbf{h} := \mathbf{r} \times \mathbf{v}$, and $\boldsymbol{\lambda}$ is orthogonal to both $\mathbf{n}$ and $\mathbf{e}_z$. One can also safely assume that the mass of the star is negligible compared to the BH mass $M_\bullet$ (their ratio being $m_{S2}/M_\bullet \sim 10^{-5}$).

The perturbing force can be decomposed as:

$$\mathbf{f} = \mathcal{R}\mathbf{n} + \mathcal{S}\boldsymbol{\lambda} + \mathcal{W}\mathbf{e_z}\,. \tag{6.39}$$

The variation of the orbital elements in terms of the perturbing force components is given by [236, 331]

$$\begin{aligned}
\frac{da}{dt} &= 2\sqrt{\frac{a^3}{M_\bullet(1-e^2)}}\left[e\sin\phi\mathcal{R} + (1+e\cos\phi)\mathcal{S}\right], && (6.40)\\
\frac{de}{dt} &= \sqrt{\frac{a(1-e^2)}{M_\bullet}}\Bigg[\sin\phi\mathcal{R} \\
&\quad + \frac{2\cos\phi + e(1+\cos^2\phi)}{1+e\cos\phi}\mathcal{S}\Bigg], && (6.41)\\
\frac{d\omega}{dt} &= \frac{1}{e}\sqrt{\frac{a(1-e^2)}{M_\bullet}}\Bigg[-\cos\phi\mathcal{R} + \frac{1+2e\cos\phi}{1+e\cos\phi}\sin\phi\mathcal{S} \\
&\quad - e\cot i\frac{\sin(\omega+\phi)}{1+e\cos\phi}\mathcal{W}\Bigg], && (6.42)\\
\frac{di}{dt} &= \sqrt{\frac{a(1-e^2)}{M_\bullet}}\frac{\cos(\omega+\phi)}{1+e\cos\phi}\mathcal{W}, && (6.43)\\
\sin i\frac{d\Omega}{dt} &= \sqrt{\frac{a(1-e^2)}{M_\bullet}}\frac{\sin(\omega+\phi)}{1+e\cos\phi}\mathcal{W}, && (6.44)\\
\frac{d\mathcal{M}_0}{dt} &= -\sqrt{1-e^2}\left(\frac{d\omega}{dt} + \cos i\frac{d\Omega}{dt}\right) \\
&\quad - \sqrt{\frac{a}{M_\bullet}}\frac{2(e^2-1)}{(1+e\cos\phi)}\mathcal{R}, && (6.45)
\end{aligned}$$

where the radial coordinate has been expressed as $r = a(1-e^2)/(1+e\cos\phi)$.

Once the variation in time of the orbital elements is known, one can compute the secular change of the orbital element μ^a over a complete orbit using:

$$\Delta\mu^a = \int_0^{2\pi} \frac{d\mu^a}{d\phi} d\phi\,, \tag{6.46}$$

where

$$\frac{d\mu^a}{d\phi} = \frac{d\mu^a}{dt}\frac{dt}{d\phi} \tag{6.47}$$

and

$$\frac{d\phi}{dt} = \sqrt{\frac{M_\bullet}{a^3(1-e^2)^3}}(1+e\cos\phi)^2\,. \tag{6.48}$$

Due to the spherical symmetry of the energy distribution in Eq. (6.36), the only non-zero component of $\mathbf{f}_V$ is the radial one:

$$\mathcal{R}_V = \frac{\Lambda}{M_\bullet r^2}\left[-M_\bullet^2 + e^{-2r\alpha^2/M_\bullet}\left(M_\bullet^2 + 2M_\bullet r\alpha^2 + 2r^2\alpha^4\right)\right]\,, \tag{6.49}$$

while $\mathcal{S}_V = \mathcal{W}_V = 0$.

In Figure 6.5 the variation of the orbital elements $\Delta\mu^a/\Lambda$ due to the presence of the vector cloud for different values of the coupling α is shown. The secular change is negligible for both the eccentricity e and the semi-major axis a.

The change in the mean anomaly at epoch $\mathcal{M}_0$ is instead proportional to α, increasing monotonically. $\mathcal{M}_0$ is directly related to the time of pericenter passage t_p: a larger mean anomaly at the epoch corresponds to a later pericenter passage. The only meaningful change in the orbital elements is found in $\Delta\omega$, which quantifies the precession effect on the orbit. First of all, one can observe that $\Delta\omega < 0$ always. This is a consequence of the fact that the presence of an extended mass within the orbit of S2 would produce a retrograde precession in the orbit [170].

Unsurprisingly, its maximum variation is found in the range

$$0.003 \lesssim \alpha \lesssim 0.03\,. \tag{6.50}$$

Indeed, as in the case of scalar clouds, this behaviour is expected if one computes the effective peak position of the energy distribution in Eq. (6.36),

$$R_{\text{peak}} = \frac{\int_0^\infty \rho r dr}{\int_0^\infty \rho dr} = \frac{M_\bullet}{2\alpha^2}\,, \tag{6.51}$$

which, for the values of α reported in Eq. (6.21), corresponds to

$$500\,M_\bullet \lesssim R_{\text{peak}} \lesssim 50000\,M_\bullet\,, \tag{6.52}$$

i.e., it roughly matches the orbital range of S2 ($3\cdot 10^3\,M_\bullet \lesssim r_{s2} \lesssim 5\cdot 10^4\,M_\bullet$). This result shows that the maximum variation in ω is found when the star crosses regions of higher (vector) density, while its orbit remains basically unaffected if the cloud is located away from its apoastron or too close to the central BH mass.

It is interesting to see how the previous results change if one includes the first PN correction to the equations of motion via Eq. (5.14).

This corresponds to have a total acceleration

$$\mathbf{a} = -\frac{M_\bullet \mathbf{r}}{r^3} + \mathbf{a}_V + \mathbf{a}_{1\text{PN}}\,, \tag{6.53}$$

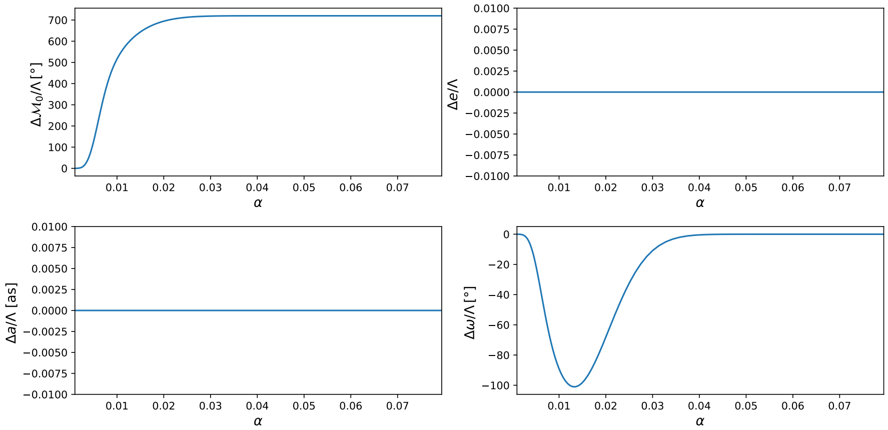

Figure 6.5: Variation of the orbital elements $\Delta\mu^a/\Lambda$ over an entire orbit for different values of the coupling constant α when only the vector cloud is present. The maximum variation in $\Delta\omega/\Lambda$ is roughly found in the range $0.003 \lesssim \alpha \lesssim 0.03$.

The decomposition of the acceleration in Eq. (5.14) into the basis $(\mathbf{n}, \boldsymbol{\lambda}, \mathbf{e}_z)$ has been done in Ref. [236] and it reads

$$\begin{aligned} \mathcal{R}_{\rm 1PN} &= \frac{M_\bullet}{r^2}\left(4\dot{r}^2 - v^2 + 4\frac{M_\bullet}{r}\right) , \\ \mathcal{S}_{\rm 1PN} &= \frac{M_\bullet}{r^2}\left(4\dot{r}r\dot{\phi}\right) , \\ \mathcal{W}_{\rm 1PN} &= 0 . \end{aligned} \tag{6.54}$$

In order to express everything in terms of the orbital elements, one can use the expression for the velocities reported in Ref. [236], i.e.,

$$\dot{r} = \sqrt{\frac{M_\bullet}{a(1-e^2)}}\, e \sin f , \tag{6.55}$$

and

$$r\dot{\phi} = \sqrt{\frac{M_\bullet}{a(1-e^2)}}\,(1 + e\cos f) \tag{6.56}$$

where f is the true anomaly defined as $f \equiv \phi - \omega$.

In this second case $\Lambda = 10^{-3}$ is set, which corresponds to the current upper limit obtained by the GRAVITY collaboration for the fractional mass of an extended mass distribution around SgrA* (see previous Section and Ref. [167]).

In Figure 6.6 we show the variation of the orbital elements when the first PN correction is included in the equations of motion. Opposite to the previous case, here, the variation of the argument of the pericenter $\Delta\omega$ can be either positive or negative, according to the value of α. Indeed now the retrograde precession induced by the vector cloud is compensated by the (prograde) Schwarzschild precession due to the

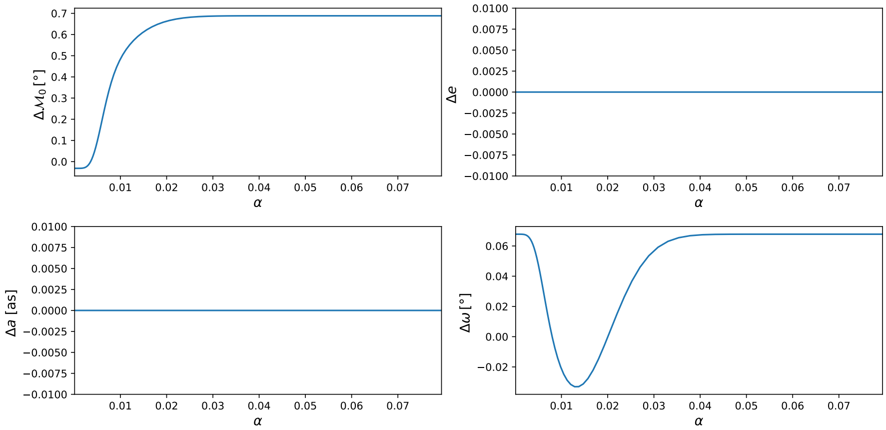

Figure 6.6: Variation of the orbital elements $\Delta\mu^a$ over an entire orbit for different values of the coupling constant α when one includes the Schwarzschild precession in the equation for the osculating elements. Here $\Lambda = 10^{-3}$. The maximum variation is still found in $0.003 \lesssim \alpha \lesssim 0.03$.

1PN correction in the equations of motion, and its maximum value corresponds to $\Delta\omega \simeq -1.8'$, which is smaller than the previous case with $\Lambda = 10^{-3}$ ($\Delta\omega \simeq -6'$).

6.3.3 *Constraints on the fractional mass* Λ

As in the scalar cloud case, one can now perform the MCMC analysis adding the fractional mass Λ to the list of fitting parameters in (5.19). To do so, we follow the procedure explained in Sec. 5.3. In Figure 6.7 we report the best-fit values of Λ with relative 1σ uncertainties obtained via the χ^2 minimisation and we compare the range of α with the effective peak position of the cloud in Eq. (6.51).

The smallest uncertainties for Λ are found roughly in the range of Eq. (6.21), which is slightly different from the scalar cloud case and in agreement with the orbital variation reported in Figure 6.6.

After performing the MCMC analysis, one can look for the MLE $\hat{\Lambda}$, that again corresponds to the value that maximises the posterior density distribution reported in Figure 6.8, as a consequence of using flat priors and a Gaussian likelihood.

In Table 6.2 the values of $\hat{\Lambda}$ with relative 1σ uncertainties are reported, together with the value of the Bayes factor $\log_{10} K$ evaluated via Eq. (5.30). As in the scalar case, when the posterior distribution is found to be non-normal and peaked at zero, the 1σ (3σ) confidence interval are estimated looking for that value of Λ such that roughly the 68% (99%) of $P(\Lambda_\alpha|D)$ lies below that value.

When $\alpha \gtrsim 0.03$, the posterior of Λ starts to be flat, with a sudden drop around $\Lambda \simeq 10^{-2}$. One can show that for flat distributions defined in an interval $[a, b]$, the mean is given by $(a-b)/2$ while

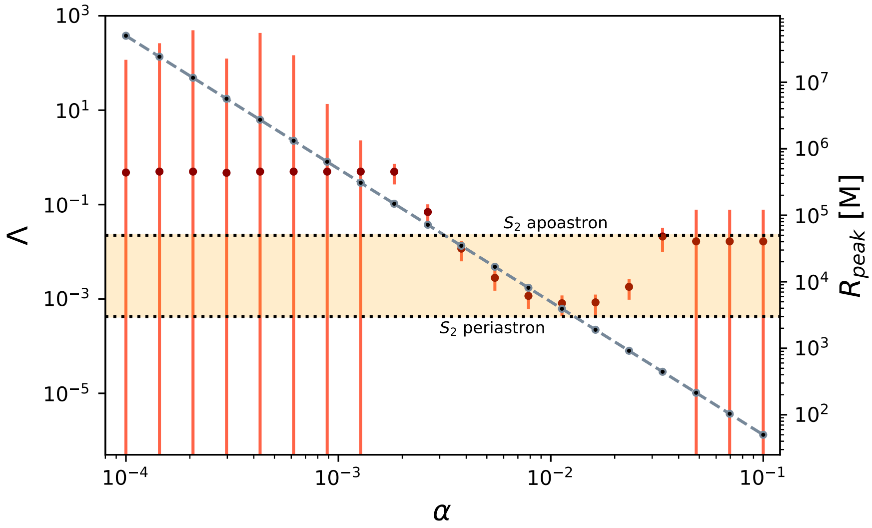

Figure 6.7: Best-fit values for Λ and relative 1σ uncertainties as function of the coupling α obtained minimising the χ^2. The grey dashed line represents the effective peak position of the vector cloud given by Eq. (6.51), while the orange band gives the orbital range of S2.

the variance is $(b-a)^2/12$ [332]. These are the values reported in Table 6.2. However, what is important to notice in these cases is that for $\alpha \gtrsim 0.03$ ($R_{\text{peak}} \lesssim 550\, M_\bullet$), it is not possible to determine a unique value for Λ that best fits the data, confirming the expectation from the χ^2 minimisation.

When α is in the range of Eq. (6.21) the posterior distributions of Λ are Gaussian whose means and standard deviations are reported in Table 6.2. For all cases considered in this range, $\hat{\Lambda} \sim 10^{-3}$ with 1σ uncertainties roughly of the same order of magnitude. This makes all the $\hat{\Lambda}$ values derived from the MCMC analysis compatible with zero within the 3σ confidence level. In addition to this, the associated Bayes factors always have $\log K < 2$. This result, according to the literature [301], shows no statistical evidence in favour of the BH plus vector cloud model with respect to the non-perturbative case in vacuum. Hence, one can only derive an upper limit on the fractional mass of $\Lambda \lesssim 10^{-3}$ at 3σ confidence level.

As opposed to the scalar case, the upper bound derived in this work for vector clouds actually imposes a limit on the superradiant growth of the cloud, that in general would lead to transfer up to $\sim \mathcal{O}(10)\%$ of the BH mass into the vector cloud [311, 321, 333]. In this work we showed that for a field's effective mass of $m_v \sim 10^{-19} - 10^{-18}$ eV, the mass of the cloud around SgrA* can not exceed the limit $M_{\text{cloud}} \lesssim 0.1\% M_\bullet$. Assuming a BH spinning with $j \sim 0.5$ (an indicative value), the growth timescale of the cloud can vary between $10^5 - 10^{10}$ yrs, exact values depend on the effective mass m_v. This estimate is below

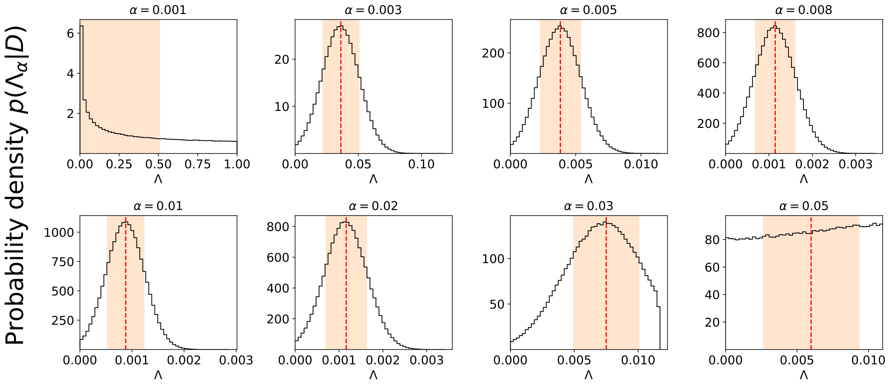

Figure 6.8: Posterior probability densities $p(\Lambda_\alpha|D)$ for different values of α. Red dashed lines represent the mean value of the distributions (which coincides with the MLE $\hat{\Lambda}$), while orange bands correspond to 1σ confidence level, such that $\approx 68\%$ of $p(\Lambda_\alpha|D)$ lies in that region.

the age of the Universe ($t_{\rm age} \sim 10^{10}$ yrs), making the superradiant process and the above constraints relevant.

6.3.4 *Environmental effects*

All the above results are obtained neglecting the backreaction effects of the matter on the motion of S2. Indeed, the presence of a matter distribution induces a gravitational drag force on the body moving in it, with the consequence that part of the material is dragged along the motion producing a dynamical friction force on the main body [222, 334]. It has been shown that dynamical friction induced by ultralight bosons may play a significant role in the strong regime [335, 336]. Here we investigated whether dynamical friction affects S2 motion too.

In a Newtonian setup, including the dynamical friction force means adding the following two components to the equations of motion [337]:

$$\begin{aligned} F_{{\rm DF},r} &= F_{\rm DF}\frac{\dot{r}}{v}\,, \\ F_{{\rm DF},\phi} &= F_{\rm DF}\frac{r\dot{\phi}}{v}\,, \end{aligned} \tag{6.57}$$

where $v^2 = \dot{r}^2 + r^2\dot{\phi}^2$, assuming that the motion of S2 happens on the equatorial plane ($\theta = \pi/2$) of the central SMBH.

The term $F_{\rm DF}$ has been derived in Ref. [334] for a perturber in linear motion and it reads

$$F_{\rm DF} = -\frac{4\pi m_{s2}^2 \rho}{v^2} I_v\,, \tag{6.58}$$

α	$\hat{\Lambda}$	$\log_{10} K$
0.001	$\lesssim (0.51, 0.98)$	-0.45
0.003	0.03596 ± 0.01477	-2.09
0.005	0.00379 ± 0.00157	-3.11
0.008	0.00114 ± 0.00047	1.62
0.01	0.00088 ± 0.00036	1.42
0.02	0.00116 ± 0.00047	1.69
0.03	0.00688 ± 0.00263	-2.55
0.04	0.00617 ± 0.00337	-4.77
0.05	0.00592 ± 0.00339	-4.96

Table 6.2: MLE $\hat{\Lambda}$ with associated 1σ error and Bayes factors $\log_{10} K$ for different values of α. The measurements for each α are not independent (the same orbit was used to derive them) and therefore cannot be combined to derive a more stringent upper limit. For non-normal distributions we report Λ_1 and Λ_2 defined such that $P(\Lambda_\alpha < \Lambda_1|D) \approx 68\%$ and $P(\Lambda_\alpha < \Lambda_2|D) \approx 99\%$ of $P(\Lambda_\alpha|D)$.

with

$$I_v = \begin{cases} \frac{1}{2}\log\left(\frac{1+v/c_s}{1-v/c_s}\right) - \frac{v}{c_s}\,, & v < c_s \\ \frac{1}{2}\log\left(1-\frac{c_s^2}{v^2}\right) + \log\left(\frac{vt}{r_{\min}}\right)\,, & v > c_s\,, \end{cases} \tag{6.59}$$

where ρ is the density of the matter distribution in Eq. (6.36), m_{s2} is the mass of the star S2 which is taken to be $m_{s2} = 14\,M_\odot$ and c_s is the speed of sound in the medium which constitutes the environment. Kim and Kim [338] showed that Eq. (6.58) correctly reproduces the results obtained for circular orbits if one substitutes $vt \to 2r(t)$.

Despite the orbit of S2 is far from being circular, one can still use Eqs. (6.57) in a first approximation.

To have a complete understanding, four different values of the speed of sound c_s for both the supersonic ($c_s = 10^{-6}$, $c_s = 10^{-3}$) and the subsonic ($c_s = 0.1$, $c_s = 0.03$) regimes were tested.

We set $\Lambda = 10^{-3}$ since it corresponds to the maximum allowed value of the fractional mass and we tested different values of α.

Results are basically independent on c_s and the maximum difference in both the astrometry and the radial velocity with respect to the case where no dynamical friction is implemented is found to be always negligible.

In Figure 6.9 we report the absolute difference in DEC, RA and RV in the supersonic case with $c_s = 10^{-3}$ and different values of α. Overall, the effect of dynamical friction is at most 10^{-5} mas in the astrometry and $\approx 10^{-3}$ km/s in the RV, and in both cases is reached around periastron passages. Overall, it remains well below the current (and future) instrument precision and can be neglected.

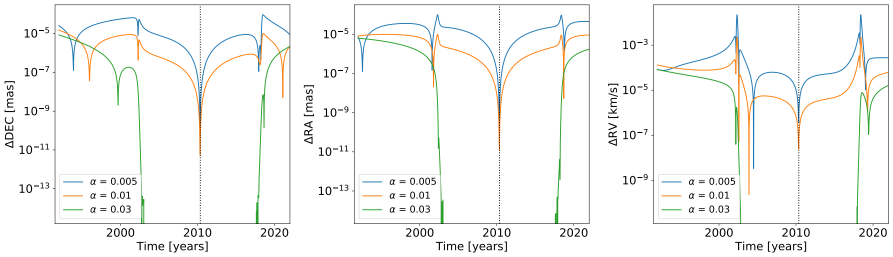

Figure 6.9: Absolute difference in DEC, RA and RV between the case where dynamical friction is implemented in the supersonic case with $c_s = 10^{-3}$ and the case where no dynamical friction is present. Here $\Lambda = 10^{-3}$. The difference is maximum around the periastron passages and minimum at the apoastron (black dotted line). Overall, they remain far below the current instrument threshold.

The same analysis is performed considering the scalar cloud model implemented in Sec. 6.2 and the Plummer density profile (2.7) tested in Ref. [167]. In both cases, results are similar to those of Figure 6.9, leading to the conclusion that dynamical friction effects can be safely neglected.

Along the same line, one can try to compute the effect that regular gas around SgrA* has on S2 orbit. Gillessen et al. [339] detected a drag force acting on the gas cloud G2 and they derived an estimate for the number density of the gas ambient. Here we used their same formulation for the drag force, meaning

$$F_{\text{drag}} = c_D r^{-\gamma} v^2 m_{s2}\,, \tag{6.60}$$

where $\gamma = 1$, v is the relative velocity between the medium and the star, that, following Ref. [339], is assumed to be equal to the velocity of the star itself. c_D parametrizes the strength of the drag force and it is related to the normalised number density of the gas ambient. Gillessen et al. [339] derived $c_D \sim 10^{-3}$ studying the gas cloud G2, and this is the value used in this work as well. In this case no vector cloud is present ($\Lambda = 0$) and only the force contribution due to the presence of gas is considered.

The maximum difference induced by the drag force exerted by the gas ambient on the astrometry and the radial velocity of S2 is of order $\sim 10^{-6}$ mas and $\sim 10^{-3}$ km/s, respectively. Hence, also the contribution due to regular gas around SgrA* has a negligible effect on S2.

We also note that the difference induced by the presence of gas is comparable with the effect produced by dynamical friction. As a consequence, even with the development of future instruments and the advent of GRAVITY+, it will still be hard to disentangle the two effects.

6.3.5 *Discussion*

In this work we continued the analysis of superradiant clouds clustered around SgrA*. Specifically, a massive vector field is considered, which gives rise to a spherically symmetric cloud. The MCMC analysis confirmed the current upper bound for the fractional mass of $\Lambda \lesssim 0.1\% M_\bullet$, recovering previous results on extended masses [167, 340]. Despite the values of the mass of the field that one can actually test with S2 motion is roughly the same in both the scalar and vector cloud case, in the latter these values can effectively engage a superradiant instability in a timescale smaller than the cosmic age. This strongly constrains the mass of a possible superradiant cloud at the GC, improving the theoretical bound that leads to have masses up to two order of magnitude larger [311, 321, 333].

Also, the effect of the environment on S2 orbit was investigated for the first time. Both the dynamical friction exerted by the medium on the star and the effect of ambient gas around SgrA* were considered. In both cases, the effect on the astrometry and the RV of S2 are negligible.

This analysis was also extended to the scalar cloud case in Sec. 6.2 and to the Plummer profile, showing that even in those cases both effects can be neglected. However, since the difference in the astrometry and the RV induced by those effects is of the same order of magnitude, it will be difficult to separate them even with the advent of GRAVITY+.

7

TESTING EXTENDED THEORIES OF GRAVITY

As mentioned in the introductory chapter, GR is a successful theory of gravity whose predictions have been largely tested at Solar System scales and that perfectly reproduces current observations in GWs astronomy and binary pulsars [28]. Although no significant deviation from GR has been currently detected, there are observational evidences, such as the rotational curve of galaxies or gravitational lensing effects [37], that can not be explained by means of GR only.

One way to address these inconsistencies is to directly modify GR, such that the gravitational potential in the weak field limit becomes scale dependent with the introduction of a so-called "fifth force". The latter emerges in the weak field limit as a Yukawa-like modification of the Newtonian potential, which naturally depends on the length scale considered.

Due to the high impact that a discovery of a fifth force would have, the presence of a Yukawa modification has been largely investigated in the past. The strongest constraints come from the Lunar Laser Ranging [341] and the motion of planets in the Solar System [342, 343].

The discovery of orbiting stars around the GC [161, 344–348], all located within one arcsecond distance from the SMBH, SgrA*, allows to test GR in a completely different environment from the Solar System.

The importance of such a test resides in the fact that many ETGs may suffer from a screening mechanism, which turns the field properties into environment-dependent quantities. The general idea is that the effective potential felt by the extra field introduced in the theory depends explicitly on the environment. This dependence can either be incorporated in the effective mass of the field, like the chameleon mechanism [349], in the coupling to matter, like the symmetron mechanisms [349] or in the kinetic function, as in the Vainshtein mechanisms [350]. All these examples only concern scalar fields, but screening mechanisms for vector and tensor fields have been also proposed [351, 352]. In all cases, the extra field becomes ineffective in the local universe, making it unobservable.

Several works have used either mock data or the measurement of SP in S2 orbit to test the strength of a possible Yukawa interactions [197, 353–358] also including the presence of an (expected) bulk mass distribution around SgrA* [359].

In this chapter S2 data will be used to constrain the intensity of a possible Yukawa correction to the Newtonian force. Although we do not expect our results to deviate consistently from the literature, a full analysis of S2 motion including GRAVITY data, that dominate the χ^2 due to their very small uncertainties, is still missing and, as we will see, allows to put much stringent constraints than previous estimates (e.g. those obtained by the UCLA group in 2017 [360]). The results presented here are still work in progress and have only been partially checked by the Collaboration.

7.1 SETUP

7.1.1 *Yukawa-like potential*

A Yukawa-like interaction emerges quite naturally in the weak field limit of several ETGs, e.g. Scalar-Tensor-Vector theories [193], massive gravity theories [361, 362], theories in higher dimensions with Kaluza-Klein compactification [363, 364], massive Brans-Dicke theories [365, 366] or $f(R)$ theories [367]. But the fifth-force scenario also appears in some specific models for DM [368–370].

The Yukawa-like potential will look like

$$U = -\frac{M_\bullet}{r}\left(1 + \alpha e^{-r/\lambda}\right) , \tag{7.1}$$

where α represents the strength of interaction and λ is a scale parameter which depends on the specific theory considered. For instance, when new massive fields are included in the theory, λ represents the Compton wavelength of the field, which is related to its mass via $m_\varphi = h/c\lambda$.

The parameter α is well constrained at Solar System scales and on Earth-based laboratories [342, 371, 372], with very stringent upper bounds in the range $10^7 \lesssim \lambda \lesssim 10^{14}\,\mathrm{m}$. In the context of S-stars, a previous study of the Yukawa-like potential using the motion of S2 has been performed by the UCLA group [360], considering a scalelength range $10^{12} \lesssim \lambda \lesssim 10^{14}\,\mathrm{m}$. The more stringent upper bound is found to be $|\alpha| < 0.016$ for $\lambda = 150\,\mathrm{AU}$ ($\sim 2.2 \cdot 10^{13}\,\mathrm{m}$), while the same upper limit becomes broader for smaller and larger values of λ (cfr. Figure 7.4).

7.1.2 1*PN correction and Yukawa interaction*

Recently, Jovanović et al. [373] constrained the parameters of the potential in Eq. (7.1) using S-stars and assuming that at first PN order both the GR and the Yukawa contributions are present, the latter acting as a correction to the observed SP. Despite a formal PPN parametrization is not possible when a massive field and a Yukawa correction are

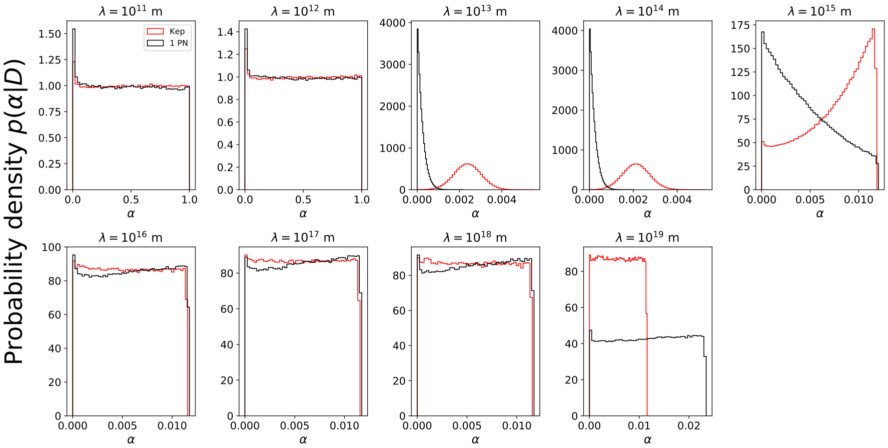

Figure 7.1: Posterior probability densities $P(\alpha|D)$ for different values of the scalelength λ. Red posteriors represent the Keplerian case in Sec. 7.1.1 while black posteriors correspond to the 1 PN case of Sec. 7.1.2.

present [366], one can still derive the equations of motion assuming the GR parameters, $\gamma = \beta = 1$. The latter assumption comes from the estimates obtained by different experimental observations (see e.g. [28, 236]) and it is valid for those ETGs which are indistinguishable from GR at first PN order.

The total acceleration felt by the star can be expressed as:

$$\mathbf{a}_{\text{tot}} = \mathbf{a}_{\text{New}} + \mathbf{a}_{\text{Yuk}} + \mathbf{a}_{1\text{PN}} \tag{7.2}$$

where the contribution given by $\mathbf{a}_{\text{New}} + \mathbf{a}_{\text{Yuk}}$ is derived from the potential in Eq. (7.1), while $\mathbf{a}_{1\text{PN}}$ is reported in Eq. (5.14).

In both cases the dataset used is the one reported in Sec. 5.1, while the fitting method is explained in Sec. 5.3, where the parameter α is added to the list in (5.19) and the length scale λ is kept fixed, picking almost equally spaced values in the range $10^{11} \leq \lambda \leq 10^{19}$ m.

7.2 CONSTRAINTS ON THE STRENGTH OF THE FIFTH FORCE

In Figure 7.1 we report the posterior distributions $P(\alpha|D)$ for different fixed values of the scalelength λ obtained by EMCEE, comparing the setups of Sec. 7.1.1 and Sec. 7.1.2. When $\lambda \leq 10^{12}$ m the posterior $P(\alpha|D)$ is flat in the full range $0 < |\alpha| < 1$ in both cases, with uncertainty of order $\sigma_\alpha \sim 10^{-1}$. One can understand this result in terms of the precession effect that the Yukawa potential induces in the orbit of S2.

Following Ref. [374] one can compute the precession angle in a full orbit as

$$\Delta\phi_p = -\frac{2L}{M_\bullet e^2} \int_{-1}^{1} \frac{dz\, z}{\sqrt{1-z^2}} \frac{dU(z)}{dz}\,, \tag{7.3}$$

where $U(z)$ is the perturbing potential at radius $r = L/(1+ez)$ with $L = a(1-e^2)$.

When $\lambda = 10^{11} - 10^{12}\,\mathrm{m}$, the precession angle $\Delta\phi_p \sim 0$ for any value of α and hence it has no detectable effect on the orbit.

When the length scale becomes comparable with S2 orbital range ($\lambda = 10^{13} - 10^{14}\,\mathrm{m}$) the effect on the orbit is maximised and one can clearly see the difference between the two cases: if only the Yukawa potential is present, the posterior $P(\alpha|D)$ is a Gaussian distribution with mean around $\alpha \sim 0.002$, which corresponds to have $\Delta\phi_p \sim 0.12°$. Taking the most up-to-date value of the SP reported in Ref. [167], $\Delta\phi_{\mathrm{Sch}} = 12.1' \times (0.99 \pm 0.15) = (0.20 \pm 0.03)°$, one can see that the precession angle induced by the Yukawa potential is compatible, within the 3σ uncertainties, with $\Delta\phi_{\mathrm{Sch}}$. In the absence of the first PN correction in the equations of motion the prograde precession detected in S2 [219] is compensated by the presence of the Yukawa potential.

Indeed, when the 1 PN correction is included as reported in Sec. 7.1.2, the posterior of α for the same λ becomes peaked around 0 with uncertainty $\sigma_\alpha \sim 10^{-4}$.

What is probably the most interesting result of this analysis appears in correspondence of larger length scales. For $\lambda > 10^{15}\,\mathrm{m}$, and in both the Newtonian and the 1 PN case, the posteriors $P(\alpha|D)$ are flat in the interval $0 < \alpha \lesssim 0.012$ with a sudden drop in correspondence of this upper limit. For such lengthscales the precession effects is smaller than $\Delta\phi_{\mathrm{Sch}}$ for any value of α and thus one expects to recover a flat distribution as in the first two cases considered.

However, there are reasons to believe that this is not a numerical artefact that follows from the failure of the MCMC analysis, but rather a consequence of the exponential growth of the χ^2 in correspondence of $\alpha \gtrsim 10^{-2}$, even if one allows the other parameters to vary in a larger parameter space. This is shown in Figure 7.2, where the quantity $\chi^2/2$ is reported as function of α.

To obtain this plot, we firstly fix the value of the length scale to be $\lambda = 10^{18}\,\mathrm{m}$, then 100 values of the parameters in Eq. (5.19) are randomly extracted from the posterior distributions obtained by EMCEE and, keeping α fixed, the χ^2 is computed. Afterwards, for each value of α, the mean and the standard deviation of the 100 χ^2 are computed and reported in the plot. In this way one is able to estimate the fluctuations of the likelihood due to the variation of other parameters too, not only α. Indeed, the exponential increase starts more or less in correspondence of the upper limit found by EMCEE, $\alpha \sim 0.01$, represented by the red dashed line.

In other words, the best-fit parameters describing S2 orbit are not compatible with a fifth force having an intensity larger than $\alpha \sim 0.01$ at 3σ confidence level, whatever is the length scale considered.

The independence of the results from the parameter λ can be understood in terms of the acceleration felt by the star in its orbital range. As can be seen from Figure 7.3, the absolute difference in the acceleration Δa_{tot} with respect to the case with $\lambda = 10^{16}\,\mathrm{m}$ is of order $10^{-8}\,\mathrm{m/s^2}$

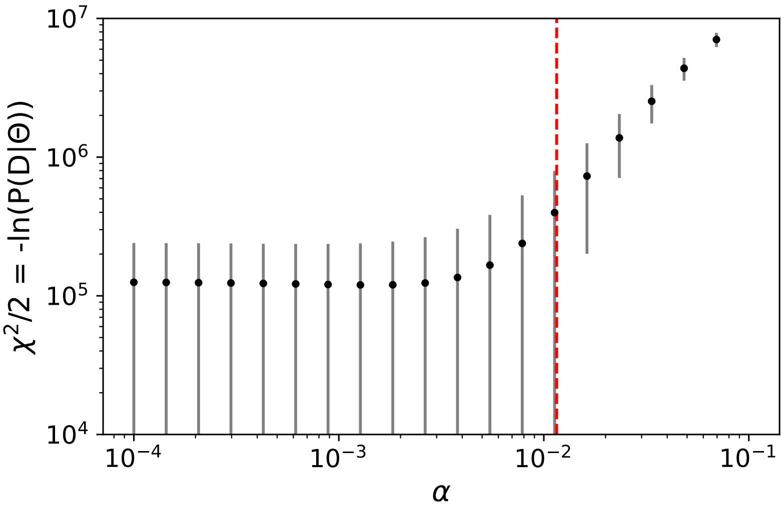

Figure 7.2: $\chi^2/2$ computed for 100 values of the parameters in Eq. (5.19) randomly extracted from their posterior distributions, for any value of α, which is kept fixed. The red dashed line represents the upper limit found by EMCEE above which values of α are not sampled anymore.

for each value of λ tested, much below current instruments' precision. Therefore, one does not expect the results to change for $\lambda \geq 10^{16}$ m.

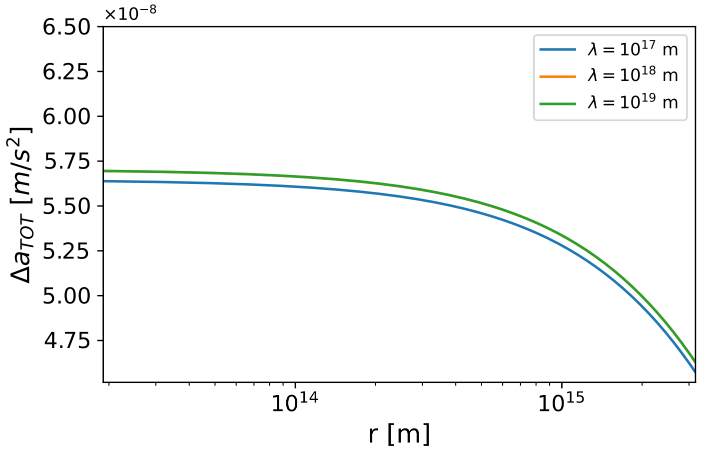

Figure 7.3: Difference in the acceleration in S2 orbital range. Here the difference is computed with respect to the acceleration felt by the star when $\lambda = 10^{16}$ m. Here $\alpha = 0.02$, but results scale with α.

In Figure 7.4 we reported the 95% confidence interval on α as function of λ considering the 1 PN case, since we assumed that the prograde precession detected in S2 orbit is indeed caused by the SP. Compared to the similar analysis performed by Hees et al. [360] one can see that the precision of the GRAVITY instrument allows for much more stringent bounds on α, reaching a plateau of order 10^{-2} for larger values of λ and constraining scale lengths that have not been explored

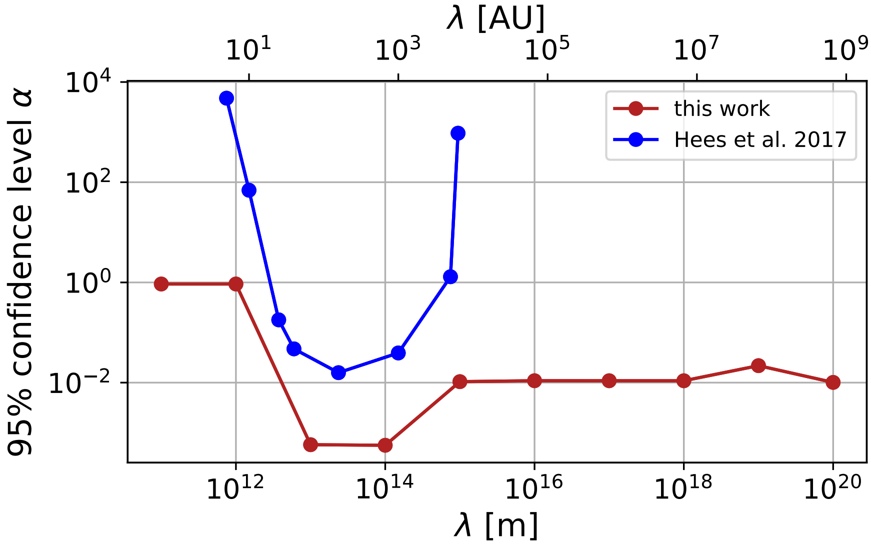

Figure 7.4: 95% confidence interval on α as function of the scalelength λ using GRAVITY data (red dots) and compared with results in Ref. [360] (blue dots).

before with Earth-based experiments [342]. For $70 \lesssim \lambda \lesssim 700$ AU, which roughly corresponds to S2 orbital range, one can place an upper limit of $|\alpha| < 0.001$ at 95% confidence interval, improving the previous estimate by Hees et al. [360] by roughly one order of magnitude.

If one assumes that the interaction is mediated by a massive boson, the scale length λ corresponds to the Compton wavelength of the particle and hence an upper limit on the graviton's mass can be derived. Specifically, since $\alpha = 1$ is excluded at 95% confidence level up to $\lambda \sim 10^{19}$ m, this can be seen as a lower limit on the graviton's wavelength, that translates in an upper limit on the mass $m_g \lesssim 10^{-26}$ eV.

If confirmed, those results would not only improve the current upper limit on α in the regions of the GC that S2 can actually probe, but they would also significantly enlarge the parameter space tested. Moreover, in the context of massive gravity, the upper limit on the graviton's mass derived in this work would be ~ 3 orders of magnitude more stringent than the current upper limit derived by the LIGO-Virgo Collaboration ($m_g \lesssim 10^{-23}$ eV) [375], underlying once again the incredible power of GRAVITY's high-precision astrometry .

8

CONCLUDING REMARKS

With the advent of high technology instruments and pioneering experiments, the gravitational physics field has seen an enormous increase in the available data sources in the last decades. This huge amount of data must be exploited to the full to try to answer those questions about the Universe and the theory of gravity that remain unanswered to this day.

Throughout this work we have shown how studying the motion of a test particle in a certain gravitational background can potentially help to determine the features of the background itself. Studying the geodesic motion in the strong field regime of gravity we showed the potential signatures due to the presence of an hidden compact companion generating a tidal field, while solving the geodesic equations for null particles in the Schwarzschild geometry helped us understand the behaviour of luminosity as seen by a distant observer. The latter analysis showed that current and future EHT measurements will not be able to distinguish between an actual BH and a so-called BH-mimicker, i.e., an horizonless compact object.

In this context it would be particularly interesting to extend the analysis to rotating BHs, showing explicitly the role played by the spin on the observed luminosity and how it affects the measurements.

In the second part of this thesis we focused on the GC and star S2, that constitute the perfect laboratory to look for DM and unveil possible deviations from GR. We exploited the knowledge on profiles describing a scalar or vector field coupled to the gravity sector to determine an upper limit on the extended mass of a boson cloud around SgrA*. This analysis also placed a limit on the superradiant growth of vector clouds at the GC, restricting it by at least two orders of magnitude with respect to what is expected theoretically.

In the same context we also investigated the presence of a possible fifth force in the Universe, which emerges as the weak field limit of many ETGs and also as a possible DM model. The exquisite precision of the GRAVITY instrument allowed us to place much stringent constraints on the intensity of such a force than previous results on the topic [360], showing the importance of performing these tests with high precision instruments.

One of the next goals will be to extend the analysis on the Yukawa potential to other stars in the S-cluster, once that the preliminary results reported in this thesis have been confirmed. Due to the spherical symmetry of the potential, this operation is quite straightforward to perform and it requires only the time to implement and adapt the fitting code.

The importance of fitting multiple stars resides in the specific form that the Yukawa potential has. Indeed, as we have seen in Chapter 7, when fitting orbits to derive constraints on the intensity α, the spatial length-scale λ must be fixed to a specific value. The orbital range of S2 allowed us to place a very stringent constraint of $|\alpha| \lesssim 10^{-3}$ for $\lambda = 10^{13} - 10^{14}$ m, while the same limit becomes broader for larger and shorter length scales. In this sense, including more stars with different orbital ranges in the fit will improve the constraint on α also at different spatial lengths than those proved by S2. Considering the available data at the moment of writing one can expect to improve the constraints on α at least up to $\lambda \sim 10^{15}$ m.

The future appears even brighter, with several experiments on their way to be launched and the update GRAVITY+ on its way to be completed. The increase in capability and the extended field of view of GRAVITY+ will increase the number of observed stars at the GC, aiming to find fainter and closer objects to SgrA*.

While it is clear what kind of orbital parameters the star must have in order to finally measure SgrA* spin [210], what it is still being debated is the way in which astrometric and spectroscopic measurements should be treated in relativistic settings. With the implementation of the 1.5 PN equations of motion, needed to determine the BH spin, the latter topic becomes of fundamental importance and must be addressed in the incoming future in order to find a common strategy and consistent results [292, 297].

Still remaining in the context of stellar motion, the setup developed in this thesis can be easily extended to test different DM models, especially when the issues mentioned above will be solved and a full GR setup can be considered. Illustrative examples are BHs immersed in a DM halos [376, 377] or BHs in a DM spike [378].

Besides the follow-up of stellar motions, GRAVITY+'s key science case is to track the motion of hot gas in the immediate vicinity of the BH event horizon, the so-called flares of radiation at the GC [115, 120]. Being so close to the SMBH, hot spots might also be used as probes of strong gravity features, in particular light bending, i.e., the extreme gravitational lensing effects that lead to the existence of an infinite sequence of mirror images of an orbiting hot spot. These multiple images have a tiny impact on the observables, and only the secondary image might be potentially detectable.

In this context, it would be interesting to study the observable impact of the secondary image of GC flares, using three observables:

the astrometry, the light curve and the linear polarization evolution. The importance of observing secondary images resides in the fact that they carry important information about the BH geometry, specifically on the inclination angle of the BH axis and the magnitude of its spin. It would be extremely exciting, albeit not easy at all, to detect secondary images and combine observations at event horizon scales and stellar motion scales in order to obtain an estimate on SgrA* spin, in the same way it has been done for its mass and distance from Earth.

Overall, the development of pioneering experiments such as GRAVITY+ and the new generation EHT, together with advanced GWs interferometry, will create the perfect experimental array to tackle the current problems in the theory of gravity and understand a little more on what nowadays still remains *dark*.

Part III

APPENDIX

A

GEODESICS IN MAJUMDAR-PAPAPETROU SPACETIMES

There is a solution known in closed form, describing a regular and asymptotically flat BH binary spacetime geometry: it is known as the Majumdar-Papapetrou geometry and describes a pair (or more) of charged, extremal BHs. The BHs feel no force as they are extremal: their gravitational attraction is exactly canceled by an electrostatic repulsion. In isotropic cylindrical coordinates the geometry reads

$$ds^2 = -\frac{1}{U^2}dt^2 + U^2\left(d\rho^2 + \rho^2 d\phi^2 + dz^2\right) \,, \tag{A.1}$$

where

$$U = 1 + \frac{m_1}{\sqrt{\rho^2 + (z+a)^2}} + \frac{m_2}{\sqrt{\rho^2 + (z-a)^2}} \,. \tag{A.2}$$

Studies similar to that in the main body of this work were done in the context of such a spacetime [226–228]. Following their analysis, we find the following corrections for the ISCO frequency of an extremal BH of mass M perturbed by a companion of mass M_c at a distance $R = 2a$

$$M\Omega_{\rm ISCO} = \frac{\sqrt{3}}{16}\left(1 - \frac{M_c}{2R}\right) \,, \tag{A.3}$$

$$M\Omega_{\rm LR} = \frac{1}{4}\left(1 - \frac{M_c}{2R}\right) \,. \tag{A.4}$$

These results have no approximation other than assuming a large separation R. As one can see, the correction to the ISCO or LR frequency has a scaling with ϵ (or equivalently, with distance R) different from that found in Chap. 3 for neutral binaries. The disagreement can be traced back to the monopolar and dipolar components, and indirectly to the fact that this is not a purely gravitational system.

To see this, perform a translation of the z coordinate, $z \to z' - a$ and change from (ρ, z') coordinates to the usual spheroidal coordinates $(r_{\rm iso}, \theta)$, to find

$$U = 1 + \frac{m_1}{r_{\rm iso}} + \frac{m_2}{|\mathbf{r}_{\rm iso} - 2\mathbf{a}|} \,. \tag{A.5}$$

Use the same Laplace expansion in (3.13) to expand the second term, but now neglect the monopole $\ell = 0$ and the dipole $\ell = 1$ terms, finding

$$U = 1 + \frac{m_1}{r_{\text{iso}}} + \frac{m_2}{(2a)^3} r_{\text{iso}}^2 Y_{\ell m}^*(\theta_2, \phi_2) Y_{\ell m}(\theta, \phi)\,, \tag{A.6}$$

where again (θ_2, ϕ_2) are the angular coordinates of the second mass m_2 in the new reference frame. We now want to express the metric in the new coordinates using the relations $\rho \to (r - m_1)\cos\theta$ and $z \to (r - m_1)\sin\theta$, where r is the non-isotropic coordinate $r_{\text{iso}} = r - m_1$. To make contact with the approach in Chap. 3, set $\ell = 2$ in the harmonic expansion, fix the equatorial plane $\theta = \pi/2$ and specify the angular coordinates of m_2, which correspond to the polar case $(\theta_2, \phi_2) = (0, 0)$. Assume large separations, $a \gg 1$, and expand the metric in powers of $(1/a)$ up to $\mathcal{O}(1/a^4)$. We then find the leading correction

$$m_1 \Omega_{\text{ISCO}} = \frac{\sqrt{3}}{16}\left(1 + \frac{m_2}{R^3}\right)\,, \tag{A.7}$$

which is now in perfect agreement (scaling-wise) with the main body, for neutral binaries. In conclusion, the Majumdar-Papapetrou spacetime does affect the geodesics in a different way, which can be ascribed to the spacetime not describing two BHs bound and evolving solely under the gravitational interaction.

B

LIGHT RING RELAXATION PROPERTIES

To derive Eq. (3.41) let's focus on the Schwarzschild geometry written in standard coordinates,

$$ds^2 = -f dt^2 + f^{-1} dr^2 + r^2(d\theta^2 + \sin^2\theta d\varphi^2) \tag{B.1}$$

with $f = 1 - 2M/r$.

Take a null particle on the circular orbit at $r = r_c = 3M$ and perturb it, so that $r = 3M + \delta$. The motion of the particle is controlled by $\dot{r}^2 = V$. Expanding the potential close to the LR, one finds

$$\dot{\delta}^2 = V(r_c) + V'(r - r_c) + \frac{(r - r_c)^2}{2} V'' + ... \tag{B.2}$$

where the prime represents a derivative with respect to the radial coordinate. By definition of circular orbit, the first two terms vanish. Thus, one gets

$$\dot{\delta}^2 = \frac{\delta^2}{2} V'' . \tag{B.3}$$

Now $d\delta/d\tau = \dot{t} d\delta/dt$, therefore one can write

$$\frac{d\delta/dt}{\delta} = \left(\frac{V''}{2\dot{t}^2}\right)^{1/2} , \tag{B.4}$$

which has solution

$$\delta \sim \delta_0 e^{\lambda_L t} , \tag{B.5}$$

$$\lambda_L = \left(\frac{V''}{2\dot{t}^2}\right)^{1/2} . \tag{B.6}$$

where λ_L is exactly the Lyapunov exponent in Eq. (3.41) and for Schwarzschild spacetime it reads $\lambda_L = 1/3\sqrt{3}M = \Omega_{\rm LR}$.

C

AN ISOTROPICALLY-EMITTING STAR

In this Appendix we provide some details on the calculation of the emission of isotropic stars reported in Chap. 4. In order to so so, one needs to describe the physics as seen by a freely-falling observer. The following builds on - and agrees with - Refs. [1, 379, 380].

Let consider two different observers: a static observer, i.e., characterised by a wordline with $r = \theta = \varphi =$ const. and a free-falling observer, who starts from rest at spatial infinity and has a purely radial motion.

Start first with an observer at rest on the equatorial axis ($\{r, \theta, \varphi\} = \{r_e, \pi/2, \text{arbitrary}\}$) in a proper reference frame with basis

$$\omega^{\hat{t}} = e^{\nu} dt\,, \quad \omega^{\hat{r}} = e^{-\nu} dr\,, \quad \omega^{\hat{\varphi}} = r d\varphi\,. \tag{C.1}$$

If one considers a photon emitted by a source at rest at infinity and received by the observer, its geodesic motion is fully determined by its energy E and its impact parameter b. The components of the photon's four momentum read:

$$\begin{aligned} p_t &= -e^{2\nu}\dot{t} = -E\,, \quad p_\varphi = r^2\dot{\varphi} = L \equiv bE\,, \\ p_r &= e^{-2\nu}\dot{r} = A\, e^{-2\nu} E\,, \quad A^2 \equiv 1 - b^2 r^{-2} e^{2\nu}\,, \end{aligned} \tag{C.2}$$

We must now compute the $p^{\hat{t}}$ component of the momentum in the observer's reference frame. From Eq. (C.1) one gets

$$dt = e^{-\nu}\omega^{\hat{t}}\,, \quad dr = e^{\nu}\omega^{\hat{r}}\,, \quad d\varphi = r^{-1}\omega^{\hat{\varphi}}\,, \tag{C.3}$$

and hence

$$p^{\hat{t}} = -e^{-\nu} p_t\,, \quad p^{\hat{r}} = e^{\nu} p_r = A\, E\, e^{-\nu}\,. \tag{C.4}$$

The ratio of observed to emitted energy is then

$$\frac{p^{\hat{t}}}{E} = e^{-\nu}\,. \tag{C.5}$$

Moreover, the observer sees the null rays come in at an angle α relative to its radial direction given by

$$\cos\alpha = -\frac{p^{\hat{r}}}{p^{\hat{t}}} = -A\,. \tag{C.6}$$

Here, α is the angle between the propagation direction and the radial direction and it is defined as $\cos\alpha = v_{\hat{r}}$, where $v_{\hat{r}}$ is the velocity of the massless particle relative to the observer's reference frame,

$$v_{\hat{r}} = \frac{|g_{rr}|^{1/2} dr/d\lambda}{|g_{00}|^{1/2} dt/d\lambda} . \tag{C.7}$$

Consider now free-falling observers. The basis one-forms of their proper reference frame are

$$\omega^{\hat{t}} = dt + xe^{-2\nu} dr , \quad \omega^{\hat{r}} = xdt + e^{-2\nu} dr , \tag{C.8}$$

with $x = (2m/r_e)^{1/2}$. When a photon with energy at infinity E_o and impact parameter b reaches the observer at $r = r_e$ and $\theta = \pi/2$, its four momentum is given by (C.2). On the other hand, infalling observers will see the photon comes in with an energy $p^{\hat{t}} = \omega^{\hat{t}} \cdot \mathbf{p}$ and an angle $\alpha = \cos^{-1}(-p^{\hat{r}}/p^{\hat{t}})$ to the radial direction. As before, using (C.8) we get

$$dt = \frac{-\omega^{\hat{t}} + \omega^{\hat{r}} x}{x^2 - 1} , \quad dr = \frac{e^{2\nu}(-\omega^{\hat{r}} + \omega^{\hat{t}} x)}{x^2 - 1} . \tag{C.9}$$

Hence, we recover the results of Ref. [379]

$$\cos\alpha = -\left(\frac{p^{\hat{r}}}{p^{\hat{t}}}\right) = -\frac{x + a}{1 + ax} , \tag{C.10}$$

$$\frac{p^{\hat{t}}}{E} = -\frac{1 + ax}{x^2 - 1} = \frac{1}{1 + x\cos\alpha} , \tag{C.11}$$

$$\frac{b}{r_e} = \sin\alpha\, e^{-\nu} = \sin\alpha \left(\frac{p^{\hat{t}}}{E}\right) = \frac{\sin\alpha}{1 + x\cos\alpha} . \tag{C.12}$$

D

CORNER PLOTS

In this Appendix the correlations between the fitted parameters reported in (5.19) together with the fractional mass Λ, are shown using corner plots, namely the one and two-dimensional projections of the samples collected with EMCEE that reveal the covariances between parameters.

D.1 SCALAR CLOUD CASE

The corner plots for two representative values of α ($\alpha = 0.01$ and $\alpha = 0.001$) are shown in Figures D.1-D.2 for the scalar cloud case in Sec. 6.2. Those plots show the behaviour of the parameters when the cloud is located in and outside S2's orbital range, respectively.

The strong correlation between Λ and the periastron passage t_p when $\alpha = 0.01$ can be understood following the argument of Heißel et al. [170]: the presence of an extended mass will induce a retrograde precession in the orbit that will result in a positive shift of the periastron passage time, needed to compensate the (negative) shift in the initial true anomaly. Indeed, when considering the SP, which instead induces a prograde precession (hence a positive initial shift in the true anomaly), t_p will undergo a negative shift, as can be seen from the strong anti-correlation between $f_{\rm SP}$ and t_p reported in Ref. [166].

D.2 VECTOR CLOUD CASE

The corner plots for two representative values of α ($\alpha = 0.01$ and $\alpha = 0.001$) are shown in Figures D.3-D.4 for the vector cloud case in Sec. 6.3. Those plots show the behaviour of the parameters when the cloud is located in and outside S2's orbital range, respectively.

Considerations on correlations between parameters of the previous section apply to this case as well.

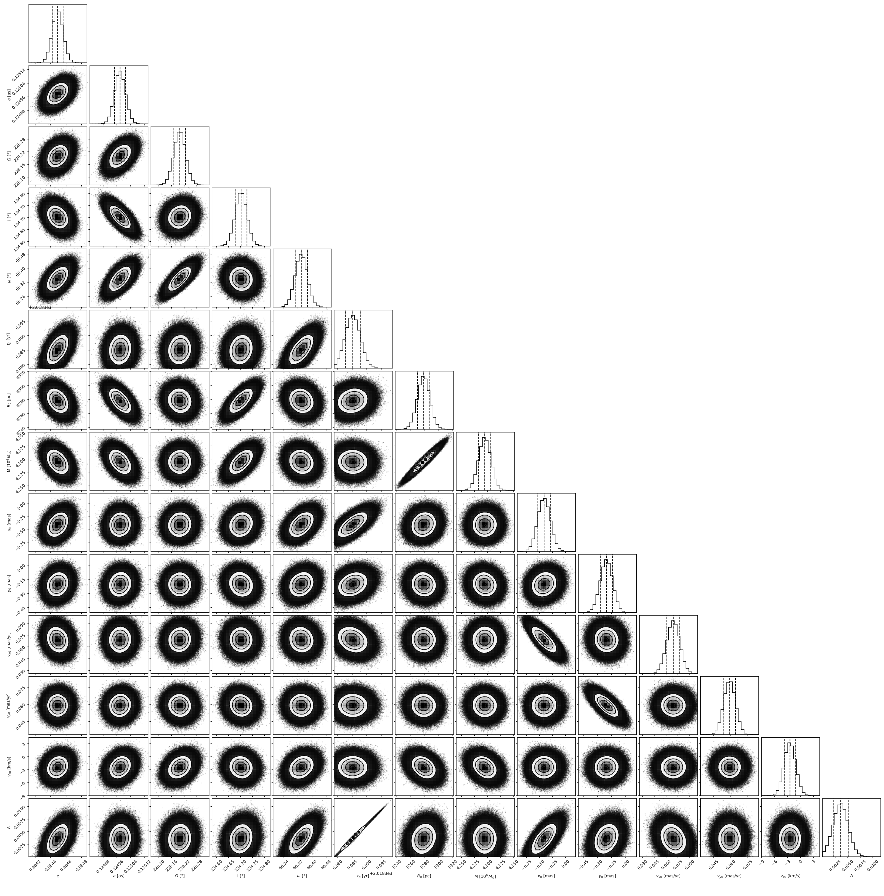

Figure D.1: Corner plot of the fitted parameters with $f_{\mathrm{SP}} = 1$ and $\alpha = 0.01$ when a scalar cloud is present. Dashed lines represent the 0.16, 0.50 and 0.84 quantiles of the distributions.

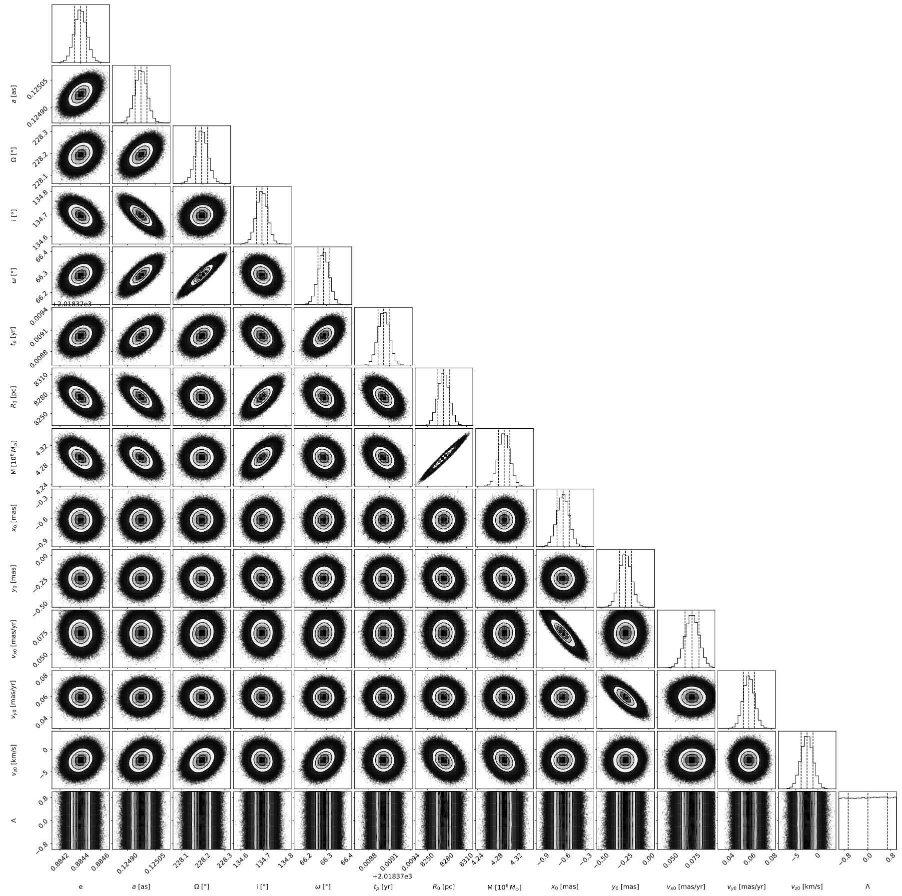

Figure D.2: Corner plot of the fitted parameters with $f_{\text{SP}} = 1$ and $\alpha = 0.001$ when a scalar cloud is present. Dashed lines represent the 0.16, 0.50 and 0.84 quantiles of the distributions.

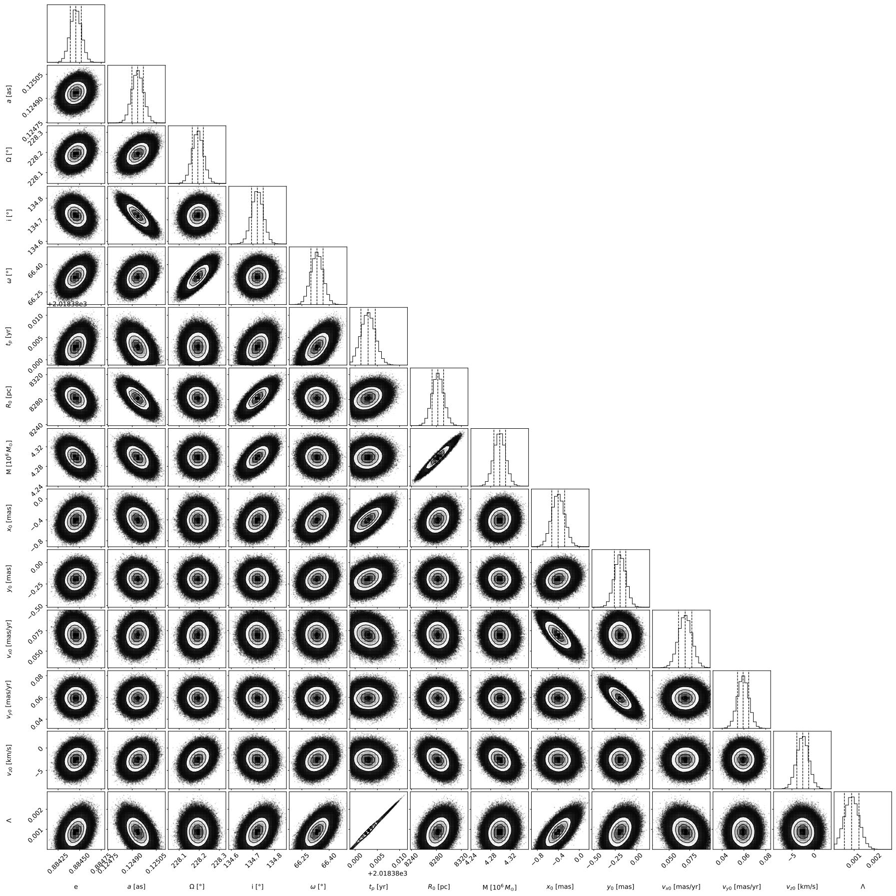

Figure D.3: Corner plot of the fitted parameters with $f_{\mathrm{SP}} = 1$ and $\alpha = 0.01$ when a vector cloud is present. Dashed lines represent the 0.16, 0.50 and 0.84 quantiles of the distributions.

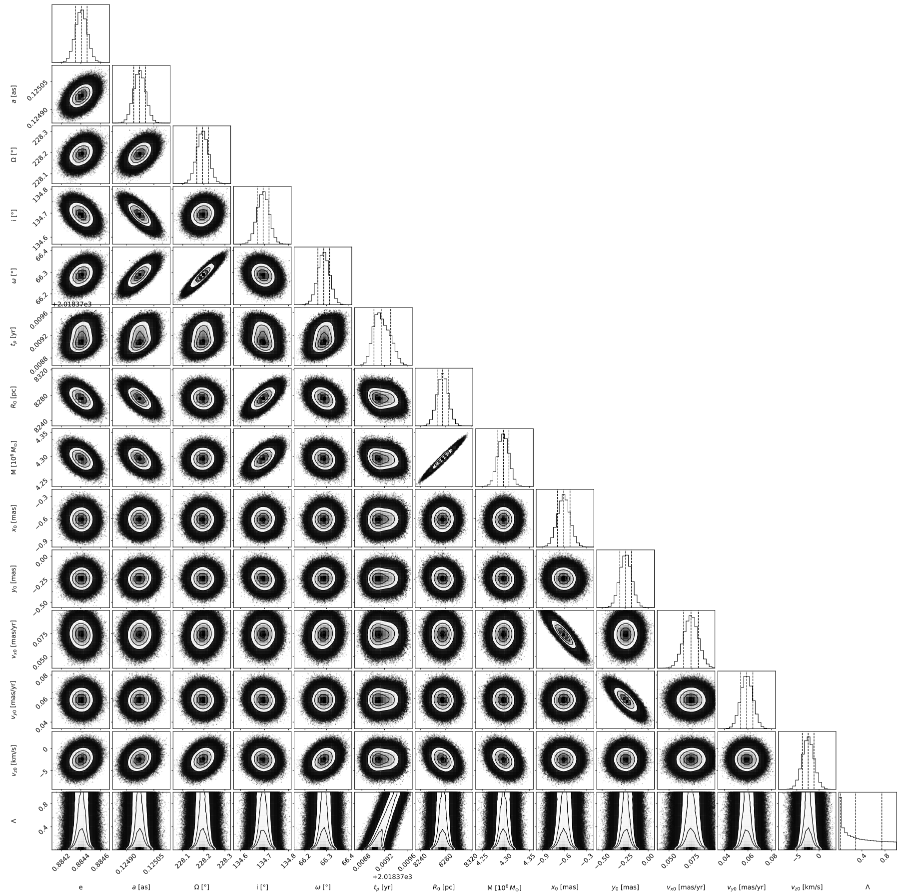

Figure D.4: Corner plot of the fitted parameters with $f_{\mathrm{SP}} = 1$ and $\alpha = 0.001$ when a vector cloud is present. Dashed lines represent the 0.16, 0.50 and 0.84 quantiles of the distributions.

BIBLIOGRAPHY

[1] Charles W. Misner, K. S. Thorne, and J. A. Wheeler. *Gravitation*. San Francisco: W. H. Freeman, 1973. ISBN: 978-0-7167-0344-0, 978-0-691-17779-3.

[2] Robert M. Wald. *General Relativity*. Chicago, USA: Chicago Univ. Pr., 1984. DOI: 10.7208/chicago/9780226870373.001.0001.

[3] R. Giacconi et al. "Discovery of Periodic X-Ray Pulsations in Centaurus X-3 from UHURU." In: 167 (July 1971), p. L67. DOI: 10.1086/180762.

[4] B. P. Abbott et al. "Observation of Gravitational Waves from a Binary Black Hole Merger." In: *Phys. Rev. Lett.* 116.6 (2016), p. 061102. DOI: 10.1103/PhysRevLett.116.061102. arXiv: 1602.03837 [gr-qc].

[5] Werner Israel. "Event horizons in static vacuum space-times." In: *Phys. Rev.* 164 (1967), pp. 1776–1779. DOI: 10.1103/PhysRev.164.1776.

[6] B. Carter. "Axisymmetric Black Hole Has Only Two Degrees of Freedom." In: *Phys. Rev. Lett.* 26 (1971), pp. 331–333. DOI: 10.1103/PhysRevLett.26.331.

[7] Remo Ruffini and John A. Wheeler. "Introducing the black hole." In: *Phys. Today* 24.1 (1971), p. 30. DOI: 10.1063/1.3022513.

[8] Werner Israel. "Event horizons in static electrovac space-times." In: *Commun. Math. Phys.* 8 (1968), pp. 245–260. DOI: 10.1007/BF01645859.

[9] Robert M. Wald. "Final States of Gravitational Collapse." In: *Phys. Rev. Lett.* 26 (26 1971), pp. 1653–1655. DOI: 10.1103/PhysRevLett.26.1653. URL: https://link.aps.org/doi/10.1103/PhysRevLett.26.1653.

[10] R. Abbott et al. "GWTC-3: Compact Binary Coalescences Observed by LIGO and Virgo During the Second Part of the Third Observing Run." In: (Nov. 2021). arXiv: 2111.03606 [gr-qc].

[11] R. Abbott et al. "GW190814: Gravitational Waves from the Coalescence of a 23 Solar Mass Black Hole with a 2.6 Solar Mass Compact Object." In: *Astrophys. J. Lett.* 896.2 (2020), p. L44. DOI: 10.3847/2041-8213/ab960f. arXiv: 2006.12611 [astro-ph.HE].

[12] M. Bailes et al. “Gravitational-wave physics and astronomy in the 2020s and 2030s.” In: *Nature Rev. Phys.* 3.5 (2021), pp. 344–366. DOI: `10.1038/s42254-021-00303-8`.

[13] Avery E. Broderick et al. “Testing the No-Hair Theorem with Event Horizon Telescope Observations of Sagittarius A*.” In: *Astrophys. J.* 784 (2014), p. 7. DOI: `10.1088/0004-637X/784/1/7`. arXiv: `1311.5564 [astro-ph.HE]`.

[14] Tim Johannsen et al. “Testing General Relativity with Accretion-Flow Imaging of Sgr A*.” In: *Phys. Rev. Lett.* 117.9 (2016), p. 091101. DOI: `10.1103/PhysRevLett.117.091101`. arXiv: `1608.03593 [astro-ph.HE]`.

[15] Kazunori Akiyama et al. “First M87 Event Horizon Telescope Results. I. The Shadow of the Supermassive Black Hole.” In: *Astrophys. J. Lett.* 875 (2019), p. L1. DOI: `10.3847/2041-8213/ab0ec7`. arXiv: `1906.11238 [astro-ph.GA]`.

[16] Kazunori Akiyama et al. “First M87 Event Horizon Telescope Results. II. Array and Instrumentation.” In: *Astrophys. J. Lett.* 875.1 (2019), p. L2. DOI: `10.3847/2041-8213/ab0c96`. arXiv: `1906.11239 [astro-ph.IM]`.

[17] Kazunori Akiyama et al. “First M87 Event Horizon Telescope Results. III. Data Processing and Calibration.” In: *Astrophys. J. Lett.* 875.1 (2019), p. L3. DOI: `10.3847/2041-8213/ab0c57`. arXiv: `1906.11240 [astro-ph.GA]`.

[18] Kazunori Akiyama et al. “First M87 Event Horizon Telescope Results. IV. Imaging the Central Supermassive Black Hole.” In: *Astrophys. J. Lett.* 875.1 (2019), p. L4. DOI: `10.3847/2041-8213/ab0e85`. arXiv: `1906.11241 [astro-ph.GA]`.

[19] Kazunori Akiyama et al. “First M87 Event Horizon Telescope Results. V. Physical Origin of the Asymmetric Ring.” In: *Astrophys. J. Lett.* 875.1 (2019), p. L5. DOI: `10.3847/2041-8213/ab0f43`. arXiv: `1906.11242 [astro-ph.GA]`.

[20] Kazunori Akiyama et al. “First M87 Event Horizon Telescope Results. VI. The Shadow and Mass of the Central Black Hole.” In: *Astrophys. J. Lett.* 875.1 (2019), p. L6. DOI: `10.3847/2041-8213/ab1141`. arXiv: `1906.11243 [astro-ph.GA]`.

[21] Kazunori Akiyama et al. “First Sagittarius A* Event Horizon Telescope Results. I. The Shadow of the Supermassive Black Hole in the Center of the Milky Way.” In: *Astrophys. J. Lett.* 930.2 (2022), p. L12. DOI: `10.3847/2041-8213/ac6674`.

[22] Kazunori Akiyama et al. “First Sagittarius A* Event Horizon Telescope Results. II. EHT and Multiwavelength Observations, Data Processing, and Calibration.” In: *Astrophys. J. Lett.* 930.2 (2022), p. L13. DOI: `10.3847/2041-8213/ac6675`.

[23] Kazunori Akiyama et al. "First Sagittarius A* Event Horizon Telescope Results. III. Imaging of the Galactic Center Supermassive Black Hole." In: *Astrophys. J. Lett.* 930.2 (2022), p. L14. DOI: 10.3847/2041-8213/ac6429.

[24] Kazunori Akiyama et al. "First Sagittarius A* Event Horizon Telescope Results. IV. Variability, Morphology, and Black Hole Mass." In: *Astrophys. J. Lett.* 930.2 (2022), p. L15. DOI: 10.3847/2041-8213/ac6736.

[25] Kazunori Akiyama et al. "First Sagittarius A* Event Horizon Telescope Results. V. Testing Astrophysical Models of the Galactic Center Black Hole." In: *Astrophys. J. Lett.* 930.2 (2022), p. L16. DOI: 10.3847/2041-8213/ac6672.

[26] Kazunori Akiyama et al. "First Sagittarius A* Event Horizon Telescope Results. VI. Testing the Black Hole Metric." In: *Astrophys. J. Lett.* 930.2 (2022), p. L17. DOI: 10.3847/2041-8213/ac6756.

[27] Reinhard Genzel. "Nobel Lecture: A forty-year journey." In: *Rev. Mod. Phys.* 94 (2 June 2022), p. 020501. DOI: 10.1103/RevModPhys.94.020501. URL: https://link.aps.org/doi/10.1103/RevModPhys.94.020501.

[28] Clifford M. Will. "The Confrontation between General Relativity and Experiment." In: *Living Rev. Rel.* 17 (2014), p. 4. DOI: 10.12942/lrr-2014-4. arXiv: 1403.7377 [gr-qc].

[29] Baron Kelvin Thomson William. *Baltimore Lectures on Molecular Dynamics and the Wave Theory of Light*. May 2010. ISBN: 978-0-511-69452-3. DOI: 10.1017/cbo9780511694523.

[30] F. Zwicky. "Republication of: The redshift of extragalactic nebulae." In: *General Relativity and Gravitation* 41.1 (Jan. 2009), pp. 207–224. DOI: 10.1007/s10714-008-0707-4.

[31] K. C. Freeman. "On the Disks of Spiral and S0 Galaxies." In: 160 (June 1970), p. 811. DOI: 10.1086/150474.

[32] V. C. Rubin, Jr. Ford W. K., and N. Thonnard. "Rotational properties of 21 SC galaxies with a large range of luminosities and radii, from NGC 4605 (R=4kpc) to UGC 2885 (R=122kpc)." In: 238 (June 1980), pp. 471–487. DOI: 10.1086/158003.

[33] Mordehai Milgrom. "The MOND paradigm." In: (Jan. 2008). arXiv: 0801.3133 [astro-ph].

[34] Julio F. Navarro, Carlos S. Frenk, and Simon D. M. White. "The Structure of cold dark matter halos." In: *Astrophys. J.* 462 (1996), pp. 563–575. DOI: 10.1086/177173. arXiv: astro-ph/9508025.

[35] Risa H. Wechsler and Jeremy L. Tinker. "The Connection between Galaxies and their Dark Matter Halos." In: *Ann. Rev. Astron. Astrophys.* 56 (2018), pp. 435–487. DOI: `10.1146/annurev-astro-081817-051756`. arXiv: `1804.03097 [astro-ph.GA]`.

[36] Xiang-Ping Wu et al. "A comparison of different cluster mass estimates: consistency or discrepancy ?" In: *Mon. Not. Roy. Astron. Soc.* 301 (1998), p. 861. DOI: `10.1046/j.1365-8711.1998.02055.x`. arXiv: `astro-ph/9808179`.

[37] Richard Massey, Thomas Kitching, and Johan Richard. "The dark matter of gravitational lensing." In: *Rept. Prog. Phys.* 73 (2010), p. 086901. DOI: `10.1088/0034-4885/73/8/086901`. arXiv: `1001.1739 [astro-ph.CO]`.

[38] Maxim Markevitch et al. "Direct constraints on the dark matter self-interaction cross-section from the merging galaxy cluster 1E0657-56." In: *Astrophys. J.* 606 (2004), pp. 819–824. DOI: `10.1086/383178`. arXiv: `astro-ph/0309303`.

[39] Douglas Clowe et al. "A direct empirical proof of the existence of dark matter." In: *Astrophys. J. Lett.* 648 (2006), pp. L109–L113. DOI: `10.1086/508162`. arXiv: `astro-ph/0608407`.

[40] Giuseppina Battaglia et al. "The Radial velocity dispersion profile of the Galactic Halo: Constraining the density profile of the dark halo of the Milky Way." In: *Mon. Not. Roy. Astron. Soc.* 364 (2005). [Erratum: Mon.Not.Roy.Astron.Soc. 370, 1055 (2006)], pp. 433–442. DOI: `10.1111/j.1365-2966.2005.09367.x`. arXiv: `astro-ph/0506102`.

[41] Prajwal Raj Kafle et al. "On the Shoulders of Giants: Properties of the Stellar Halo and the Milky Way Mass Distribution." In: *Astrophys. J.* 794.1 (2014), p. 59. DOI: `10.1088/0004-637X/794/1/59`. arXiv: `1408.1787 [astro-ph.GA]`.

[42] Paul J. McMillan. "The mass distribution and gravitational potential of the Milky Way." In: 465.1 (Feb. 2017), pp. 76–94. DOI: `10.1093/mnras/stw2759`. arXiv: `1608.00971 [astro-ph.GA]`.

[43] Francesco Sylos Labini et al. "Mass Models of the Milky Way and Estimation of Its Mass from the Gaia DR3 Data Set." In: 945.1, 3 (Mar. 2023), p. 3. DOI: `10.3847/1538-4357/acb92c`. arXiv: `2302.01379 [astro-ph.GA]`.

[44] Yoshiaki Sofue. "Rotation Curve of the Milky Way and the Dark Matter Density." In: *Galaxies* 8.2 (Apr. 2020), p. 37. DOI: `10.3390/galaxies8020037`. arXiv: `2004.11688 [astro-ph.GA]`.

[45] Yongjun Jiao et al. "Detection of the Keplerian decline in the Milky Way rotation curve." In: *Astron. Astrophys.* 678 (2023), A208. DOI: `10.1051/0004-6361/202347513`. arXiv: `2309.00048 [astro-ph.GA]`.

[46] B. J. Carr and S. W. Hawking. "Black holes in the early Universe." In: 168 (Aug. 1974), pp. 399–416. DOI: `10.1093/mnras/168.2.399`.

[47] B. J. Carr et al. "New cosmological constraints on primordial black holes." In: *Phys. Rev. D* 81 (2010), p. 104019. DOI: `10.1103/PhysRevD.81.104019`. arXiv: `0912.5297 [astro-ph.CO]`.

[48] R. D. Peccei and Helen R. Quinn. "CP Conservation in the Presence of Instantons." In: *Phys. Rev. Lett.* 38 (1977), pp. 1440–1443. DOI: `10.1103/PhysRevLett.38.1440`.

[49] Asimina Arvanitaki et al. "String Axiverse." In: *Phys. Rev. D* 81 (2010), p. 123530. DOI: `10.1103/PhysRevD.81.123530`. arXiv: `0905.4720 [hep-th]`.

[50] R. L. Workman et al. "Review of Particle Physics." In: *PTEP* 2022 (2022), p. 083C01. DOI: `10.1093/ptep/ptac097`.

[51] Joshua Frieman, Michael Turner, and Dragan Huterer. "Dark Energy and the Accelerating Universe." In: *Ann. Rev. Astron. Astrophys.* 46 (2008), pp. 385–432. DOI: `10.1146/annurev.astro.46.060407.145243`. arXiv: `0803.0982 [astro-ph]`.

[52] John Dubinski and R. G. Carlberg. "The Structure of cold dark matter halos." In: *Astrophys. J.* 378 (1991), p. 496. DOI: `10.1086/170451`.

[53] Wayne Hu, Rennan Barkana, and Andrei Gruzinov. "Cold and fuzzy dark matter." In: *Phys. Rev. Lett.* 85 (2000), pp. 1158–1161. DOI: `10.1103/PhysRevLett.85.1158`. arXiv: `astro-ph/0003365`.

[54] David N. Spergel and Paul J. Steinhardt. "Observational evidence for selfinteracting cold dark matter." In: *Phys. Rev. Lett.* 84 (2000), pp. 3760–3763. DOI: `10.1103/PhysRevLett.84.3760`. arXiv: `astro-ph/9909386`.

[55] Manoj Kaplinghat, Lloyd Knox, and Michael S. Turner. "Annihilating the cold dark matter cusp crisis." In: *Phys. Rev. Lett.* 85 (2000), p. 3335. DOI: `10.1103/PhysRevLett.85.3335`. arXiv: `astro-ph/0005210`.

[56] Antonino Del Popolo and Morgan Le Delliou. "Review of Solutions to the Cusp-Core Problem of the ΛCDM Model." In: *Galaxies* 9.4 (2021), p. 123. DOI: `10.3390/galaxies9040123`. arXiv: `2209.14151 [astro-ph.CO]`.

[57] Asimina Arvanitaki and Sergei Dubovsky. "Exploring the String Axiverse with Precision Black Hole Physics." In: *Phys. Rev. D* 83 (2011), p. 044026. DOI: `10.1103/PhysRevD.83.044026`. arXiv: `1004.3558 [hep-th]`.

[58] David J. E. Marsh. "Axion Cosmology." In: *Phys. Rept.* 643 (2016), pp. 1–79. DOI: `10.1016/j.physrep.2016.06.005`. arXiv: `1510.07633 [astro-ph.CO]`.

[59] Mark Goodsell et al. "Naturally Light Hidden Photons in LARGE Volume String Compactifications." In: *JHEP* 11 (2009), p. 027. DOI: `10.1088/1126-6708/2009/11/027`. arXiv: `0909.0515 [hep-ph]`.

[60] Joerg Jaeckel and Andreas Ringwald. "The Low-Energy Frontier of Particle Physics." In: *Ann. Rev. Nucl. Part. Sci.* 60 (2010), pp. 405–437. DOI: `10.1146/annurev.nucl.012809.104433`. arXiv: `1002.0329 [hep-ph]`.

[61] Hooman Davoudiasl and Peter B Denton. "Ultralight Boson Dark Matter and Event Horizon Telescope Observations of M87*." In: *Phys. Rev. Lett.* 123.2 (2019), p. 021102. DOI: `10.1103/PhysRevLett.123.021102`. arXiv: `1904.09242 [astro-ph.CO]`.

[62] Nitsan Bar et al. "Galactic rotation curves versus ultralight dark matter: Implications of the soliton-host halo relation." In: *Phys. Rev. D* 98.8 (2018), p. 083027. DOI: `10.1103/PhysRevD.98.083027`. arXiv: `1805.00122 [astro-ph.CO]`.

[63] Nitsan Bar et al. "Ultralight dark matter in disk galaxies." In: *Phys. Rev. D* 99.10 (2019), p. 103020. DOI: `10.1103/PhysRevD.99.103020`. arXiv: `1903.03402 [astro-ph.CO]`.

[64] Eric Armengaud et al. "Constraining the mass of light bosonic dark matter using SDSS Lyman-α forest." In: *Mon. Not. Roy. Astron. Soc.* 471.4 (2017), pp. 4606–4614. DOI: `10.1093/mnras/stx1870`. arXiv: `1703.09126 [astro-ph.CO]`.

[65] Vid Iršič et al. "First constraints on fuzzy dark matter from Lyman-α forest data and hydrodynamical simulations." In: *Phys. Rev. Lett.* 119.3 (2017), p. 031302. DOI: `10.1103/PhysRevLett.119.031302`. arXiv: `1703.04683 [astro-ph.CO]`.

[66] Jiajun Zhang et al. "The Importance of Quantum Pressure of Fuzzy Dark Matter on Lyman-Alpha Forest." In: *Astrophys. J.* 863 (2018), p. 73. DOI: `10.3847/1538-4357/aacf3f`. arXiv: `1708.04389 [astro-ph.CO]`.

[67] Takeshi Kobayashi et al. "Lyman-α constraints on ultralight scalar dark matter: Implications for the early and late universe." In: *Phys. Rev. D* 96.12 (2017), p. 123514. DOI: `10.1103/PhysRevD.96.123514`. arXiv: `1708.00015 [astro-ph.CO]`.

[68] Ka-Hou Leong et al. "Testing extreme-axion wave-like dark matter using the BOSS Lyman-alpha forest data." In: *Mon. Not. Roy. Astron. Soc.* 484.3 (2019), pp. 4273–4286. DOI: `10.1093/mnras/stz271`. arXiv: `1810.05930 [astro-ph.CO]`.

[69] Nataliya K. Porayko et al. “Parkes Pulsar Timing Array constraints on ultralight scalar-field dark matter.” In: *Phys. Rev. D* 98.10 (2018), p. 102002. DOI: `10.1103/PhysRevD.98.102002`. arXiv: `1810.03227 [astro-ph.CO]`.

[70] Andrei Khmelnitsky and Valery Rubakov. “Pulsar timing signal from ultralight scalar dark matter.” In: *JCAP* 02 (2014), p. 019. DOI: `10.1088/1475-7516/2014/02/019`. arXiv: `1309.5888 [astro-ph.CO]`.

[71] J. Antoniadis et al. “The second data release from the European Pulsar Timing Array I. The dataset and timing analysis.” In: (June 2023). DOI: `10.1051/0004-6361/202346841`. arXiv: `2306.16224 [astro-ph.HE]`.

[72] Clemente Smarra et al. “The second data release from the European Pulsar Timing Array: VI. Challenging the ultralight dark matter paradigm.” In: (June 2023). arXiv: `2306.16228 [astro-ph.HE]`.

[73] Naoya Kitajima et al. “Nanohertz Gravitational Waves from Axion Domain Walls Coupled to QCD.” In: (June 2023). arXiv: `2306.17146 [hep-ph]`.

[74] Aaron Bryant and Alfred Krabbe. “The episodic and multiscale Galactic Centre.” In: 93, 101630 (Dec. 2021), p. 101630. DOI: `10.1016/j.newar.2021.101630`.

[75] E. Mills et al. “Properties of the Compact H II Region Complex G-0.02-0.07.” In: 735.2, 84 (July 2011), p. 84. DOI: `10.1088/0004-637X/735/2/84`. arXiv: `1102.2533 [astro-ph.GA]`.

[76] F. K. Baganoff et al. “Rapid X-ray flaring from the direction of the supermassive black hole at the galactic centre.” In: *Nature* 413 (2001), pp. 45–48. DOI: `10.1038/35092510`. arXiv: `astro-ph/0109367`.

[77] Frederick K. Baganoff et al. “Chandra x-ray spectroscopic imaging of Sgr A* and the central parsec of the Galaxy.” In: *Astrophys. J.* 591 (2003), pp. 891–915. DOI: `10.1086/375145`. arXiv: `astro-ph/0102151`.

[78] Michael P. Muno et al. “Diffuse x-ray emission in a deep Chandra image of the Galactic center.” In: *Astrophys. J.* 613 (2004), pp. 326–342. DOI: `10.1086/422865`. arXiv: `astro-ph/0402087`.

[79] R. Schödel, D. Merritt, and A. Eckart. “The nuclear star cluster of the Milky Way: proper motions and mass.” In: 502.1 (July 2009), pp. 91–111. DOI: `10.1051/0004-6361/200810922`. arXiv: `0902.3892 [astro-ph.GA]`.

[80] Robert D. Blum et al. “Really cool stars and the star formation history at the Galactic Center.” In: *Astrophys. J.* 597 (2003), pp. 323–346. DOI: `10.1086/378380`. arXiv: `astro-ph/0307291`.

[81] W. J. Forrest et al. "Brackett alpha images of the Galactic center." In: *The Galactic Center*. Ed. by Donald C. Backer. Vol. 155. American Institute of Physics Conference Series. Apr. 1987, pp. 153–156. DOI: 10.1063/1.36414.

[82] David A. Allen, A. R. Hyland, and D. J. Hillier. "The source of luminosity at the Galactic Centre." In: 244 (June 1990), p. 706.

[83] A. Krabbe et al. "A Cluster of He i Emission-Line Stars in the Galactic Center." In: 382 (Nov. 1991), p. L19. DOI: 10.1086/186204.

[84] Peter Tamblyn and G. H. Rieke. "IRS 16: The Galaxy's Central Wimp?" In: 414 (Sept. 1993), p. 573. DOI: 10.1086/173104.

[85] R. Genzel et al. "The Dark Mass Concentration in the Central Parsec of the Milky Way." In: *Astrophys. J.* 472 (1996), p. 153. DOI: 10.1086/178051.

[86] R. D. Blum, K. Sellgren, and D. L. Depoy. "JHKL Photometry and the K-Band Luminosity Function at the Galactic Center." In: 470 (Oct. 1996), p. 864. DOI: 10.1086/177917. arXiv: astro-ph/9604109 [astro-ph].

[87] T. Paumard et al. "New results on the helium stars in the galactic center using BEAR spectro-imagery." In: 366 (Feb. 2001), pp. 466–480. DOI: 10.1051/0004-6361:20000227. arXiv: astro-ph/0011215 [astro-ph].

[88] Thibaut Paumard, Jean-Pierre Maillard, and Mark Morris. "Kinematic and structural analysis of the minispiral in the Galactic Center from BEAR spectro-imagery." In: *Astron. Astrophys.* 426 (2004), pp. 81–96. DOI: 10.1051/0004-6361:20034209. arXiv: astro-ph/0405197.

[89] T. Paumard et al. "The Two Young Star Disks in the Central Parsec of the Galaxy: Properties, Dynamics, and Formation." In: 643.2 (June 2006), pp. 1011–1035. DOI: 10.1086/503273. arXiv: astro-ph/0601268 [astro-ph].

[90] Angelle Tanner et al. "High Spectral Resolution Observations of the Massive Stars in the Galactic Center." In: 641.2 (Apr. 2006), pp. 891–904. DOI: 10.1086/500498. arXiv: astro-ph/0510028 [astro-ph].

[91] Reinhard Genzel, Frank Eisenhauer, and Stefan Gillessen. "The Galactic Center massive black hole and nuclear star cluster." In: *Reviews of Modern Physics* 82.4 (Oct. 2010), pp. 3121–3195. DOI: 10.1103/RevModPhys.82.3121. arXiv: 1006.0064 [astro-ph.GA].

[92] Mariafelicia De Laurentis, Ivan De Martino, and Riccardo Della Monica. "The Galactic Center as a laboratory for theories of gravity and dark matter." In: *arXiv e-prints*, arXiv:2211.07008 (Nov. 2022), arXiv:2211.07008. DOI: 10.48550/arXiv.2211.07008. arXiv: 2211.07008 [astro-ph.GA].

[93] A. M. Ghez et al. “The first measurement of spectral lines in a short - period star bound to the galaxy’s central black hole: A paradox of youth.” In: *Astrophys. J. Lett.* 586 (2003), pp. L127–L131. DOI: 10.1086/374804. arXiv: astro-ph/0302299.

[94] Pierre Salati and Joseph Silk. “A Stellar Probe of Dark Matter Annihilation in Galactic Nuclei.” In: 338 (Mar. 1989), p. 24. DOI: 10.1086/167177.

[95] Malcolm Fairbairn, Pat Scott, and Joakim Edsjo. “The Zero Age Main Sequence of WIMP burners.” In: *Phys. Rev. D* 77 (2008), p. 047301. DOI: 10.1103/PhysRevD.77.047301. arXiv: 0710.3396 [astro-ph].

[96] Pat Scott, Malcolm Fairbairn, and Joakim Edsjo. “Dark stars at the Galactic centre - the main sequence.” In: *Mon. Not. Roy. Astron. Soc.* 394 (2009), p. 82. DOI: 10.1111/j.1365-2966.2008.14282.x. arXiv: 0809.1871 [astro-ph].

[97] Jordi Casanellas and IlíDio Lopes. “The formation and evolution of young low-mass stars within halos with high concentration of dark matter particles.” In: *Astrophys. J.* 705 (2009), pp. 135–143. DOI: 10.1088/0004-637X/705/1/135. arXiv: 0909.1971 [astro-ph.CO].

[98] Andrew R. Zentner and Andrew P. Hearin. “Asymmetric Dark Matter May Alter the Evolution of Low-mass Stars and Brown Dwarfs.” In: *Phys. Rev. D* 84 (2011), p. 101302. DOI: 10.1103/PhysRevD.84.101302. arXiv: 1110.5919 [astro-ph.CO].

[99] André Martins, Ilídio Lopes, and Jordi Casanellas. “Asteroseismic constraints on asymmetric dark matter: Light particles with an effective spin-dependent coupling.” In: *Phys. Rev. D* 95.2 (2017), p. 023507. DOI: 10.1103/PhysRevD.95.023507. arXiv: 1701.03928 [astro-ph.SR].

[100] D. Lynden-Bell. “Galactic Nuclei as Collapsed Old Quasars.” In: *Nature* 223.5207 (Aug. 1969), pp. 690–694. DOI: 10.1038/223690a0.

[101] D. Lynden-Bell and M. J. Rees. “On quasars, dust and the galactic centre.” In: *Mon. Not. Roy. Astron. Soc.* 152 (Jan. 1971), p. 461. DOI: 10.1093/mnras/152.4.461.

[102] B. Balick and R. L. Brown. “Intense sub-arcsecond structure in the galactic center.” In: *APJ* 194 (Dec. 1974), pp. 265–270. DOI: 10.1086/153242.

[103] R. D. Ekers et al. “A full synthesis map of Sgr A at 5 GHz.” In: 43 (Oct. 1975), pp. 159–166.

[104] R. L. Brown and K. Y. Lo. “Variability of the compact radio source at the Galactic Center.” In: *APJ* 253 (Feb. 1982), pp. 108–114. DOI: 10.1086/159615.

[105] W. Miller Goss, Robert L. Brown, and K. Y. Lo. “The discovery of sgr a*.” In: (May 2003). DOI: 10.1002/asna.200385047. arXiv: astro-ph/0305074.

[106] M. K. Crawford et al. “Mass distribution in the galactic centre.” In: 315.6019 (June 1985), pp. 467–470. DOI: 10.1038/315467a0.

[107] E. Serabyn and J. H. Lacy. “NE II observations of the galactic center : evidence for a massive black hole.” In: 293 (June 1985), pp. 445–458. DOI: 10.1086/163250.

[108] R. Guesten et al. “Aperture Synthesis Observations of the Circumnuclear Ring in the Galactic Center.” In: 318 (July 1987), p. 124. DOI: 10.1086/165355.

[109] J. M. Jackson et al. “Neutral Gas in the Central 2 Parsecs of the Galaxy.” In: 402 (Jan. 1993), p. 173. DOI: 10.1086/172120.

[110] D. A. Roberts, F. Yusef-Zadeh, and W. M. Goss. “Kinematics of the Ionized Gas in Sagittarius A West: Mass Estimates of the Inner 0.13 Parsecs of the Galaxy.” In: 459 (Mar. 1996), p. 627. DOI: 10.1086/176927.

[111] Tim Johannsen and Dimitrios Psaltis. “Testing the No-hair Theorem with Observations in the Electromagnetic Spectrum. II. Black Hole Images.” In: 718.1 (July 2010), pp. 446–454. DOI: 10.1088/0004-637X/718/1/446. arXiv: 1005.1931 [astro-ph.HE].

[112] A. M. Ghez et al. “Variable infrared emission from the supermassive black hole at the center of the milky way.” In: *Astrophys. J. Lett.* 601 (2004), pp. L159–L162. DOI: 10.1086/382024. arXiv: astro-ph/0309076.

[113] A. Eckart et al. “First simultaneous NIR / x-ray detection of a flare from Sgr A*.” In: *Astron. Astrophys.* 427 (2004), pp. 1–11. DOI: 10.1051/0004-6361:20040495. arXiv: astro-ph/0403577.

[114] J. Neilsen et al. “A Chandra/HETGS Census of X-Ray Variability from Sgr A* during 2012.” In: *Astrophys. J.* 774 (2013), p. 42. DOI: 10.1088/0004-637X/774/1/42. arXiv: 1307.5843 [astro-ph.HE].

[115] GRAVITY Collaboration. “Detection of orbital motions near the last stable circular orbit of the massive black hole SgrA*.” In: 618 (Oct. 2018), p. L10. DOI: 10.1051/0004-6361/201834294. arXiv: 1810.12641 [astro-ph.GA].

[116] R. Abuter et al. “The flux distribution of Sgr A*.” In: *Astron. Astrophys.* 638 (2020), A2. DOI: 10.1051/0004-6361/202037717. arXiv: 2004.07185 [astro-ph.GA].

[117] N. Aimar et al. “Magnetic reconnection plasmoid model for Sagittarius A* flares.” In: *Astron. Astrophys.* 672 (2023), A62. DOI: 10.1051/0004-6361/202244936. arXiv: 2301.11874 [astro-ph.HE].

[118] Tatsuya Matsumoto, Chi-Ho Chan, and Tsvi Piran. "The origin of hotspots around Sgr A*: Orbital or pattern motion?" In: *Mon. Not. Roy. Astron. Soc.* 497.2 (2020), pp. 2385–2392. DOI: 10.1093/mnras/staa2095. arXiv: 2004.13029 [astro-ph.HE].

[119] Xi Lin, Ya-Ping Li, and Feng Yuan. "A 'coronal-mass-ejection' model for flares in Sagittarius A*." In: *Mon. Not. Roy. Astron. Soc.* 520.1 (2023), pp. 1271–1284. DOI: 10.1093/mnras/stad176. arXiv: 2301.05925 [astro-ph.HE].

[120] R. Abuter et al. "Polarimetry and Astrometry of NIR Flares as Event Horizon Scale, Dynamical Probes for the Mass of Sgr A*." In: *Astron. Astrophys.* 677 (2023), p. L10. DOI: 10.1051/0004-6361/202347416. arXiv: 2307.11821 [astro-ph.GA].

[121] R. Ruffini, C. R. Argüelles, and J. A. Rueda. "On the core-halo distribution of dark matter in galaxies." In: 451.1 (July 2015), pp. 622–628. DOI: 10.1093/mnras/stv1016. arXiv: 1409.7365 [astro-ph.GA].

[122] C. R. Argüelles et al. "Can fermionic dark matter mimic supermassive black holes?" In: *Int. J. Mod. Phys. D* 28.14 (2019), p. 1943003. DOI: 10.1142/S021827181943003X. arXiv: 1905.09776 [astro-ph.GA].

[123] E. A. Becerra-Vergara et al. "Geodesic motion of S2 and G2 as a test of the fermionic dark matter nature of our Galactic core." In: *Astron. Astrophys.* 641 (2020), A34. DOI: 10.1051/0004-6361/201935990. arXiv: 2007.11478 [astro-ph.GA].

[124] Vitor Cardoso and Paolo Pani. "Testing the nature of dark compact objects: a status report." In: *Living Rev. Rel.* 22.1 (2019), p. 4. DOI: 10.1007/s41114-019-0020-4. arXiv: 1904.05363 [gr-qc].

[125] M. S. Morris, K. S. Thorne, and U. Yurtsever. "Wormholes, Time Machines, and the Weak Energy Condition." In: *Phys. Rev. Lett.* 61 (1988), pp. 1446–1449. DOI: 10.1103/PhysRevLett.61.1446.

[126] Cosimo Bambi and Dejan Stojkovic. "Astrophysical Wormholes." In: *Universe* 7.5 (2021), p. 136. DOI: 10.3390/universe7050136. arXiv: 2105.00881 [gr-qc].

[127] De-Chang Dai and Dejan Stojkovic. "Observing a Wormhole." In: *Phys. Rev. D* 100.8 (2019), p. 083513. DOI: 10.1103/PhysRevD.100.083513. arXiv: 1910.00429 [gr-qc].

[128] John H. Simonetti et al. "Sensitive searches for wormholes." In: *Phys. Rev. D* 104.8 (2021), p. L081502. DOI: 10.1103/PhysRevD.104.L081502. arXiv: 2007.12184 [gr-qc].

[129] Alex Simpson and Matt Visser. "Black-bounce to traversable wormhole." In: *JCAP* 02 (2019), p. 042. DOI: 10.1088/1475-7516/2019/02/042. arXiv: 1812.07114 [gr-qc].

[130] Riccardo Della Monica and Ivan De Martino. "Unveiling the nature of SgrA* with the geodesic motion of S-stars." In: *JCAP* 03.03 (2022), p. 007. DOI: `10.1088/1475-7516/2022/03/007`. arXiv: `2112.01888 [astro-ph.GA]`.

[131] M. Cadoni et al. "Are nonsingular black holes with super-Planckian hair ruled out by S2 star data?" In: *Phys. Rev. D* 107.4 (2023), p. 044038. DOI: `10.1103/PhysRevD.107.044038`. arXiv: `2211.11585 [gr-qc]`.

[132] Pau Amaro-Seoane et al. "Constraining scalar fields with stellar kinematics and collisional dark matter." In: *JCAP* 11 (2010), p. 002. DOI: `10.1088/1475-7516/2010/11/002`. arXiv: `1009.0019 [astro-ph.CO]`.

[133] F. H. Vincent et al. "Imaging a boson star at the Galactic center." In: *Class. Quant. Grav.* 33.10 (2016), p. 105015. DOI: `10.1088/0264-9381/33/10/105015`. arXiv: `1510.04170 [gr-qc]`.

[134] S. Bonazzola and F. Pacini. "Equilibrium of a Large Assembly of Particles in General Relativity." In: *Phys. Rev.* 148 (1966), pp. 1269–1270. DOI: `10.1103/PhysRev.148.1269`.

[135] David A. Feinblum and William A. McKinley. "Stable States of a Scalar Particle in Its Own Gravational Field." In: *Phys. Rev.* 168.5 (1968), p. 1445. DOI: `10.1103/PhysRev.168.1445`.

[136] David J. Kaup. "Klein-Gordon Geon." In: *Phys. Rev.* 172 (1968), pp. 1331–1342. DOI: `10.1103/PhysRev.172.1331`.

[137] Remo Ruffini and Silvano Bonazzola. "Systems of selfgravitating particles in general relativity and the concept of an equation of state." In: *Phys. Rev.* 187 (1969), pp. 1767–1783. DOI: `10.1103/PhysRev.187.1767`.

[138] M. Grould et al. "Comparing timelike geodesics around a Kerr black hole and a boson star." In: *Class. Quant. Grav.* 34.21 (2017), p. 215007. DOI: `10.1088/1361-6382/aa8d39`. arXiv: `1709.05938 [astro-ph.HE]`.

[139] Pedro V. P. Cunha et al. "Lensing and dynamics of ultracompact bosonic stars." In: *Phys. Rev. D* 96.10 (2017), p. 104040. DOI: `10.1103/PhysRevD.96.104040`. arXiv: `1709.06118 [gr-qc]`.

[140] Hector Olivares et al. "How to tell an accreting boson star from a black hole." In: *Mon. Not. Roy. Astron. Soc.* 497.1 (2020), pp. 521–535. DOI: `10.1093/mnras/staa1878`. arXiv: `1809.08682 [gr-qc]`.

[141] F. H. Vincent et al. "Geometric modeling of M87* as a Kerr black hole or a non-Kerr compact object." In: *Astron. Astrophys.* 646 (2021), A37. DOI: `10.1051/0004-6361/202037787`. arXiv: `2002.09226 [gr-qc]`.

[142] R. Genzel et al. “Near-infrared flares from accreting gas around the supermassive black hole at the galactic centre.” In: *Nature* 425 (2003), pp. 934–937. DOI: 10.1038/nature02065. arXiv: astro-ph/0310821.

[143] Leonhard Meyer et al. “Near-infrared polarimetry setting constraints on the orbiting spot model for Sgr A* flares.” In: *Astron. Astrophys.* 460 (2006), p. 15. DOI: 10.1051/0004-6361:20065925. arXiv: astro-ph/0610104.

[144] Giacomo Fragione and Abraham Loeb. “An upper limit on the spin of SgrA* based on stellar orbits in its vicinity.” In: *Astrophys. J. Lett.* 901.2 (2020), p. L32. DOI: 10.3847/2041-8213/abb9b4. arXiv: 2008.11734 [astro-ph.GA].

[145] Ruth A. Daly et al. “New Black Hole Spin Values for Sagittarius A* Obtained with the Outflow Method.” In: (Oct. 2023). arXiv: 2310.12108 [astro-ph.GA].

[146] A. Eckart and R. Genzel. “Stellar proper motions in the central 0.1 PC of the galaxy.” In: *Mon. Not. Roy. Astron. Soc.* 284 (1997), pp. 576–598. DOI: 10.1093/mnras/284.3.576.

[147] A. M. Ghez et al. “High proper motion stars in the vicinity of Sgr A*: Evidence for a supermassive black hole at the center of our galaxy.” In: *Astrophys. J.* 509 (1998), pp. 678–686. DOI: 10.1086/306528. arXiv: astro-ph/9807210.

[148] Frank Eisenhauer et al. “SINFONI in the Galactic Center: Young stars and IR flares in the central light month.” In: *Astrophys. J.* 628 (2005), pp. 246–259. DOI: 10.1086/430667. arXiv: astro-ph/0502129.

[149] S. Gillessen et al. “Monitoring stellar orbits around the Massive Black Hole in the Galactic Center.” In: *Astrophys. J.* 692 (2009), pp. 1075–1109. DOI: 10.1088/0004-637X/692/2/1075. arXiv: 0810.4674 [astro-ph].

[150] S. Gillessen et al. “An Update on Monitoring Stellar Orbits in the Galactic Center.” In: 837.1, 30 (Mar. 2017), p. 30. DOI: 10.3847/1538-4357/aa5c41. arXiv: 1611.09144 [astro-ph.GA].

[151] Yuri Levin and Andrei M. Beloborodov. “Stellar disk in the galactic center - A Remnant of a dense accretion disk?” In: *Astrophys. J. Lett.* 590 (2003), pp. L33–L36. DOI: 10.1086/376675. arXiv: astro-ph/0303436.

[152] Ulf Lockmann, Holger Baumgardt, and Pavel Kroupa. “Origin of the S-Stars in the Galactic Center.” In: *Astrophys. J. Lett.* 683 (2008), p. L151. DOI: 10.1086/591734. arXiv: 0807.2239 [astro-ph].

[153] Evgeny Griv. "Origin of the Galactic Center S-Stars: Gravitational Torques from Lin-Shu-Type Spiral Density Waves." In: 709.2 (Feb. 2010), pp. 597–604. DOI: 10.1088/0004-637X/709/2/597.

[154] M. Fujii et al. "The Origin of S-stars and a Young Stellar Disk: Distribution of Debris Stars of a Sinking Star Cluster." In: 716.1 (June 2010), pp. L80–L84. DOI: 10.1088/2041-8205/716/1/L80. arXiv: 1003.4125 [astro-ph.GA].

[155] Brad Hansen and Milos Milosavljevic. "The need for a second black hole at the Galactic center." In: *Astrophys. J. Lett.* 593 (2003), p. L77. DOI: 10.1086/378182. arXiv: astro-ph/0306074.

[156] O. Straub et al. "Where intermediate-mass black holes could hide in the Galactic Centre - A full parameter study with the S2 orbit." In: *Astron. Astrophys.* 672 (2023). [Erratum: Astron.Astrophys. 677, C2 (2023)], A63. DOI: 10.1051/0004-6361/202245132. arXiv: 2303.04067 [astro-ph.GA].

[157] Clifford M. Will et al. "Constraining a Companion of the Galactic Center Black Hole Sgr A*." In: *Astrophys. J.* 959.1 (2023), p. 58. DOI: 10.3847/1538-4357/ad09b3. arXiv: 2307.16646 [astro-ph.GA].

[158] A. Eckart and R. Genzel. "Observations of stellar proper motions near the Galactic Centre." In: 383.6599 (Oct. 1996), pp. 415–417. DOI: 10.1038/383415a0.

[159] R. Genzel et al. "On the nature of the dark mass in the centre of the Milky Way." In: *Mon. Not. Roy. Astron. Soc.* 291 (1997), pp. 219–234. DOI: 10.1093/mnras/291.1.219.

[160] R. Genzel et al. "Stellar dynamics in the Galactic centre: Proper motions and anisotropy." In: *Mon. Not. Roy. Astron. Soc.* 317 (2000), p. 348. DOI: 10.1046/j.1365-8711.2000.03582.x. arXiv: astro-ph/0001428.

[161] A. M. Ghez et al. "The First Measurement of Spectral Lines in a Short-Period Star Bound to the Galaxy's Central Black Hole: A Paradox of Youth." In: *The Astrophysical Journal* 586.2 (Mar. 2003), p. L127. DOI: 10.1086/374804. URL: https://dx.doi.org/10.1086/374804.

[162] F. Martins et al. "On the Nature of the Fast-Moving Star S2 in the Galactic Center." In: 672.2 (Jan. 2008), p. L119. DOI: 10.1086/526768. arXiv: 0711.3344 [astro-ph].

[163] M. Habibi et al. "Twelve Years of Spectroscopic Monitoring in the Galactic Center: The Closest Look at S-stars near the Black Hole." In: 847.2, 120 (Oct. 2017), p. 120. DOI: 10.3847/1538-4357/aa876f. arXiv: 1708.06353 [astro-ph.SR].

[164] GRAVITY Collaboration et al. “First light for GRAVITY: Phase referencing optical interferometry for the Very Large Telescope Interferometer.” In: 602, A94 (June 2017), A94. DOI: 10.1051/0004-6361/201730838. arXiv: 1705.02345 [astro-ph.IM].

[165] Devin S. Chu et al. “Investigating the Binarity of S0-2: Implications for its Origins and Robustness as a Probe of the Laws of Gravity around a Supermassive Black Hole.” In: *Astrophys. J.* 854.1 (2018). [Erratum: Astrophys.J. 863, 111 (2018)], p. 12. DOI: 10.3847/1538-4357/aaa3eb. arXiv: 1709.04890 [astro-ph.SR].

[166] GRAVITY Collaboration. “Detection of the Schwarzschild precession in the orbit of the star S2 near the Galactic centre massive black hole.” In: 636 (2020), p. L5. DOI: 10.1051/0004-6361/202037813. arXiv: 2004.07187 [astro-ph.GA].

[167] GRAVITY Collaboration. “Mass distribution in the Galactic Center based on interferometric astrometry of multiple stellar orbits.” In: 657 (2022), p. L12. DOI: 10.1051/0004-6361/202142465. arXiv: 2112.07478 [astro-ph.GA].

[168] G. F. Rubilar and A. Eckart. “Periastron shifts of stellar orbits near the Galactic Center.” In: 374 (July 2001), pp. 95–104. DOI: 10.1051/0004-6361:20010640.

[169] David Merritt. *Dynamics and Evolution of Galactic Nuclei*. 2013.

[170] Gernot Heißel et al. “The dark mass signature in the orbit of S2.” In: *A&A* 660 (Dec. 2022), A13. DOI: 10.1051/0004-6361/202142114. arXiv: 2112.07778 [astro-ph.GA].

[171] Thomas Lacroix. “Dynamical constraints on a dark matter spike at the Galactic Centre from stellar orbits.” In: *Astron. Astrophys.* 619 (2018), A46. DOI: 10.1051/0004-6361/201832652. arXiv: 1801.01308 [astro-ph.GA].

[172] Paolo Gondolo and Joseph Silk. “Dark matter annihilation at the galactic center.” In: *Phys. Rev. Lett.* 83 (1999), pp. 1719–1722. DOI: 10.1103/PhysRevLett.83.1719. arXiv: astro-ph/9906391.

[173] Nitsan Bar et al. “Looking for ultralight dark matter near supermassive black holes.” In: *JCAP* 07 (2019), p. 045. DOI: 10.1088/1475-7516/2019/07/045. arXiv: 1905.11745 [astro-ph.CO].

[174] Riccardo Della Monica and Ivan de Martino. “Narrowing the allowed mass range of ultralight bosons with the S2 star.” In: *Astron. Astrophys.* 670 (2023), p. L4. DOI: 10.1051/0004-6361/202245150. arXiv: 2206.03980 [gr-qc].

[175] Hsi-Yu Schive, Tzihong Chiueh, and Tom Broadhurst. “Cosmic Structure as the Quantum Interference of a Coherent Dark Wave.” In: *Nature Phys.* 10 (2014), pp. 496–499. DOI: 10.1038/nphys2996. arXiv: 1406.6586 [astro-ph.GA].

[176] Lam Hui et al. “Ultralight scalars as cosmological dark matter.” In: *Phys. Rev. D* 95.4 (2017), p. 043541. DOI: `10.1103/PhysRevD.95.043541`. arXiv: `1610.08297 [astro-ph.CO]`.

[177] Philip Mocz et al. “Galaxy formation with BECDM – I. Turbulence and relaxation of idealized haloes.” In: *Mon. Not. Roy. Astron. Soc.* 471.4 (2017), pp. 4559–4570. DOI: `10.1093/mnras/stx1887`. arXiv: `1705.05845 [astro-ph.CO]`.

[178] Hsi-Yu Schive et al. “Understanding the Core-Halo Relation of Quantum Wave Dark Matter from 3D Simulations.” In: *Phys. Rev. Lett.* 113.26 (2014), p. 261302. DOI: `10.1103/PhysRevLett.113.261302`. arXiv: `1407.7762 [astro-ph.GA]`.

[179] H. C. Plummer. “On the problem of distribution in globular star clusters.” In: 71 (Mar. 1911), pp. 460–470. DOI: `10.1093/mnras/71.5.460`.

[180] Zhao-Qiang Shen et al. “Exploring dark matter spike distribution around the Galactic centre with stellar orbits.” In: *Mon. Not. Roy. Astron. Soc.* 527 (2024), p. 3196. DOI: `10.1093/mnras/stad3282`. arXiv: `2303.09284 [astro-ph.GA]`.

[181] Julio F. Navarro et al. “The Inner structure of Lambda-CDM halos 3: Universality and asymptotic slopes.” In: *Mon. Not. Roy. Astron. Soc.* 349 (2004), p. 1039. DOI: `10.1111/j.1365-2966.2004.07586.x`. arXiv: `astro-ph/0311231`.

[182] Jianling Wang, Francois Hammer, and Yanbin Yang. “Milky Way total mass derived by rotation curve and globular cluster kinematics from Gaia EDR3.” In: *Mon. Not. Roy. Astron. Soc.* 510.2 (2022), pp. 2242–2260. DOI: `10.1093/mnras/stab3258`. arXiv: `2111.09324 [astro-ph.GA]`.

[183] Leor Barack et al. “Black holes, gravitational waves and fundamental physics: a roadmap.” In: *Class. Quant. Grav.* 36.14 (2019), p. 143001. DOI: `10.1088/1361-6382/ab0587`. arXiv: `1806.05195 [gr-qc]`.

[184] Emanuele Berti et al. “Testing General Relativity with Present and Future Astrophysical Observations.” In: *Class. Quant. Grav.* 32 (2015), p. 243001. DOI: `10.1088/0264-9381/32/24/243001`. arXiv: `1501.07274 [gr-qc]`.

[185] C. Brans and R. H. Dicke. “Mach’s Principle and a Relativistic Theory of Gravitation.” In: *Phys. Rev.* 124 (3 Nov. 1961), pp. 925–935. DOI: `10.1103/PhysRev.124.925`. URL: `https://link.aps.org/doi/10.1103/PhysRev.124.925`.

[186] D. Lovelock. “The Einstein tensor and its generalizations.” In: *J. Math. Phys.* 12 (1971), pp. 498–501. DOI: `10.1063/1.1665613`.

[187] D. Lovelock. “The four-dimensionality of space and the einstein tensor.” In: *J. Math. Phys.* 13 (1972), pp. 874–876. DOI: `10.1063/1.1666069`.

[188] Pierre Touboul et al. “MICROSCOPE Mission: Final Results of the Test of the Equivalence Principle.” In: *Phys. Rev. Lett.* 129.12 (2022), p. 121102. DOI: `10.1103/PhysRevLett.129.121102`. arXiv: `2209.15487 [gr-qc]`.

[189] Gregory Walter Horndeski. “Second-order scalar-tensor field equations in a four-dimensional space.” In: *Int. J. Theor. Phys.* 10 (1974), pp. 363–384. DOI: `10.1007/BF01807638`.

[190] John D. Barrow and S. Cotsakis. “Inflation and the Conformal Structure of Higher Order Gravity Theories.” In: *Phys. Lett. B* 214 (1988), pp. 515–518. DOI: `10.1016/0370-2693(88)90110-4`.

[191] David Wands. “Extended gravity theories and the Einstein-Hilbert action.” In: *Class. Quant. Grav.* 11 (1994), pp. 269–280. DOI: `10.1088/0264-9381/11/1/025`. arXiv: `gr-qc/9307034`.

[192] Thomas P. Sotiriou. “f(R) gravity and scalar-tensor theory.” In: *Class. Quant. Grav.* 23 (2006), pp. 5117–5128. DOI: `10.1088/0264-9381/23/17/003`. arXiv: `gr-qc/0604028`.

[193] J. W. Moffat. “Scalar-tensor-vector gravity theory.” In: *JCAP* 03 (2006), p. 004. DOI: `10.1088/1475-7516/2006/03/004`. arXiv: `gr-qc/0506021`.

[194] Andreas Eckart et al. “The Milky Way’s Supermassive Black Hole: How Good a Case Is It?” In: *Found. Phys.* 47.5 (2017), pp. 553–624. DOI: `10.1007/s10701-017-0079-2`. arXiv: `1703.09118 [astro-ph.HE]`.

[195] Mariafelicia De Laurentis, Ivan De Martino, and Ruth Lazkoz. “Modified gravity revealed along geodesic tracks.” In: *Eur. Phys. J. C* 78.11 (2018), p. 916. DOI: `10.1140/epjc/s10052-018-6401-0`. arXiv: `1811.00046 [gr-qc]`.

[196] Austin Joyce et al. “Beyond the Cosmological Standard Model.” In: *Phys. Rept.* 568 (2015), pp. 1–98. DOI: `10.1016/j.physrep.2014.12.002`. arXiv: `1407.0059 [astro-ph.CO]`.

[197] Duško Borka et al. “Estimating the Parameters of Extended Gravity Theories with the Schwarzschild Precession of S2 Star.” In: *Universe* 7.11 (2021), p. 407. DOI: `10.3390/universe7110407`. arXiv: `2111.00578 [gr-qc]`.

[198] Mariafelicia De Laurentis et al. “Test-particle dynamics in general spherically symmetric black hole spacetimes.” In: *Phys. Rev. D* 97.10 (2018), p. 104024. DOI: `10.1103/PhysRevD.97.104024`. arXiv: `1712.00265 [gr-qc]`.

[199] Sanjeev Kalita. “Gravitational Theories near the Galactic Center.” In: *Astrophys. J.* 855.1 (2018), p. 70. DOI: `10.3847/1538-4357/aaadbb`.

[200] A. Hees et al. “Violation of the equivalence principle from light scalar fields: from Dark Matter candidates to scalarized black holes.” In: *54th Rencontres de Moriond on Gravitation*. May 2019. arXiv: `1905.08524 [gr-qc]`.

[201] W. Brandner et al. “NAOS+CONICA at YEPUN: first VLT adaptive optics system sees first light.” In: *The Messenger* 107 (Mar. 2002), pp. 1–6.

[202] F. Eisenhauer et al. “GRAVITY: Microarcsecond Astrometry and Deep Interferometric Imaging with the VLT.” In: *Moorwood, Alan F. M.: Science with the VLT in the ELT Era, Springer, 361-368 (2009)* (Jan. 2009). DOI: `10.1007/978-1-4020-9190-2_61`.

[203] S. Gillessen et al. “GRAVITY: a four-telescope beam combiner instrument for the VLTI.” In: *Optical and Infrared Interferometry II*. Ed. by William C. Danchi, Françoise Delplancke, and Jayadev K. Rajagopal. Vol. 7734. Society of Photo-Optical Instrumentation Engineers (SPIE) Conference Series. July 2010, 77340Y, 77340Y. DOI: `10.1117/12.856689`. arXiv: `1007.1612 [astro-ph.IM]`.

[204] Frank Eisenhauer et al. “Sinfoni - integral field spectroscopy at 50 milli-arcsecond resolution with the eso vlt.” In: *Proc. SPIE Int. Soc. Opt. Eng.* 4841 (2003), pp. 1548–1561. DOI: `10.1117/12.459468`. arXiv: `astro-ph/0306191`.

[205] Gravity+ Collaboration et al. “The GRAVITY+ Project: Towards All-sky, Faint-Science, High-Contrast Near-Infrared Interferometry at the VLTI.” In: *The Messenger* 189 (Dec. 2022), pp. 17–22. DOI: `10.18727/0722-6691/5285`. arXiv: `2301.08071 [astro-ph.IM]`.

[206] Piero Madau and Mark Dickinson. “Cosmic Star Formation History.” In: *Ann. Rev. Astron. Astrophys.* 52 (2014), pp. 415–486. DOI: `10.1146/annurev-astro-081811-125615`. arXiv: `1403.0007 [astro-ph.CO]`.

[207] James Aird et al. “The evolution of the X-ray luminosity functions of unabsorbed and absorbed AGNs out to z∼ 5.” In: *Mon. Not. Roy. Astron. Soc.* 451.2 (2015), pp. 1892–1927. DOI: `10.1093/mnras/stv1062`. arXiv: `1503.01120 [astro-ph.HE]`.

[208] Josef Lense and Hans Thirring. “Ueber den Einfluss der Eigenrotation der Zentralkoerper auf die Bewegung der Planeten und Monde nach der Einsteinschen Gravitationstheorie.” In: *Phys. Z.* 19 (1918), pp. 156–163.

[209] Fupeng Zhang, Youjun Lu, and Qingjuan Yu. “On Testing the Kerr Metric of the Massive Black Hole in the Galactic Center via Stellar Orbital Motion: Full General Relativistic Treatment.” In: *Astrophys. J.* 809.2 (2015), p. 127. DOI: `10.1088/0004-637X/809/2/127`. arXiv: `1508.06293 [astro-ph.HE]`.

[210] Idel Waisberg et al. “What stellar orbit is needed to measure the spin of the Galactic centre black hole from astrometric data?” In: *Mon. Not. Roy. Astron. Soc.* 476.3 (2018), pp. 3600–3610. DOI: `10.1093/mnras/sty476`. arXiv: `1802.08198 [astro-ph.GA]`.

[211] Eanna E. Flanagan and Tanja Hinderer. “Constraining neutron star tidal Love numbers with gravitational wave detectors.” In: *Phys. Rev. D* 77 (2008), 021502(R). DOI: `10.1103/PhysRevD.77.021502`. arXiv: `0709.1915 [astro-ph]`.

[212] Tim Dietrich, Tanja Hinderer, and Anuradha Samajdar. “Interpreting Binary Neutron Star Mergers: Describing the Binary Neutron Star Dynamics, Modelling Gravitational Waveforms, and Analyzing Detections.” In: (Apr. 2020). arXiv: `2004.02527 [gr-qc]`.

[213] Pawan Kumar Gupta, Jan Steinhoff, and Tanja Hinderer. “Relativistic effective action of dynamical gravitomagnetic tides for slowly rotating neutron stars.” In: (Nov. 2020). arXiv: `2011.03508 [gr-qc]`.

[214] Piotr T. Chrusciel, Joao Lopes Costa, and Markus Heusler. “Stationary Black Holes: Uniqueness and Beyond.” In: *Living Rev. Rel.* 15 (2012), p. 7. DOI: `10.12942/lrr-2012-7`. arXiv: `1205.6112 [gr-qc]`.

[215] Vitor Cardoso and Leonardo Gualtieri. “Testing the black hole ‘no-hair’ hypothesis.” In: *Class. Quant. Grav.* 33.17 (2016), p. 174001. DOI: `10.1088/0264-9381/33/17/174001`. arXiv: `1607.03133 [gr-qc]`.

[216] Vitor Cardoso et al. “Testing strong-field gravity with tidal Love numbers.” In: *Phys. Rev. D* 95.8 (2017). [Addendum: Phys.Rev.D 95, 089901 (2017)], p. 084014. DOI: `10.1103/PhysRevD.95.084014`. arXiv: `1701.01116 [gr-qc]`.

[217] Noah Sennett et al. “Distinguishing Boson Stars from Black Holes and Neutron Stars from Tidal Interactions in Inspiraling Binary Systems.” In: *Phys. Rev. D* 96.2 (2017), p. 024002. DOI: `10.1103/PhysRevD.96.024002`. arXiv: `1704.08651 [gr-qc]`.

[218] Smadar Naoz et al. “A hidden friend for the galactic center black hole, Sgr A*.” In: *Astrophys. J. Lett.* 888.1 (2020), p. L8. DOI: `10.3847/2041-8213/ab5e3b`. arXiv: `1912.04910 [astro-ph.GA]`.

[219] GRAVITY Collaboration. “Detection of the gravitational redshift in the orbit of the star S2 near the Galactic centre massive black hole.” In: *A&A* 615 (2018), p. L15. DOI: `10.1051/0004-6361/201833718`. arXiv: `1807.09409 [astro-ph.GA]`.

[220] Carl D. Murray and Stanley F. Dermott. *Solar System Dynamics*. Cambridge University Press, 2000. DOI: `10.1017/CBO9781139174817`.

[221] R C Domingos, R Vilhena de Moraes, and D A P Bertachini. "Third-Body Perturbation in the Case of Elliptic Orbits for the Disturbing Body." In: *Mathematical Problems in Engineering* 2008 (2008). DOI: 10.1155/2008/763654.

[222] S. Chandrasekhar. *The Mathematical Theory of Black Holes*. New York: Oxford University Press, 1983.

[223] Vitor Cardoso et al. "Geodesic stability, Lyapunov exponents and quasinormal modes." In: *Phys. Rev. D* 79 (2009), p. 064016. DOI: 10.1103/PhysRevD.79.064016. arXiv: 0812.1806 [hep-th].

[224] Vitor Cardoso, Edgardo Franzin, and Paolo Pani. "Is the gravitational-wave ringdown a probe of the event horizon?" In: *Phys. Rev. Lett.* 116.17 (2016), p. 171101. DOI: 10.1103/PhysRevLett.116.171101. arXiv: 1602.07309 [gr-qc].

[225] Huan Yang. "Relating Black Hole Shadow to Quasinormal Modes for Rotating Black Holes." In: (Jan. 2021). arXiv: 2101.11129 [gr-qc].

[226] Keisuke Nakashi and Takahisa Igata. "Innermost stable circular orbits in the Majumdar-Papapetrou dihole spacetime." In: *Phys. Rev. D* 99.12 (2019), p. 124033. DOI: 10.1103/PhysRevD.99.124033. arXiv: 1903.10121 [gr-qc].

[227] Keisuke Nakashi and Takahisa Igata. "Effect of a second compact object on stable circular orbits." In: *Phys. Rev. D* 100.10 (2019), p. 104006. DOI: 10.1103/PhysRevD.100.104006. arXiv: 1908.10075 [gr-qc].

[228] Thiago Assumpcao et al. "Black hole binaries: ergoregions, photon surfaces, wave scattering, and quasinormal modes." In: *Phys. Rev. D* 98.6 (2018), p. 064036. DOI: 10.1103/PhysRevD.98.064036. arXiv: 1806.07909 [gr-qc].

[229] Laura Bernard et al. "Physics of black hole binaries: Geodesics, relaxation modes, and energy extraction." In: *Phys. Rev. D* 100.4 (2019), p. 044002. DOI: 10.1103/PhysRevD.100.044002. arXiv: 1905.05204 [gr-qc].

[230] Álvar Daza et al. "Wada structures in a binary black hole system." In: *Phys. Rev. D* 98.8 (2018), p. 084050. DOI: 10.1103/PhysRevD.98.084050. arXiv: 1807.10741 [gr-qc].

[231] Tullio Regge and John A. Wheeler. "Stability of a Schwarzschild singularity." In: *Phys. Rev.* 108 (1957), pp. 1063–1069. DOI: 10.1103/PhysRev.108.1063.

[232] F.J. Zerilli. "Gravitational field of a particle falling in a schwarzschild geometry analyzed in tensor harmonics." In: *Phys. Rev. D* 2 (1970), pp. 2141–2160. DOI: 10.1103/PhysRevD.2.2141.

[233] K.S. Thorne. "Multipole Expansions of Gravitational Radiation." In: *Rev. Mod. Phys.* 52 (1980), pp. 299–339. DOI: `10.1103/RevModPhys.52.299`.

[234] Xiao He Zhang. "Multipole expansions of the general-relativistic gravitational field of the external universe." In: *Phys. Rev. D* 34.4 (1986), pp. 991–1004. DOI: `10.1103/PhysRevD.34.991`.

[235] Taylor Binnington and Eric Poisson. "Relativistic theory of tidal Love numbers." In: *Phys. Rev.* D80 (2009), p. 084018. DOI: `10.1103/PhysRevD.80.084018`. arXiv: `0906.1366 [gr-qc]`.

[236] E. Poisson and C.M. Will. "Gravity: Newtonian, Post-Newtonian, Relativistic." In: *Gravity: Newtonian, Post-Newtonian, Relativistic* (Jan. 2012), pp. 1–780. DOI: `10.1017/CBO9781139507486`.

[237] Vitor Cardoso, Francisco Duque, and Taishi Ikeda. "Tidal effects and disruption in superradiant clouds: a numerical investigation." In: (2020). arXiv: `2001.01729 [gr-qc]`.

[238] S. Chandrasekhar and S. Detweiler. "The Quasi-Normal Modes of the Schwarzschild Black Hole." In: *Proceedings of the Royal Society of London Series A* 344.1639 (Aug. 1975), pp. 441–452. DOI: `10.1098/rspa.1975.0112`.

[239] C. V. Vishveshwara. "Scattering of Gravitational Radiation by a Schwarzschild Black-hole." In: *Nature* 227 (1970), pp. 936–938. DOI: `10.1038/227936a0`.

[240] Valeria Ferrari and Bahram Mashhoon. "New approach to the quasinormal modes of a black hole." In: *Phys. Rev. D* 30 (1984), pp. 295–304. DOI: `10.1103/PhysRevD.30.295`.

[241] B. F. Schutz and C. M. Will. "Black hole normal modes - A semianalytic approach." In: 291 (Apr. 1985), pp. L33–L36. DOI: `10.1086/184453`.

[242] Edward W. Leaver. "Spectral decomposition of the perturbation response of the Schwarzschild geometry." In: *Phys. Rev. D* 34 (1986), pp. 384–408. DOI: `10.1103/PhysRevD.34.384`.

[243] Emanuele Berti, Vitor Cardoso, and Clifford M. Will. "On gravitational-wave spectroscopy of massive black holes with the space interferometer LISA." In: *Phys. Rev. D* 73 (2006), p. 064030. DOI: `10.1103/PhysRevD.73.064030`. arXiv: `gr-qc/0512160`.

[244] Emanuele Berti, Vitor Cardoso, and Andrei O. Starinets. "Quasinormal modes of black holes and black branes." In: *Class. Quant. Grav.* 26 (2009), p. 163001. DOI: `10.1088/0264-9381/26/16/163001`. arXiv: `0905.2975 [gr-qc]`.

[245] Huan Yang et al. "Quasinormal-mode spectrum of Kerr black holes and its geometric interpretation." In: *Phys. Rev. D* 86 (2012), p. 104006. DOI: `10.1103/PhysRevD.86.104006`. arXiv: `1207.4253 [gr-qc]`.

[246] Sai Iyer. "Black-hole normal modes: A WKB approach. II. Schwarzschild black holes." In: *Phys. Rev. D* 35 (12 June 1987), pp. 3632–3636. DOI: `10.1103/PhysRevD.35.3632`. URL: `https://link.aps.org/doi/10.1103/PhysRevD.35.3632`.

[247] Vitor Cardoso and Paolo Pani. "Tests for the existence of black holes through gravitational wave echoes." In: *Nat. Astron.* 1.9 (2017), pp. 586–591. DOI: `10.1038/s41550-017-0225-y`. arXiv: `1709.01525 [gr-qc]`.

[248] Pablo A. Cano, Kwinten Fransen, and Thomas Hertog. "Ringing of rotating black holes in higher-derivative gravity." In: *Phys. Rev. D* 102.4 (2020), p. 044047. DOI: `10.1103/PhysRevD.102.044047`. arXiv: `2005.03671 [gr-qc]`.

[249] Richard Brito, Vitor Cardoso, and Paolo Pani. "Superradiant instability of black holes immersed in a magnetic field." In: *Phys. Rev. D* 89.10 (2014), p. 104045. DOI: `10.1103/PhysRevD.89.104045`. arXiv: `1405.2098 [gr-qc]`.

[250] P. T. Leung et al. "Quasinormal modes of dirty black holes." In: *Phys. Rev. Lett.* 78 (1997), pp. 2894–2897. DOI: `10.1103/PhysRevLett.78.2894`. arXiv: `gr-qc/9903031 [gr-qc]`.

[251] Enrico Barausse, Vitor Cardoso, and Paolo Pani. "Can environmental effects spoil precision gravitational-wave astrophysics?" In: *Phys. Rev.* D89.10 (2014), p. 104059. DOI: `10.1103/PhysRevD.89.104059`. arXiv: `1404.7149 [gr-qc]`.

[252] Eugene I Butikov. "A dynamical picture of the oceanic tides." In: *American Journal of Physics* 70.10 (2002), pp. 1001–1011. DOI: `10.1119/1.1498858`.

[253] Poul Hjorth and Jens Martin Knudsen. *Elements of Newtonian mechanics*. Germany: Springer Verlag, 1996.

[254] Filippo Camilloni et al. "Tidal deformations of a binary system induced by an external Kerr black hole." In: *Phys. Rev. D* 107.8 (2023), p. 084011. DOI: `10.1103/PhysRevD.107.084011`. arXiv: `2301.04879 [gr-qc]`.

[255] Byron D Tapley et al. "The gravity recovery and climate experiment: Mission overview and early results." In: *Geophysical Research Letters* 31.9 (2004).

[256] MR Drinkwater et al. "GOCE: ESA's first Earth Explorer Core mission." In: *Earth gravity field from space—From sensors to earth sciences*. Springer, 2003, pp. 419–432.

[257] Ignazio Ciufolini, Antonio Paolozzi, and Claudio Paris. "Overview of the LARES Mission: orbit, error analysis and technological aspects." In: *Journal of Physics: Conference Series*. Vol. 354. 1. IOP Publishing. 2012, p. 012002.

[258] C. T. Cunningham and J. M. Bardeen. “The Optical Appearance of a Star Orbiting an Extreme Kerr Black Hole.” In: 173 (May 1972), p. L137. DOI: 10.1086/180933.

[259] J.-P. Luminet. “Image of a spherical black hole with thin accretion disk.” In: *Astron. Astrophys.* 75 (1979), pp. 228–235.

[260] Heino Falcke, Fulvio Melia, and Eric Agol. “Viewing the shadow of the black hole at the galactic center.” In: *Astrophys. J. Lett.* 528 (2000), p. L13. DOI: 10.1086/312423. arXiv: astro-ph/9912263.

[261] Vitor Cardoso and Rodrigo Vicente. “Moving black holes: energy extraction, absorption cross-section and the ring of fire.” In: *Phys. Rev. D* 100.8 (2019), p. 084001. DOI: 10.1103/PhysRevD.100.084001. arXiv: 1906.10140 [gr-qc].

[262] Samuel E. Gralla, Alexandru Lupsasca, and Daniel P. Marrone. “The shape of the black hole photon ring: A precise test of strong-field general relativity.” In: *Phys. Rev. D* 102.12 (2020), p. 124004. DOI: 10.1103/PhysRevD.102.124004. arXiv: 2008.03879 [gr-qc].

[263] Pedro V. P. Cunha and Carlos A. R. Herdeiro. “Shadows and strong gravitational lensing: a brief review.” In: *Gen. Rel. Grav.* 50.4 (2018), p. 42. DOI: 10.1007/s10714-018-2361-9. arXiv: 1801.00860 [gr-qc].

[264] M. Bauböck et al. “Modeling the orbital motion of Sgr A*’s near-infrared flares.” In: *Astron. Astrophys.* 635 (2020), A143. DOI: 10.1051/0004-6361/201937233. arXiv: 2002.08374 [astro-ph.HE].

[265] Joseph F. Dolan. “Dying Pulse Trains in Cygnus XR-1: Evidence for an Event Horizon?” In: 113.786 (Aug. 2001), pp. 974–982. DOI: 10.1086/322917.

[266] Joseph F. Dolan and Daria C Auerswald. “A Search for Dying Pulse Trains in Cyg X-1 using RXTE.” In: *arXiv e-prints*, arXiv:1104.3164 (Apr. 2011), arXiv:1104.3164. arXiv: 1104.3164 [astro-ph.HE].

[267] I. D. Novikov and Ja. B. Zeldovich. “Physics of relativistic collapse.” In: *International Conference on Relativistic Theories of Gravitation*. Vol. 1. 1965.

[268] M. A. Podurets. “Asymptotic Behavior of the Optical Luminosity of a Star in Gravitational Collapse.” In: 8 (June 1965), p. 868.

[269] William L. Ames and Kip S. Thorne. “The Optical Appearance of a Star that is Collapsing Through its Gravitational Radius.” In: 151 (Feb. 1968), p. 659. DOI: 10.1086/149465.

[270] Joe Keir. "Slowly decaying waves on spherically symmetric spacetimes and ultracompact neutron stars." In: *Class. Quant. Grav.* 33.13 (2016), p. 135009. DOI: 10.1088/0264-9381/33/13/135009. arXiv: 1404.7036 [gr-qc].

[271] Vitor Cardoso et al. "Light rings as observational evidence for event horizons: long-lived modes, ergoregions and nonlinear instabilities of ultracompact objects." In: *Phys. Rev. D* 90.4 (2014), p. 044069. DOI: 10.1103/PhysRevD.90.044069. arXiv: 1406.5510 [gr-qc].

[272] William H. Press. "Long Wave Trains of Gravitational Waves from a Vibrating Black Hole." In: *The Astrophysical Journal Letters* 170 (Dec. 1971), p. L105. DOI: 10.1086/180849.

[273] J. M. Cohen et al. "Observable Blueshifts Near Compact Objects." In: 88.2 (Dec. 1982), pp. 307–312. DOI: 10.1007/BF01092704.

[274] Yasusada Nambu and Sousuke Noda. "Wave Optics in Black Hole Spacetimes: Schwarzschild Case." In: *Class. Quant. Grav.* 33 (2016), p. 075011. DOI: 10.1088/0264-9381/33/7/075011. arXiv: 1502.05468 [gr-qc].

[275] Yasusada Nambu, Sousuke Noda, and Yuichiro Sakai. "Wave Optics in Spacetimes with Compact Gravitating Object." In: *Phys. Rev. D* 100.6 (2019), p. 064037. DOI: 10.1103/PhysRevD.100.064037. arXiv: 1905.01793 [gr-qc].

[276] William Krivan et al. "Dynamics of perturbations of rotating black holes." In: *Physical Review D* 56.6 (Sept. 1997), 3395–3404. ISSN: 1089-4918. DOI: 10.1103/physrevd.56.3395. URL: http://dx.doi.org/10.1103/PhysRevD.56.3395.

[277] Ramon Lopez-Aleman, Gaurav Khanna, and Jorge Pullin. "Perturbative evolution of particle orbits around Kerr black holes: Time domain calculation." In: *Class. Quant. Grav.* 20 (2003), pp. 3259–3268. DOI: 10.1088/0264-9381/20/14/320. arXiv: gr-qc/0303054 [gr-qc].

[278] Enrique Pazos-Ávalos and Carlos O. Lousto. "Numerical integration of the Teukolsky equation in the time domain." In: *Physical Review D* 72.8 (Oct. 2005). ISSN: 1550-2368. DOI: 10.1103/physrevd.72.084022. URL: http://dx.doi.org/10.1103/PhysRevD.72.084022.

[279] Pranesh A. Sundararajan, Gaurav Khanna, and Scott A. Hughes. "Towards adiabatic waveforms for inspiral into Kerr black holes. I. A New model of the source for the time domain perturbation equation." In: *Phys. Rev.* D76 (2007), p. 104005. DOI: 10.1103/PhysRevD.76.104005. arXiv: gr-qc/0703028 [gr-qc].

[280] Vitor Cardoso, Francisco Duque, and Gaurav Khanna. "Gravitational tuning forks and hierarchical triple systems." In: (Jan. 2021). arXiv: 2101.01186 [gr-qc].

[281] Saul A. Teukolsky. “Perturbations of a rotating black hole. 1. Fundamental equations for gravitational electromagnetic and neutrino field perturbations.” In: *Astrophys. J.* 185 (1973), pp. 635–647. DOI: 10.1086/152444.

[282] R. Abbott et al. “Tests of general relativity with binary black holes from the second LIGO-Virgo gravitational-wave transient catalog.” In: *Phys. Rev. D* 103.12 (2021), p. 122002. DOI: 10.1103/PhysRevD.103.122002. arXiv: 2010.14529 [gr-qc].

[283] R. Abbott et al. “Tests of General Relativity with GWTC-3.” In: (Dec. 2021). arXiv: 2112.06861 [gr-qc].

[284] Enno Harms et al. “A new gravitational wave generation algorithm for particle perturbations of the Kerr spacetime.” In: *Class. Quant. Grav.* 31.24 (2014), p. 245004. DOI: 10.1088/0264-9381/31/24/245004. arXiv: 1406.5983 [gr-qc].

[285] Michael D. Johnson et al. “Universal interferometric signatures of a black hole’s photon ring.” In: *Sci. Adv.* 6.12 (2020), eaaz1310. DOI: 10.1126/sciadv.aaz1310. arXiv: 1907.04329 [astro-ph.IM].

[286] Peter Galison et al. “The Next Generation Event Horizon Telescope Collaboration: History, Philosophy, and Culture.” In: *Galaxies* 11.1 (2023), p. 32. DOI: 10.3390/galaxies11010032. arXiv: 2304.02463 [physics.hist-ph].

[287] Michael D. Johnson et al. “Key Science Goals for the Next-Generation Event Horizon Telescope.” In: *Galaxies* 11 (2023), p. 61. DOI: 10.3390/galaxies11030061. arXiv: 2304.11188 [astro-ph.HE].

[288] M. Grould et al. “General relativistic effects on the orbit of the S2 star with GRAVITY.” In: *Astron. Astrophys.* 608 (2017), A60. DOI: 10.1051/0004-6361/201731148. arXiv: 1709.04492 [astro-ph.HE].

[289] Joseph H. Catanzarite. “A new algorithm for fitting orbits of multiple-planet systems to combined RV and astrometric data.” In: *arXiv e-prints*, arXiv:1008.3416 (Aug. 2010), arXiv:1008.3416. DOI: 10.48550/arXiv.1008.3416. arXiv: 1008.3416 [astro-ph.EP].

[290] Clifford M. Will and Kenneth Nordtvedt Jr. “Conservation Laws and Preferred Frames in Relativistic Gravity. I. Preferred-Frame Theories and an Extended PPN Formalism.” In: *Astrophys. J.* 177 (1972), p. 757. DOI: 10.1086/151754.

[291] Clifford M. Will. “Testing the general relativistic no-hair theorems using the Galactic center black hole SgrA*.” In: *Astrophys. J. Lett.* 674 (2008), pp. L25–L28. DOI: 10.1086/528847. arXiv: 0711.1677 [astro-ph].

[292] Gernot Heißel et al. “Non-uniqueness of relativistic orbital parametrisations. To ray-trace, or not to ray-trace?” In preparation.

[293] Ephraim Fischbach and Belvin S. Freeman. “Second Order Contribution to the Gravitational Deflection of Light.” In: *Phys. Rev. D* 22 (1980), p. 2950. DOI: 10.1103/PhysRevD.22.2950.

[294] R. Epstein and I. I. Shapiro. “POST POSTNEWTONIAN DEFLECTION OF LIGHT BY THE SUN.” In: *Phys. Rev. D* 22 (1980), pp. 2947–2949. DOI: 10.1103/PhysRevD.22.2947.

[295] V. A. Brumberg. *Essential relativistic celestial mechanics.* 1991.

[296] S. A. Klioner, E. Gerlach, and M. H. Soffel. “Relativistic aspects of rotational motion of celestial bodies.” In: *Relativity in Fundamental Astronomy: Dynamics, Reference Frames, and Data Analysis*. Ed. by Sergei A. Klioner, P. Kenneth Seidelmann, and Michael H. Soffel. Vol. 261. Jan. 2010, pp. 112–123. DOI: 10.1017/S174392130999024X. arXiv: 1001.0915 [astro-ph.EP].

[297] Diogo C. Ribeiro et al. “Revisiting the PN formalism: an efficient formula for expanding metrics in General Relativity.” In preparation.

[298] Jonathan Goodman and Jonathan Weare. “Ensemble samplers with affine invariance.” In: *Communications in Applied Mathematics and Computational Science* 5.1 (Jan. 2010), pp. 65–80. DOI: 10.2140/camcos.2010.5.65.

[299] Daniel Foreman-Mackey et al. “emcee: The MCMC Hammer.” In: 125.925 (Mar. 2013), p. 306. DOI: 10.1086/670067. arXiv: 1202.3665 [astro-ph.IM].

[300] P. M. Plewa et al. “Pinpointing the near-infrared location of Sgr A* by correcting optical distortion in the NACO imager.” In: 453.3 (Nov. 2015), pp. 3234–3244. DOI: 10.1093/mnras/stv1910. arXiv: 1509.01941 [astro-ph.GA].

[301] Robert E. Kass and Adrian E. Raftery. “Bayes Factors.” In: *J. Am. Statist. Assoc.* 90.430 (1995), pp. 773–795. DOI: 10.1080/01621459.1995.10476572.

[302] Steven Lewis and Adrian Raftery. “Estimating Bayes Factors via Posterior Simulation With the Laplace-Metropolis Estimator.” In: *Journal of the American Statistical Association* 92 (1999). DOI: 10.1080/01621459.1997.10474016.

[303] Alan Heavens et al. “Marginal Likelihoods from Monte Carlo Markov Chains.” In: (Apr. 2017). arXiv: 1704.03472 [stat.CO].

[304] R. H. Dicke. “Coherence in Spontaneous Radiation Processes.” In: *Phys. Rev.* 93 (1954), pp. 99–110. DOI: 10.1103/PhysRev.93.99.

[305] William H. Press and Saul A. Teukolsky. "Floating Orbits, Superradiant Scattering and the Black-hole Bomb." In: *Nature* 238 (1972), pp. 211–212. DOI: 10.1038/238211a0.

[306] S. A. Teukolsky and W. H. Press. "Perturbations of a rotating black hole. III. Interaction of the hole with gravitational and electromagnetic radiation." In: 193 (Oct. 1974), pp. 443–461. DOI: 10.1086/153180.

[307] S. A. Teukolsky. "Rotating black holes - separable wave equations for gravitational and electromagnetic perturbations." In: *Phys. Rev. Lett.* 29 (1972), pp. 1114–1118. DOI: 10.1103/PhysRevLett.29.1114.

[308] J. N. Goldberg et al. "Spin s spherical harmonics and edth." In: *J. Math. Phys.* 8 (1967), p. 2155. DOI: 10.1063/1.1705135.

[309] Hirotada Okawa, Helvi Witek, and Vitor Cardoso. "Black holes and fundamental fields in Numerical Relativity: initial data construction and evolution of bound states." In: *Phys. Rev. D* 89.10 (2014), p. 104032. DOI: 10.1103/PhysRevD.89.104032. arXiv: 1401.1548 [gr-qc].

[310] Miguel Zilhão, Helvi Witek, and Vitor Cardoso. "Nonlinear interactions between black holes and Proca fields." In: *Class. Quant. Grav.* 32 (2015), p. 234003. DOI: 10.1088/0264-9381/32/23/234003. arXiv: 1505.00797 [gr-qc].

[311] William E. East and Frans Pretorius. "Superradiant Instability and Backreaction of Massive Vector Fields around Kerr Black Holes." In: *Phys. Rev. Lett.* 119.4 (2017), p. 041101. DOI: 10.1103/PhysRevLett.119.041101. arXiv: 1704.04791 [gr-qc].

[312] William E. East. "Massive Boson Superradiant Instability of Black Holes: Nonlinear Growth, Saturation, and Gravitational Radiation." In: *Phys. Rev. Lett.* 121.13 (2018), p. 131104. DOI: 10.1103/PhysRevLett.121.131104. arXiv: 1807.00043 [gr-qc].

[313] Cosimo Bambi, Stavros Katsanevas, and Kostas D. Kokkotas, eds. *Handbook of Gravitational Wave Astronomy*. Springer Singapore, 2021. ISBN: 978-981-15-4702-7. DOI: 10.1007/978-981-15-4702-7.

[314] Carlos A. R. Herdeiro and Eugen Radu. "Dynamical Formation of Kerr Black Holes with Synchronized Hair: An Analytic Model." In: *Phys. Rev. Lett.* 119.26 (2017), p. 261101. DOI: 10.1103/PhysRevLett.119.261101. arXiv: 1706.06597 [gr-qc].

[315] Carlos Herdeiro, Eugen Radu, and Helgi Rúnarsson. "Kerr black holes with Proca hair." In: *Class. Quant. Grav.* 33.15 (2016), p. 154001. DOI: 10.1088/0264-9381/33/15/154001. arXiv: 1603.02687 [gr-qc].

[316] Vitor Cardoso et al. “Floating and sinking: The Imprint of massive scalars around rotating black holes.” In: *Phys. Rev. Lett.* 107 (2011), p. 241101. DOI: 10.1103/PhysRevLett.107.241101. arXiv: 1109.6021 [gr-qc].

[317] Miguel C. Ferreira, Caio F. B. Macedo, and Vitor Cardoso. “Orbital fingerprints of ultralight scalar fields around black holes.” In: *Phys. Rev. D* 96.8 (2017), p. 083017. DOI: 10.1103/PhysRevD.96.083017. arXiv: 1710.00830 [gr-qc].

[318] Ryuichi Fujita and Vitor Cardoso. “Ultralight scalars and resonances in black-hole physics.” In: *Phys. Rev. D* 95.4 (2017), p. 044016. DOI: 10.1103/PhysRevD.95.044016. arXiv: 1612.00978 [gr-qc].

[319] Vitor Cardoso et al. “Parasitic black holes: The swallowing of a fuzzy dark matter soliton.” In: *Phys. Rev. D* 106.12 (2022), p. L121302. DOI: 10.1103/PhysRevD.106.L121302. arXiv: 2207.09469 [gr-qc].

[320] GRAVITY Collaboration. “Scalar field effects on the orbit of S2 star.” In: *MNRAS* 489.4 (2019), pp. 4606–4621. DOI: 10.1093/mnras/stz2300. arXiv: 1908.06681 [astro-ph.GA].

[321] Richard Brito, Vitor Cardoso, and Paolo Pani. “Black holes as particle detectors: evolution of superradiant instabilities.” In: *Class. Quant. Grav.* 32.13 (2015), p. 134001. DOI: 10.1088/0264-9381/32/13/134001. arXiv: 1411.0686 [gr-qc].

[322] Hideo Kodama and Hirotaka Yoshino. “Axiverse and Black Hole.” In: *Int. J. Mod. Phys. Conf. Ser.* 7 (2012). Ed. by Sean Hayward and Xin-Zhou Li, pp. 84–115. DOI: 10.1142/S2010194512004199. arXiv: 1108.1365 [hep-th].

[323] Vitor Cardoso et al. “Piercing of a boson star by a black hole.” In: *Phys. Rev. D* 106.4 (2022), p. 044030. DOI: 10.1103/PhysRevD.106.044030. arXiv: 2206.00021 [gr-qc].

[324] Paolo Pani et al. “Perturbations of slowly rotating black holes: massive vector fields in the Kerr metric.” In: *Phys. Rev. D* 86 (2012), p. 104017. DOI: 10.1103/PhysRevD.86.104017. arXiv: 1209.0773 [gr-qc].

[325] Richard Brito, Vitor Cardoso, and Paolo Pani. “Superradiance: New Frontiers in Black Hole Physics.” In: *Lect. Notes Phys.* 906 (2015), pp.1–237. DOI: 10.1007/978-3-319-19000-6. arXiv: 1501.06570 [gr-qc].

[326] Vitor Cardoso et al. “Constraining the mass of dark photons and axion-like particles through black-hole superradiance.” In: *JCAP* 03 (2018), p. 043. DOI: 10.1088/1475-7516/2018/03/043. arXiv: 1801.01420 [gr-qc].

[327] Solomon Endlich and Riccardo Penco. “A modern approach to superradiance.” In: *Journal of High Energy Physics* 2017.5, 52 (May 2017), p. 52. DOI: `10.1007/JHEP05(2017)052`. arXiv: `1609.06723 [hep-th]`.

[328] Masha Baryakhtar, Robert Lasenby, and Mae Teo. “Black Hole Superradiance Signatures of Ultralight Vectors.” In: *Phys. Rev. D* 96.3 (2017), p. 035019. DOI: `10.1103/PhysRevD.96.035019`. arXiv: `1704.05081 [hep-ph]`.

[329] Nuno M. Santos et al. “Black holes with synchronised Proca hair: linear clouds and fundamental non-linear solutions.” In: *JHEP* 07 (2020), p. 010. DOI: `10.1007/JHEP07(2020)010`. arXiv: `2004.09536 [gr-qc]`.

[330] Yifan Chen et al. “Photon Ring Astrometry for Superradiant Clouds.” In: *Phys. Rev. Lett.* 130.11 (2023), p. 111401. DOI: `10.1103/PhysRevLett.130.111401`. arXiv: `2211.03794 [gr-qc]`.

[331] Sergei Kopeikin, Michael Efroimsky, and George Kaplan. *Relativistic Celestial Mechanics of the Solar System*. Weinheim, Germany: Wiley-VCH, 2011. ISBN: 978-3-527-40856-6, 978-3-527-63456-9. DOI: `10.1002/9783527634569`.

[332] Coryn A. L. Bailer-Jones. *Practical Bayesian Inference: A Primer for Physical Scientists*. Cambridge University Press, 2017. DOI: `10.1017/9781108123891`.

[333] Carlos A. R. Herdeiro, Eugen Radu, and Nuno M. Santos. “A bound on energy extraction (and hairiness) from superradiance.” In: *Phys. Lett. B* 824 (2022), p. 136835. DOI: `10.1016/j.physletb.2021.136835`. arXiv: `2111.03667 [gr-qc]`.

[334] Eve C. Ostriker. “Dynamical Friction in a Gaseous Medium.” In: *The Astrophysical Journal* 513.1 (Mar. 1999), p. 252. DOI: `10.1086/306858`. URL: `https://dx.doi.org/10.1086/306858`.

[335] Dina Traykova et al. “Dynamical friction from scalar dark matter in the relativistic regime.” In: *Phys. Rev. D* 104.10 (2021), p. 103014. DOI: `10.1103/PhysRevD.104.103014`. arXiv: `2106.08280 [gr-qc]`.

[336] Rodrigo Vicente and Vitor Cardoso. “Dynamical friction of black holes in ultralight dark matter.” In: *Phys. Rev. D* 105.8 (2022), p. 083008. DOI: `10.1103/PhysRevD.105.083008`. arXiv: `2201.08854 [gr-qc]`.

[337] Caio F. B. Macedo et al. “Into the lair: gravitational-wave signatures of dark matter.” In: *Astrophys. J.* 774 (2013), p. 48. DOI: `10.1088/0004-637X/774/1/48`. arXiv: `1302.2646 [gr-qc]`.

[338] Hyosun Kim and Woong-Tae Kim. “Dynamical Friction of a Circular-Orbit Perturber in a Gaseous Medium.” In: *Astrophys. J.* 665 (2007), pp. 432–444. DOI: `10.1086/519302`. arXiv: `0705.0084 [astro-ph]`.

[339] S. Gillessen et al. “Detection of a drag force in G2’s orbit: Measuring the density of the accretion flow onto Sgr A* at 1000 Schwarzschild radii.” In: *arXiv e-prints*, arXiv:1812.01416 (Dec. 2018), arXiv:1812.01416. DOI: 10.48550/arXiv.1812.01416. arXiv: 1812.01416 [astro-ph.GA].

[340] A. Foschi et al. “Using the motion of S2 to constrain scalar clouds around Sgr A*.” In: *Mon. Not. Roy. Astron. Soc.* 524.1 (2023), pp. 1075–1086. DOI: 10.1093/mnras/stad1939. arXiv: 2306.17215 [astro-ph.GA].

[341] Jurgen Muller, James G. Williams, and Slava G. Turyshev. “Lunar laser ranging contributions to relativity and geodesy.” In: *Astrophys. Space Sci. Libr.* 349 (2008). Ed. by Hansjörg Dittus, Claus Lammerzahl, and Slava G. Turyshev, pp. 457–472. DOI: 10.1007/978-3-540-34377-6_21. arXiv: gr-qc/0509114.

[342] Alex S. Konopliv et al. “Mars high resolution gravity fields from MRO, Mars seasonal gravity, and other dynamical parameters.” In: 211.1 (Jan. 2011), pp. 401–428. DOI: 10.1016/j.icarus.2010.10.004.

[343] A. Hees et al. “Constraints on modified Newtonian dynamics theories from radio tracking data of the Cassini spacecraft.” In: *Phys. Rev. D* 89 (2014), p. 102002. DOI: 10.1103/PhysRevD.89.102002. arXiv: 1402.6950 [gr-qc].

[344] A. Eckart and R. Genzel. “Observations of stellar proper motions near the Galactic Centre.” In: *Nature* 383 (1996), pp. 415–417. DOI: 10.1038/383415a0.

[345] R. Schödel et al. “A star in a 15.2-year orbit around the supermassive black hole at the centre of the Milky Way.” In: 419.6908 (Oct. 2002), pp. 694–696. DOI: 10.1038/nature01121. arXiv: astro-ph/0210426 [astro-ph].

[346] S. Gillessen et al. “Monitoring Stellar Orbits Around the Massive Black Hole in the Galactic Center.” In: 692.2 (Feb. 2009), pp. 1075–1109. DOI: 10.1088/0004-637X/692/2/1075. arXiv: 0810.4674 [astro-ph].

[347] S. Gillessen et al. “The Orbit of the Star S2 Around SGR A* from Very Large Telescope and Keck Data.” In: 707.2 (Dec. 2009), pp. L114–L117. DOI: 10.1088/0004-637X/707/2/L114. arXiv: 0910.3069 [astro-ph.GA].

[348] Nadeen Sabha et al. “The S-Star Cluster at the Center of the Milky Way: On the nature of diffuse NIR emission in the inner tenth of a parsec.” In: *Astron. Astrophys.* 545 (2012), A70. DOI: 10.1051/0004-6361/201219203. arXiv: 1203.2625 [astro-ph.GA].

[349] Clare Burrage and Jeremy Sakstein. “Tests of Chameleon Gravity.” In: *Living Rev. Rel.* 21.1 (2018), p. 1. DOI: 10.1007/s41114-018-0011-x. arXiv: 1709.09071 [astro-ph.CO].

[350] Vincenzo Salzano et al. “Breaking the Vainshtein screening in clusters of galaxies.” In: *Phys. Rev. D* 95.4 (2017), p. 044038. DOI: `10.1103/PhysRevD.95.044038`. arXiv: `1701.03517 [astro-ph.CO]`.

[351] Jose Beltran Jimenez, Andre Luis Delvas Froes, and David F. Mota. “Screening Vector Field Modifications of General Relativity.” In: *Phys. Lett. B* 725 (2013), pp. 212–217. DOI: `10.1016/j.physletb.2013.07.032`. arXiv: `1212.1923 [astro-ph.CO]`.

[352] Manuel Gonzalez-Espinoza et al. “Screening fifth forces in scalar-vector-tensor theories.” In: (Dec. 2023). arXiv: `2312.05381 [gr-qc]`.

[353] D. Borka et al. “Constraining the range of Yukawa gravity interaction from S2 star orbits.” In: *JCAP* 11 (2013), p. 050. DOI: `10.1088/1475-7516/2013/11/050`. arXiv: `1311.1404 [astro-ph.GA]`.

[354] S. Capozziello et al. “Constraining Extended Gravity Models by S2 star orbits around the Galactic Centre.” In: *Phys. Rev. D* 90.4 (2014), p. 044052. DOI: `10.1103/PhysRevD.90.044052`. arXiv: `1408.1169 [astro-ph.GA]`.

[355] Alexander F. Zakharov et al. “Constraining the range of Yukawa gravity interaction from S2 star orbits II: Bounds on graviton mass.” In: *JCAP* 05 (2016), p. 045. DOI: `10.1088/1475-7516/2016/05/045`. arXiv: `1605.00913 [gr-qc]`.

[356] A. F. Zakharov et al. “Constraining the range of Yukawa gravity interaction from S2 star orbits III: improvement expectations for graviton mass bounds.” In: *JCAP* 04 (2018), p. 050. DOI: `10.1088/1475-7516/2018/04/050`. arXiv: `1801.04679 [gr-qc]`.

[357] Ivan de Martino, Riccardo della Monica, and Mariafelicia de Laurentis. “f(R) gravity after the detection of the orbital precession of the S2 star around the Galactic Center massive black hole.” In: *Phys. Rev. D* 104.10 (2021), p. L101502. DOI: `10.1103/PhysRevD.104.L101502`. arXiv: `2106.06821 [gr-qc]`.

[358] Anna D’Addio. “S-star dynamics through a Yukawa–like gravitational potential.” In: *Phys. Dark Univ.* 33 (2021), p. 100871. DOI: `10.1016/j.dark.2021.100871`.

[359] Predrag Jovanović et al. “Influence of bulk mass distribution on orbital precession of S2 star in Yukawa gravity.” In: *Eur. Phys. J. D* 75.5 (2021), p. 145. DOI: `10.1140/epjd/s10053-021-00154-z`. arXiv: `2105.03403 [astro-ph.GA]`.

[360] A. Hees et al. “Testing General Relativity with stellar orbits around the supermassive black hole in our Galactic Center.” In: *Phys. Rev. Lett.* 118.21 (2017), p. 211101. DOI: `10.1103/PhysRevLett.118.211101`. arXiv: `1705.07902 [astro-ph.GA]`.

[361] Matt Visser. "Mass for the graviton." In: *Gen. Rel. Grav.* 30 (1998), pp. 1717–1728. DOI: 10.1023/A:1026611026766. arXiv: gr-qc/9705051.

[362] Kurt Hinterbichler. "Theoretical Aspects of Massive Gravity." In: *Rev. Mod. Phys.* 84 (2012), pp. 671–710. DOI: 10.1103/RevModPhys.84.671. arXiv: 1105.3735 [hep-th].

[363] Itzhak Bars and Matt Visser. "Feeble intermediate-range forces from higher dimensions." In: *Phys. Rev. Lett.* 57 (1 1986), pp. 25–28. DOI: 10.1103/PhysRevLett.57.25. URL: https://link.aps.org/doi/10.1103/PhysRevLett.57.25.

[364] C. D. Hoyle et al. "Submillimeter tests of the gravitational inverse square law: a search for 'large' extra dimensions." In: *Phys. Rev. Lett.* 86 (2001), pp. 1418–1421. DOI: 10.1103/PhysRevLett.86.1418. arXiv: hep-ph/0011014.

[365] L. Perivolaropoulos. "PPN Parameter gamma and Solar System Constraints of Massive Brans-Dicke Theories." In: *Phys. Rev. D* 81 (2010), p. 047501. DOI: 10.1103/PhysRevD.81.047501. arXiv: 0911.3401 [gr-qc].

[366] Justin Alsing et al. "Gravitational radiation from compact binary systems in the massive Brans-Dicke theory of gravity." In: *Phys. Rev. D* 85 (2012), p. 064041. DOI: 10.1103/PhysRevD.85.064041. arXiv: 1112.4903 [gr-qc].

[367] Salvatore Capozziello et al. "Hybrid metric-Palatini gravity." In: *Universe* 1.2 (2015), pp. 199–238. DOI: 10.3390/universe1020199. arXiv: 1508.04641 [gr-qc].

[368] Joshua A. Frieman and Ben-Ami Gradwohl. "Dark matter and the equivalence principle." In: *Phys. Rev. Lett.* 67 (21 1991), pp. 2926–2929. DOI: 10.1103/PhysRevLett.67.2926. URL: https://link.aps.org/doi/10.1103/PhysRevLett.67.2926.

[369] Ben-Ami Gradwohl and Joshua A. Frieman. "Dark matter, long range forces, and large scale structure." In: *Astrophys. J.* 398 (1992), pp. 407–424. DOI: 10.1086/171865.

[370] Sean M. Carroll et al. "Dark-Matter-Induced Weak Equivalence Principle Violation." In: *Phys. Rev. Lett.* 103 (2009), p. 011301. DOI: 10.1103/PhysRevLett.103.011301. arXiv: 0807.4363 [hep-ph].

[371] E. G. Adelberger, Blayne R. Heckel, and A. E. Nelson. "Tests of the gravitational inverse square law." In: *Ann. Rev. Nucl. Part. Sci.* 53 (2003), pp. 77–121. DOI: 10.1146/annurev.nucl.53.041002.110503. arXiv: hep-ph/0307284.

[372] Clifford M. Will. "Solar system versus gravitational-wave bounds on the graviton mass." In: *Class. Quant. Grav.* 35.17 (2018), 17LT01. DOI: 10.1088/1361-6382/aad13c. arXiv: 1805.10523 [gr-qc].

[373] P. Jovanović et al. "Constraints on Yukawa gravity parameters from observations of bright stars." In: *JCAP* 03 (2023), p. 056. DOI: `10.1088/1475-7516/2023/03/056`. arXiv: `2211.12951 [astro-ph.GA]`.

[374] Gregory S. Adkins and Jordan McDonnell. "Orbital precession due to central-force perturbations." In: *Phys. Rev. D* 75 (2007), p. 082001. DOI: `10.1103/PhysRevD.75.082001`. arXiv: `gr-qc/0702015`.

[375] Benjamin P. Abbott et al. "GW170104: Observation of a 50-Solar-Mass Binary Black Hole Coalescence at Redshift 0.2." In: *Phys. Rev. Lett.* 118.22 (2017). [Erratum: Phys.Rev.Lett. 121, 129901 (2018)], p. 221101. DOI: `10.1103/PhysRevLett.118.221101`. arXiv: `1706.01812 [gr-qc]`.

[376] Zhaoyi Xu et al. "Black Hole Space-time In Dark Matter Halo." In: *JCAP* 09 (2018), p. 038. DOI: `10.1088/1475-7516/2018/09/038`. arXiv: `1803.00767 [gr-qc]`.

[377] Vitor Cardoso et al. "Black holes in galaxies: Environmental impact on gravitational-wave generation and propagation." In: *Phys. Rev. D* 105.6 (2022), p. L061501. DOI: `10.1103/PhysRevD.105.L061501`. arXiv: `2109.00005 [gr-qc]`.

[378] Sourabh Nampalliwar et al. "Modeling the Sgr A* Black Hole Immersed in a Dark Matter Spike." In: *Astrophys. J.* 916.2 (2021), p. 116. DOI: `10.3847/1538-4357/ac05cc`. arXiv: `2103.12439 [astro-ph.HE]`.

[379] C. T. Cunningham. "Optical appearance of distant objects to observers near and inside a Schwarzschild black hole." In: *Physical Review D* 12.2 (July 1975), pp. 323–328. DOI: `10.1103/PhysRevD.12.323`.

[380] A. Siwek et al. "Perceiving light rays above and below the horizon of a black hole in Schwarzschild spacetime." In: *J. Phys. Conf. Ser.* 574.1 (2015). Ed. by Elias C. Vagenas and Dimitros S. Vlachos, p. 012060. DOI: `10.1088/1742-6596/574/1/012060`.

DECLARATION

I declare that this document is an original work of my own and that it fulfills all the requirements of the Code of Conduct and Good Practices of the Universidade de Lisboa.

Name: Arianna Foschi
Student number: 428707

Lisbon, 2024

Arianna Foschi

COLOPHON

This document was typeset using the typographical look-and-feel `classicthesis` developed by André Miede and Ivo Pletikosić. The style was inspired by Robert Bringhurst's seminal book on typography *"The Elements of Typographic Style"*.

Final Version as of May 3, 2024 (draft v1).